Modified Direct Torque Control Topologies in Five-Phase Induction Motor for Reduction of Torque Ripple, Flux Ripple, and Current Harmonic Distortion

Submitted in partial fulfillment of the requirements

for the award of the degree of

DOCTOR OF PHILOSOPHY

in

Electrical Engineering

By

Chagam Reddy Venkata Subba Reddy

Roll No: 718118

Supervisor:

Dr. Swati Devabhaktuni

Assistant Professor

Department of Electrical Engineering

NATIONAL INSTITUTE OF TECHNOLOGY WARANGAL

HANUMAKONDA-506004, TELANGANA STATE, INDIA

December - 2023

Approval

This Thesis work entitled **"Modified Direct Torque Control Topologies in Five-Phase Induction Motor for Reduction of Torque Ripple, Flux Ripple, and Current Harmonic Distortion"** by **Chagam Reddy Venkata Subba Reddy**, bearing **Roll No: 718118**, is approved for the degreeof **Doctor of Philosophy** in **Electrical Engineering** from **National Institute of Technology, Warangal**.

Examiners

_____

_____

_____

Supervisor

_____

Dr. Swati Devabhaktuni

Assistant Professor

Department of Electrical Engineering

NIT Warangal

Chairman

_____

Dr. Vishwanathan N

Professor

Department of Electrical Engineering

NIT Warangal

Date: _____

Place: NIT Warangal

DEPARTMENT OF ELECTRICAL ENGINEERING

NATIONAL INSTITUTE OF TECHNOLOGY WARANGAL

HANUMAKONDA-506 004, TELANGANA, INDIA

CERTIFICATE

This is to certify that the thesis entitled **"Modified Direct Torque Control Topologies in Five-Phase Induction Motor for Reduction of Torque Ripple, Flux Ripple, and Current Harmonic Distortion"** which is being submitted by **Chagam Reddy Venkata Subba Reddy**, bearing **Roll No.718118**, is a bonafide work submitted to **National Institute of Technology, Warangal** in partial fulfillment of the requirements for the award of the degree of **Doctor of Philosophy** in **Department of Electrical Engineering**. To the best of my knowledge, the work incorporated in this thesis has not been submitted elsewhere for the award of any degree.

Dr. Swati Devabhaktuni

(Supervisor)

Assistant Professor
Department of Electrical Engineering

NIT Warangal

Date:

Place: NIT Warangal

DECLARATION

This is to certify that the work presented in the thesis entitled **"Modified Direct Torque Control Topologies in Five-Phase Induction Motor for Reduction of Torque Ripple, Flux Ripple, and Current Harmonic Distortion"** is a bonafide work done by me under the supervision of **Dr. Swati Devabhaktuni,** Department of Electrical Engineering, National Institute of Technology,Warangal, India and is not submitted elsewhere for the award of any degree.

I declare that this written submission represents my ideas in my own words and where others' ideas or words have been included, I have adequately cited and referenced the original sources. I also declare that I have adhered to all principles of academic honesty and integrity and have not misrepresented or fabricated or falsified any idea/data/fact/source in my submission. I understand that any violation of the above will be cause for disciplinary action by the Institute and can also evoke penal action from the sources which have thus not been properly cited or from whom proper permission has not been taken when needed.

Chagam Reddy Venkata Subba Reddy
(Roll No.718118)

Date:_____

NIT Warangal

ACKNOWLEDGMENTS

I would like to express my gratitude to my supervisor, **Dr. Swati Devabhaktuni**, for providing enough freedom and generating a homely feeling throughout the journey, for his patience and valuable suggestions. It is impossible to accomplish this dissertation work without his support, and encouragement. Many thanks for his support and encouragement to achieve all my personal life ambitions too. Apart from all these, it's an honor for me to associate with a good human being like him.

I would like to thank **Prof. B. L. Narasimharaju**, Head of the Electrical Engineering Department for providing all the required facilities and support.

I wish to express my sincere thanks to **Prof. Bidyadhar Subudhi**, Director, NIT Warangal for his official support and encouragement.

I take the privilege to thank all my Doctoral Scrutiny Committee members, **Prof. Vishwanathan N**, Department of Electrical Engineering, **Dr. PorpandiSelvi S**, Associate Professor, Department of Electrical Engineering, **Dr. Ch. Ramulu**, Assistant Professor, Department of Electrical Engineering and **Dr. K. Naga Srinivasarao Batta**, Assistant Professor, Department of Electronics and Communication Engineering for their detailed review, constructive suggestions and excellent advice during the progress of this research work.

I also express my sincere thanks to **Prof. M. Sailaja Kumari** and **Prof. S. Srinivasa Rao**, former heads of the Electrical Engineering Department for their valuable suggestions, support, and cooperation.

I also appreciate the encouragement from teaching, and non-teaching members and fraternities of the Electrical Engineering Department, NIT Warangal. They have always been motivating and supportive.

I express my deep sense of gratitude and reverence to my beloved father **Sri. C Chinna Bali Reddy**, mother **Smt. C Siddamma**, wife **Smt. Rama Devi**, brother-in-law **Mr. G Yogi,** Sister **Smt. Venkata Sudha** for their sincere prayers, blessings, constant encouragement, shouldering the responsibilities and moral support rendered to me throughout my life, without which my research work would not have been possible. It is a great pleasure for me to acknowledge and express my appreciation to all my well-wishers for their understanding, relentless support, and encouragement during my research work

I am thankful to my co-scholars and friends for their support throughout my research period.

Finally, I would like to express my gratitude to the National Institute of Technology Warangal for providing me with the opportunity to carry out research and I am indebted to the people of the country for indirectly supporting my work.

Chagam Reddy Venkata Subba Reddy

ABSTRACT

Induction motors have become the workhorses of modern process industries, employing advanced vector control strategies like FOC, PTC, and DTC methods. In those, 5-phase induction motors offer several advantages over conventional 3-phase machines, including increased fault-tolerant capability, reduced per-phase power, improved efficiency, high torque density, lightweight construction, smooth operation, and the needs a simple 2-level 5-leg inverter for control. The Direct Torque Control (DTC) scheme is a widely used control technique due to its simplicity, less parameter sensitivity, and quicker dynamics although it suffers from higher torque ripple, flux ripple, and variable switching frequency. In DTC, the electromagnetic torque and stator flux of the induction motor are controlled by selecting a suitable voltage vector from a predefined switching vector table. Existing DTC techniques for 5-phase induction motors strictly adhere to conventional DTC logic, focusing only on altering the switching table to improve the steady-state performance of the drive, still, these schemes suffer with higher torque and flux ripple and variable switching frequencies. The solution involves combining a dual inverter configuration with a 5-phase open-end winding induction motor to amalgamate features such as a simple structure, an increased number of voltage levels, enhanced fault-tolerance, reduced voltage stress across switches, more switching redundancies, and zero common-mode voltage. This thesis aims to modify DTC control techniques to reduce torque ripple and flux ripple, along with minimizing current harmonic distortion without significantly affecting the dynamic performance of the drive.

The proposed Direct Torque Control (DTC) employs a constant switching torque controller, replacing the hysteresis torque controller on a 2-level inverter-controlled 5-phase induction motor drive without modifying the lookup table. The constant switching controller is implemented with a PI controller and triangular wave, comparator; and this torque controller regulates the duty cycle of selected active vectors over a sample time during variable-speed operations. The duty cycle of active voltage vectors is controlled based on speed and load conditions, leading to reduced torque ripple at low speeds. The constant switching torque (CST) controller ensures a nearly constant switching frequency by prompting the torque controller to change its status at regular intervals. However, the proposed CST-DTC exhibits slower torque and speed dynamics compared to Conventional DTC (C-DTC) due to the frequent occurrence of zero vectors. These slower dynamics are improved with the

help of the proposed Fractional Order PI (FOPI) controller-based CST-DTC (FOPI-CST-DTC) method without affecting the steady-state performance as that of PI controller-based CST-DTC. The proposed FOPI-CST-DTC control scheme shows, the reduction in torque ripple and current harmonic distortion by nearly maintaining the constant switching frequency with improved dynamic performance.

In previous work, the use of a hysteresis flux controller resulted in higher flux ripple and the harmonic plane components not eliminated. Constant Switching Flux (CSF) controller along with the Constant Switching Torque (CST) controller-based Direct Torque Control (DTC) scheme is proposed to enhance both the flux and torque profiles, as well as the current profile, without disrupting the dynamic performance of the 5-phase induction motor. This approach utilizes 10 virtual voltage vectors distributed across 10 sectors. The reduction of torque ripple and stator flux ripple is achieved by regulating the duration of voltage vectors through the Constant Switching Torque and Flux controllers. To eliminate harmonic plane components, the proposed scheme employs virtual voltage vectors generated from large and medium vectors along the same axis.

The slip speed/slip angle control based direct flux control method of a 5-phase induction motor with a simple sample-based reference voltage controller with a simplified lookup table has been introduced to improve the steady-state performance of the drive with reduced complexity. The proposed control scheme uses 20 virtual voltage vectors with simplified 2-lookup tables under high-speed and low speeds. The main objective of the proposed control scheme is to maintain constant switching frequency for different speeds under various loading conditions along with torque ripple and flux ripple reduction w.r.t exiting DTC schemes. The proposed controller changes its state for every sample period and hence change of active vector for every sample time causes constant switching frequency throughout the drive operation. The proposed control scheme also uses the virtual voltage vectors to eliminate the harmonic plane components. Since the proposed control scheme is based on direct flux control, precise control of stator flux is possible and hence the average flux ripple and current %THD show great reduction when compared with torque ripple content.

The steady-state torque ripple and stator flux ripple further can be reduced by employing an open-end winding configuration with dual 5-leg inverter feeding. The proposed 7-level torque controller under high speeds and 3-level torque controller under low speeds along with a 2-level flux controller with a modified lookup table reduces the flux ripple, torque ripple, and harmonic current distortion. The proposed method generates 30 Virtual Voltage vectors (VVV) in dual inverter

configuration from adjacent and nonadjacent VVVs of individual inverters by maintaining 72^0 and 144^0 phase displacement such that the resultant common mode voltage for dual inverter configuration will become zero. The zero common mode voltage allows the use of a single DC source for two inverters and eliminates bulky isolation transformers.

The Proposed DTC control schemes are built with MATLAB/Simulink software and interfaced with the dSPACE-1202 real-time controller. The experimental work has been conducted to test the effectiveness of the proposed schemes on a 5-phase induction motor drive setup. In this thesis, the obtained experimental results of proposed DTC control schemes are compared with the experimental results of existing DTC schemes to know the effectiveness of the proposed methods.

Contents

List of Figures

List of Tables

List of Abbreviations

AC	Alternating current
ADC	Analog to digital converter
ASD	Adjustable speed drives
BW	Bandwidth
CMV	**C**ommon mode current
CMC	Common mode voltage
CSF	Constant switching flux controller
CST	Constant switching torque controller
DAC	Digital to analog converter
DC	Direct current
DFC	Direct flux control
DI	Dual inverter
DIFPOEWIM	Dual inverter fed five-phase open-end winding induction motor
DSO	Digital storage oscilloscope
DSP	Digital signal processor
DTC	Direct torque control
FOC	Field oriented control
FOPI	Fractional order proportional integral controller
FOPID	Fractional order proportional integral derivative controller
FPIM	Five-phase induction motor
FPOEWIM	Five-phase open-end winding induction motor
HB	Hysteresis band
HP	Horsepower
IGBT	Insulated gate bipolar transistor
MLI	Multi-level inverters
NPC	Neutral point converter
OEW	Open-end winding
PI	Proportional integral controller

PMSM	Permanent magnet synchronous motor
PPR	Pulses per rotation
PTC	Predictive torque control
rpm	Rotations per minute
SSC	Slip speed control
SVPWM	Space vector pulse width modulation
SVM	Space vector modulation
SVM-DTC	Space vector modulation-based direct torque control
VSI	Voltage source inverter
THD	Total harmonic distortion
VVV	Virtual voltage vectors

List of symbols

T	Electromagnetic torque
T_l	Load torque
p	Number of poles
J	Moment of inertia
R_s	Stator resistance
R_r	Rotor resistance
L_s	Stator inductance
L_r	Rotor inductance
L_m	Magnetizing inductance
Ψ_s	Stator flux linkages
Ψ_r	Rotor flux linkages
T_s	Sampling period/control period
V_s	Stator voltage
I_s	Stator current
V_{sref}	Reference stator voltage vector
Ψ_{sref}	Reference stator flux linkages
V_{dc}	Inverter DC link voltage
V_α	α-axis stator voltage
V_β	β-axis stator voltage
$\alpha\beta$	Fundamental plane
xy	Harmonic plane
ω_e	Synchronous frequency
ω_s	Stator flux frequency
Θ,δ	Space angle
$\Delta\theta$	Change in space angle
d	Duty cycle

CHAPTER 1

Introduction & Literature Survey

Chapter 1

Introduction

1.1 Background

The electric motors convert electrical energy to mechanical work. There has been a nonstop development in the field of electric motors and electric drives since the beginning of the first principle of the electric motor by Michael Faraday in 1821. Later in 1888, Nikola Tesla brought a major dramatic change throughout the world after he invented the induction motor [1]. Electric motors are becoming at the forefront of modern industrial advancements and reshaping industries, consuming 70% of world electricity power consumption [2]. Electric motors find huge applications in daily life applications like elevators, disc drives, compressors, draught fans, and agriculture tools, text tiles, machine tools, robotics, aerospace, electric mobility. The variable-speed electric drive avoids the use of mechanical gears and saves energy loss. In the initial days, the researchers were focused on the reduction of weight/power and improvement of the motor efficiency. Today, modern motors have achieved efficiencies up to 95-96% with no further improvement expectations from the consumers [1]. An electric motor with speed control techniques is known as an adjustable speed drive (ASD) which helps in accurate position control and effective energy utilization with the application of power electronics switches-based power modulators [3]. The power electronic converters modulate the power in terms of voltage magnitude or frequency or both magnitude and frequency [3]. Many modern advanced works are in progress to improve the accurate position/speed control, energy utilization, sustainability, and reliability of modern adjustable-speed electric drives.

In the early days, DC motor drives were used in variable speed applications owing to their decoupled nature and simple and easy control even though it has complex construction and timely maintenance requirements with commutator and brushes [4]. The constructional and maintenance drawbacks associated with DC motors can be overcome by replacing AC motors in variable-speed applications [4]. The control of AC motors became flexible with advancements in power electronic switches and fast controllers. Among various types of AC motors, induction motors have become workhorses of modern industries due to their rugged and simple structure and easy control. Many research advancements are in progress to improve the performance of AC induction motor drives with modified advanced vector control schemes such as FOC, DTC, and PTC techniques [5-6]. Recently, many researchers have started to work

on multi-phase induction motors (more than 3 phases) due to their inherent features compared to three-phase motors counterparts. Some of the advantages of multi-phase induction motors are listed below [7-12].

- Greater fault-tolerance
- compact size
- high power/torque density
- increased efficiency
- fault-tolerant capacity
- Reduced per-phase current without increasing per-phase voltage i.e., reduced per-phase power without changing the total power rating
- Reduction of torque pulse magnitude and increase in torque pulse frequency cause smooth operation of the drive

The 5-phase induction motor has 5 stator windings with 72^0 phase displacement in a distributed or concentrated manner with a squirrel cage rotor which needs a 5-phase power supply. 5-phase induction motor suffers from the lack of readily available 5-phase power supply in utility centers and hence these are not suitable for general-purpose applications. With the advanced power semiconductor switches and fast DSP controllers, researchers and industry experts are focused use of five-phase induction motors in emerging fields like battery-powered electric transportation, and aircraft and ship propulsion where size, power density, and fault-tolerance are main constraints [13-15]. The working principle of a 5-phase induction motor is similar conventional 3-phase induction motor and will work on the Faraday law of electromagnetic induction.

1.2 Concept of 5-phase induction motor

1.2.1 Working principle

The 5-phase induction motor is a type of multi-phase induction motor family and contains 5 stator winding with 72^0 spatial displacement and excited with 5-phase supply with 72^0 phase displacement to produce a stator rotating magnetic field. The 5-phase induction motor stator windings are arranged in a distributed or concentrated manner with a squirrel cage rotor. The concentrated winding-based 5-phase induction motor carries concentrated winding and develops quasi-square wave flux distribution. The distributed winding-based 5-phase induction motor carries uniformly distributed windings and develops sinusoidal flux distribution [16]. In this thesis, the author considers the distributed stator winding-based 5-phase induction motor for subsequent experimental works. The working principle of a 5-phase induction motor with

distributed winding is similar to a conventional 3-phase induction motor and will work on the Faraday law of electromagnetic induction. Whenever the balanced 5-phase supply with 72^0 phase displacement is given to 72^0 spatially distributed stator windings of the 5-phase induction motor, it produces the rotating magnetic field with synchronous speed. The rotating magnetic field cuts the short-circuited rotor bars and causes the induced emf. The induced emf in short-circuited rotor bars drives the rotor currents which set the rotor magnetic field. The interaction between the stator and rotor magnetic field initiates the torque production.

1.2.2 Modelling of 5-phase induction motor

White and Woodson (1959) introduced the modeling of the universal n-phase machine in the first half of the 20th century[17]. A general n-phase decoupling transformation matrix is presented which applies to any odd or even phase number machines. With standard assumptions for a sinusoidal field distribution machine, a set of n equations is produced by applying a decoupling (Clarke's) transformation matrix. The first αβ pair is identical to the corresponding pair of equations for a three-phase machine and is responsible for useful torque production. The last equation (odd phase number) and the last two equations (even phase number) represent zero sequence components, the same as a three-phase machine. The remaining (n-3) sets (odd phase number) and (n-4) sets (even phase number) are extra components that are termed as x-y or non-torque-producing components. These components are limited by leakage impedance only similar to the zero sequence components, and thus will generate significant current distortion unless restricted by a proper control scheme. The stator αβ component only interacts with the rotor component to produce the working torque. The stator and rotor x-y components are isolated and they do not interact with each other or with the stator to rotor or rotor to the stator.

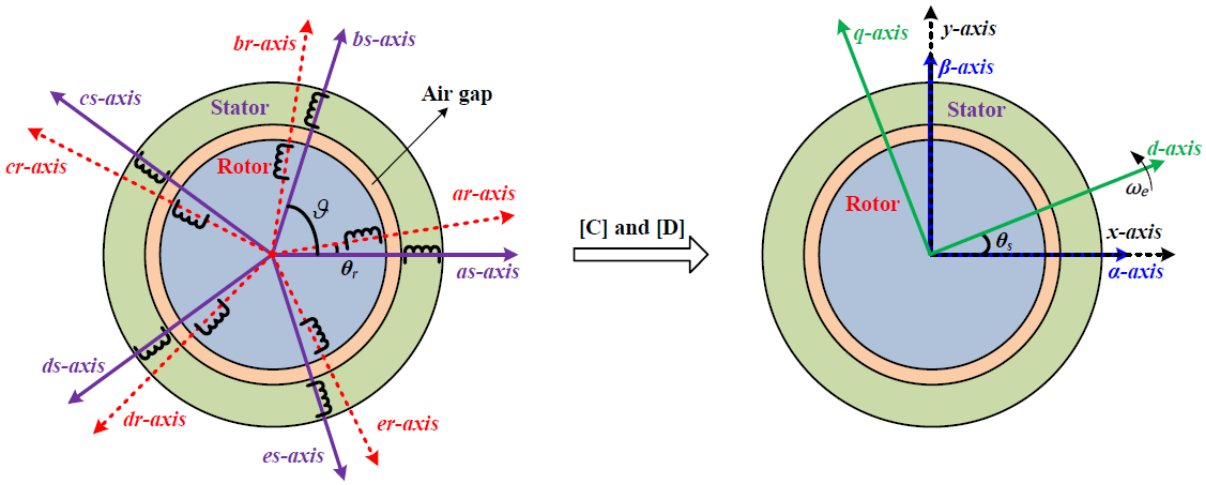

Figure 1.1 Modelling of Five-phase induction motor

Since the coupling between stator and rotor appears after decoupling transformation only in αβ equations of the multi-phase machine, it is only this set of equations that have to be transformed further, using rotational transformation. The form of this transformation is the same as for the corresponding three-phase machine. The resulting final d-q model in the common reference frame contains d-q and torque equations identical to that of a three-phase machine.

The 5-phase distributed winding induction motor is excited with a 5-phase supply voltage of 72^0 phase displacement as written below

$$V_{as} = V_m \sin(2\pi f t)$$
$$V_{bs} = V_m \sin\left(2\pi f t - {}^{2\pi}/_{5}\right)$$
$$V_{cs} = V_m \sin\left(2\pi f t - {}^{4\pi}/_{5}\right)$$
$$V_{ds} = V_m \sin\left(2\pi f t - {}^{6\pi}/_{5}\right)$$
$$V_{es} = V_m \sin\left(2\pi f t - {}^{8\pi}/_{5}\right) \quad (1.1)$$

The modeling of a 5-phase induction motor in 5-phase variable form makes a complex system design as it contains multiple time-varying inductance variables [18]. The time-varying inductance terms can be made constant by modeling the 5-phase induction motor in a 2-axis model in a synchronous rotating reference frame with the help of generalized n-phase machine modeling by White and Woodson (1959) as shown in Figure 1.1 [16].

$$\begin{bmatrix} V_{\alpha s} \\ V_{\beta s} \\ V_{xs} \\ V_{ys} \\ V_{os} \end{bmatrix} = \frac{2}{5} \begin{bmatrix} \cos(\theta_s) & \cos(\theta_s - 2\alpha) & \cos(\theta_s - 3\alpha) & \cos(\theta_s - 4\alpha) & \cos(\theta_s - 5\alpha) \\ \sin(\theta_s) & \sin(\theta_s - 2\alpha) & \sin(\theta_s - 3\alpha) & \sin(\theta_s - 4\alpha) & \sin(\theta_s - 5\alpha) \\ \cos(3\theta_s) & \cos 3(\theta_s - \alpha) & \cos(\theta_s - \alpha) & \cos(\theta_s - \alpha) & \cos(\theta_s - \alpha) \\ \sin(3\theta_s) & \sin 3(\theta_s - \alpha) & \sin(\theta_s - \alpha) & \sin(\theta_s - \alpha) & \sin(\theta_s - \alpha) \\ {}^1/_2 & {}^1/_2 & {}^1/_2 & {}^1/_2 & {}^1/_2 \end{bmatrix} \begin{bmatrix} V_a \\ V_b \\ V_c \\ V_d \\ V_e \end{bmatrix} \quad (1.2)$$

It is difficult to model a 5-phase induction motor 5-phase variable from induction motor voltage and torque equations containing mutual inductances which are time-varying. Analysis of dynamic behavior with time-varying parameters is too complex. To avoid this dynamic model of an induction motor is developed where 5-phase quantities are transformed into 2-phase dynamic quantities for control purposes. The stator voltage balancing equation in a phased manner is written as [18]

The stator voltage balancing equations 5-phase induction motor in a stationary reference frame can be written as follows.

$$V_{\alpha s} = I_{\alpha s}R_s + \frac{d\Psi_{\alpha s}}{dt}$$
$$V_{\beta s} = I_{\beta s}R_s + \frac{d\Psi_{\beta s}}{dt} \quad (1.3)$$

Where $V_{\alpha s,}V_{\beta s}$ = stator phase voltage in volts

I_s= stator phase current in amperes

R_s=stator resistance in ohms

$\Psi_{\alpha s}$, $\Psi_{\beta s}$= stator flux linkages in a stationary frame

The rotor voltage balancing equations in stationary reference frame can be written below

$$V_{\alpha r} = I_{\alpha r}R_s + \frac{d\Psi_{\alpha r}}{dt} - \omega_r\Psi_{\beta r}$$
$$V_{\beta r} = I_{\beta r}R_s + \frac{d\Psi_{\beta r}}{dt} + \omega_r\Psi_{\alpha r} \quad (1.4)$$

Where $V_{\alpha r,}V_{\beta r}$ = rotor phase voltage in volts

I_r= rotor phase current in amperes

R_r=rotor resistance in ohms

$\Psi_{\alpha r}$, $\Psi_{\beta r}$= Rotor flux linkages in a stationary frame

ω_r=Rotor speed in electrical rad/sec

The electromagnetic torque (T_e) produced in a 5-phase induction motor is expressed as (1.5)

$$T_e = \frac{5}{2}\frac{P}{2}\left(\Psi_{\alpha s}i_{\beta s} - \Psi_{\beta s}i_{\alpha s}\right) \quad (1.5)$$

The mechanical torque balancing equation can be written as (1.6)

$$\frac{J}{P/2}\frac{d\omega_r}{dt} = T_e - T_l \quad (1.6)$$

Where P = Induction motor stator poles

T_l = Load torque in Nm

1.3 Concept of 2-level 5-leg Inverter

The 2-level 5-leg inverter is the basic power circuit to drive the five-phase induction motor as shown in Figure 1.2. The 5-leg voltage source inverter (VSI) is fed with constant DC voltage. The squirrel cage 5-phase induction motor with star-connected is connected as shown in Figure 1.2 and the inverter output phase voltages are denoted with lowercase symbols (a, b, c, d, e), while the leg voltages have symbols in capital letters (A, B, C, D, E). The model of five-phase VSI is developed in space vector form by Duran et. al (2008).

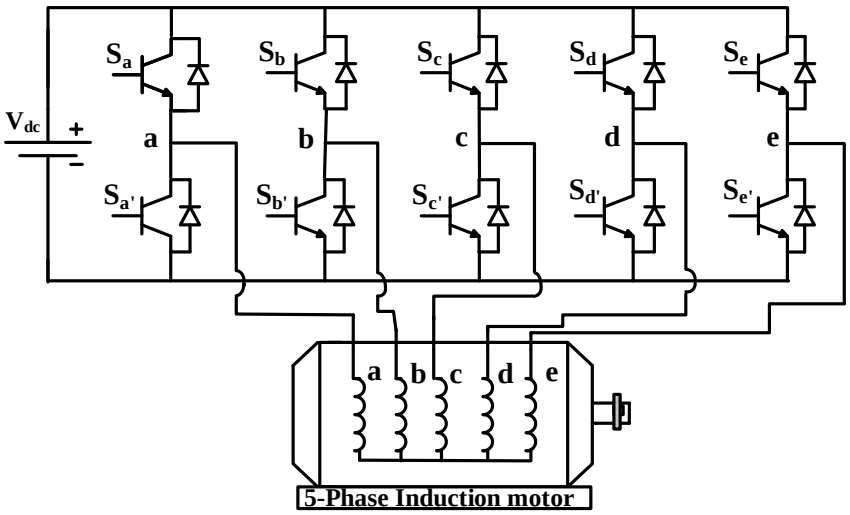

Figure 1.2 2-level 5-leg inverter with FPIM

At any instant, the 5 switches will be operated among 10 available switches as the two power switches of the same leg should be complimentary to avoid a short circuit of DC link voltage. The combination of these five switching states gives out thirty-two space voltage vectors. Out of thirty-two space vectors thirty are active vectors and two zero vectors. At any instant in time, the inverter can produce only one space vector. The space voltage vector location and magnitude of 2-level 5-leg VSI will be attained with the help of (1.1) and (1.2) in the fundamental ($\alpha\beta$) plane, and harmonic (xy) plane respectively as shown in Figure 1.3.

$$V_{s(\alpha\beta)} = \frac{2}{5}V_{dc}\left(S_a + S_b e^{j\frac{2\pi}{5}} + S_c e^{j\frac{4\pi}{5}} + S_d e^{j\frac{-4\pi}{5}} + S_e e^{j\frac{-2\pi}{5}}\right) \quad (1.1)$$

$$V_{s(xy)} = \frac{2}{5}V_{dc}\left(S_a + S_b e^{j\frac{-4\pi}{5}} + S_c e^{j\frac{2\pi}{5}} + S_d e^{j\frac{-2\pi}{5}} + S_e e^{j\frac{4\pi}{5}}\right) \quad (1.2)$$

Where $V_{s(\alpha\beta)}$=fundamental plane voltage space vector

$V_{s(xy)}$=harmonic plane voltage space vector

S_a, S_b, S_c, S_d, S_e=Each leg upper switch statuses (S_x= 0 or 1)

V_{dc}=Inverter DC link voltage

Based on space voltage vector magnitude, the 32 voltage vectors are classified as large, small, medium, and zero voltage vectors with the magnitudes of 0.6472Vdc, 0.2472Vdc, 0.4Vdc, and 0Vdc respectively in both fundamental and harmonic planes. The large voltage vectors in the fundamental plane appear as small voltage vectors and vice versa with opposite direction in the harmonic plane as shown in Figure 1.3. The medium voltage vector in the fundamental plane appears as medium voltage vectors in the harmonic plane in the same direction as in Figure 1.3.

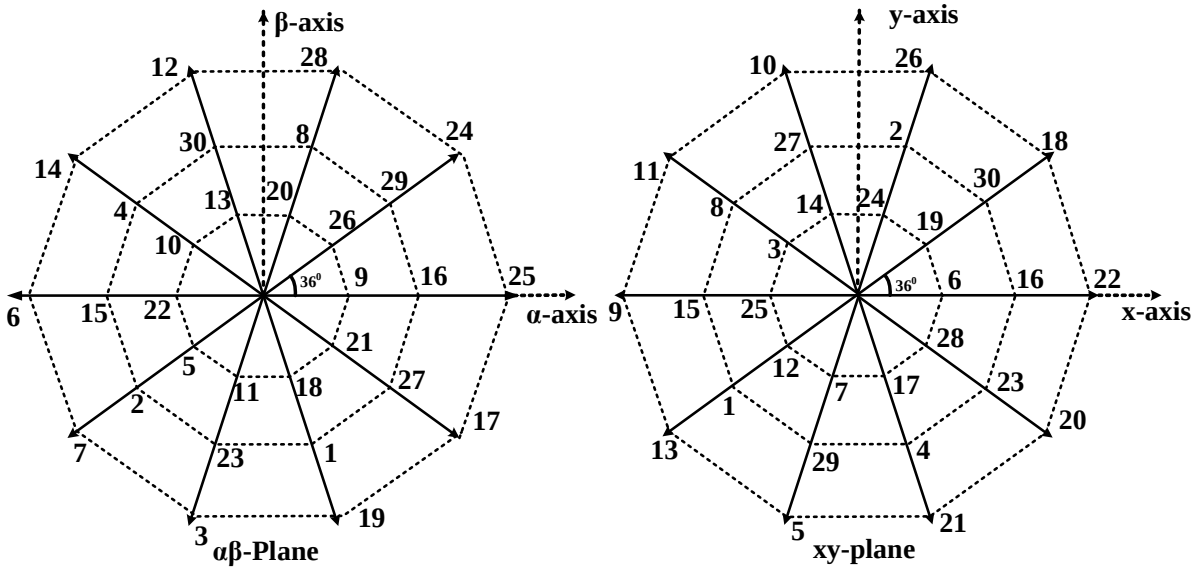

Figure 1.3 Space voltage vector location diagram in the both fundamental (αβ)-plane and harmonic (xy)-plane

The fundamental-plane voltage vectors are useful for the production of torque whereas the harmonic-plane voltage vectors produce only ohmic losses for the 5-phase distributed winding induction motor. Also, the xy plane components distort the phase current as these are dominant with the 3rd harmonic. It necessitates the elimination of xy plane components while implementing any control scheme for a 2-level VSI-fed 5-phase induction motor. Several control schemes were developed in the literature to remove xy plane harmonics.

1.4 Literature survey

The speed control of a 5-phase induction motor is necessary to use the drive in industrial and process applications. The basic and advanced control schemes that are available for conventional 3-phase machines can be applied to 5-phase induction motors with certain constraints. The widely used speed control schemes in industrial drives are broadly listed as: i) voltage/frequency control method ii) Field oriented control method iii) Model predictive control methods iv) Direct torque control method.

Voltage/frequency (v/f) control is a scalar control method that adjusts the magnitude of the stator voltage and frequency to keep the stator flux constant. While the reference voltage vector in v/f control can be implemented using carrier-based PWM or space vector PWM (SVPWM) techniques, scalar control methods are known for their limitations, including poor dynamics and unstable operation [19]. Consequently, they are not well-suited for high-performance drives. To address these limitations, Field-Oriented Control (FOC) comes into the

picture. FOC is a linear control strategy that uses linear controllers and PWM to generate applied voltage vectors to the motor control. FOC offers improved current profiles, stator flux control, and smooth torque patterns. However, it requires additional components like PWM modulator blocks and coordination transformation blocks, and it requires tuning of many parameters for PI controllers, leading to relatively slower dynamics and higher switching losses [6]. The model predictive control is a powerful non-linear control method and it selects the optimum voltage vectors based on previous historic conditions and optimization of cost function over the prediction zone [6]. The model predictive control technique maintains a good torque profile and current profile with faster dynamics. However, it suffers parameter sensitivity and high computation burden and needs fast-speed processors. The Direct Torque Control (DTC) is another powerful tool for high-performance drive applications which will operate on a predefined vector selection table based on predefined torque and flux error bands. The DTC method is simple to control, less sensitive to parameter variations, fast dynamics, and no need for coordination transformation block and inner current control loops [6].

Over the past two decades, numerous researchers have dedicated their efforts to developing speed control schemes for 5-phase induction motors, due to the evolution of advanced DSP controllers and rapid-acting power electronic switches [20]. Recent advancement in the realm of multi-phase machines, focusing on design perspectives and modelling, is elaborated in [21]-[22]. The performance analysis of both 5-phase and 3-phase inverters is detailed in [23] scalar control method. A fundamental space vector pulse width modulation (SVPWM) is applied to a 5-leg voltage source inverter (VSI) fed five-phase induction motor (FPIM) in [24] and [25], ensuring that the resulting xy plane components are reduced to zero. Furthermore, advanced vector control schemes such as field-oriented control, predictive torque control, and direct torque control have been implemented in the literature for 5-phase induction motors, demonstrating their effectiveness in enhancing motor performance. A simulation-based comparative analysis has been done for FOC and DTC in a 5-phase induction motor [26] and concluded that the FOC method exhibits better steady-state torque and flux profiles, however, it suffers from complexity as stated earlier. In [27], the FOC control scheme implemented on matrix converter fed FPIM which further increases the complexity of the system. In recent days predictive control technique popular and become a substitution for direct torque control to improve steady-state performance. In [28]-[30], PTC methods are implemented on a 5-phase induction motor, where suitable voltage vectors are selected based on the cost function. However, the PTC methods face limitations such as fine-tuning of

weighting factors in the cost function, more sensitivity to machine parameters, need of a fast DSP controller due to computational complexity.

The DTC scheme is another powerful method used for 5-phase induction motors due to its simple structure, less parameter sensitivity, and faster dynamics [31]-[32]. The DTC schemes available for conventional 3-phase machines cannot be applied directly to 5-phase machine as it contains fundamental plane and harmonic plane components. It is important to eliminate the harmonic plane components while implementing the DTC control scheme to avoid unnecessary power losses and current harmonic distortion. Several DTC schemes are implemented on a 5-phase induction motor to improve the steady-state profile. In [33], a classical DTC was implemented for a 5-phase induction motor with only large voltage vectors and it suffers from drawbacks associated with classical DTC of 3-phase machines and also not concentrated on harmonic plane components. The classical hysteresis-based DTC [34] is implemented on a 2-level VSI-controlled 5-phase interior permanent magnet synchronous motor (IPSM) by using a medium voltage vector and large voltage vector which suffer from shortcomings of classical DTC and harmonic plane components. Then the [35], discusses the 3-level hysteresis-based DTC of the FPIM and the harmonic plane components eliminated with the generation of virtual voltage vector from large and medium vectors on the same axis by volt-sec balance method and it suffers from high torque ripple and flux ripple. In [36], the same author implemented a 5-level DTC to enhance the low-speed characteristics of the FPIM with the help of a separate look-up table and selection of nearer vectors. This paper [36] uses fundamental and harmonic flux sector information to eliminate harmonic plane components and it won't make a complete zero of harmonic components, it needs two-stage vector selections to find a suitable vector. A 3-level DTC is implemented in [37] and uses two adjacent large vectors to make virtual voltage vectors such that the harmonic plane components zero with the volt-sec balance technique. The author in [37], reduces the common mode voltage to the lowest values by avoiding zero vectors and medium vectors. A three-level DTC is implemented with 20 virtual voltage vectors from large medium and medium-small vectors on the same axis in [38] with separate lookup tables to enhance the low-speed profile and it suffers from high torque ripple under low speeds due to active vector selection under torque error zero case. The author Tatte. Y, et al. implemented a modified 5-level torque controller to control the 5-phase induction motor with 20 virtual voltage vectors [39]. However, this method [39] uses two-stage vector selections to eliminate harmonic plane components which make complex control and this method still produces the little harmonic component. The DTC control schemes presented in [33]-[39] are hysteresis control-based DTC schemes that commonly suffer from

variable switching frequency. in [40]-[43], space vector modulation-based DTC (SVM-DTC) is implemented on a 5-phase induction motor and majorly focused on elimination of xy plane components and mitigation of common mode voltage, DC bus utilization. However, these SVM-DTC schemes involved complex duty cycle calculations which need fast DSP controllers. The SVM-DTC exhibits slower dynamics parameter sensitivity. In [44]-[45], a carrier-based constant switching torque controller is implemented on a 3-phase induction motor and it affects machine dynamics and flux ripple respectively. The 5-level constant switching torque controller-based DTC implemented in a 5-phase induction motor with the simulations results however, this method exhibits high xy-plane components due to medium vectors.

Multi-level inverter-fed induction motor drives getting good attention in medium and high-power industries due to their advantages like improved voltage profile, reduced EMI effect, fault-tolerance, reduced switching frequency, and reduced/zeroed common mode voltage [46]. Several research works have been done in the literature on different MLI-fed 3-phase drives [47]-[49]. In [47], a modified DTC is implemented on a neutral point inverter-controlled 3-phase drive and addresses the DC link voltage fluctuations. In [48], a DTC is implemented on a cascaded H-bridge-based MLI-fed 3-phase induction motor to improve the voltage profile which requires independent DC sources. In [49], DTC is implemented on a flying capacitor-based MLI-fed 3-phase induction motor which suffers from voltage balancing issues, and variable capacitor stresses. The researchers started to focus on MLI-fed 5-phase induction motors to combine the advantages associated with the MLI and multi-phase drives. In [50], a DTC with five-level and seven-level torque controllers for a 3-level neutral point clamped-converter fed 5-phase induction motor is executed which suffers drawbacks associated with the converter such as capacitor imbalance and neutral point shifting. In [51], a modified DTC with a novel neutral point balancing scheme is implemented in a 3-level neutral point inverter-fed 5-phase induction motor.

Apart from above mentioned various multi-level inverter topologies, dual inverter configuration attains good attention due to their special features like reduced DC-link voltage, no capacitor neutral balance issue, no need of clamping diodes, and no flying capacitors required, and simple configuration [52]. Recently several researchers focused on working on dual-inverter controlled 5-phase induction motors to adopt features associated with dual inverter configuration [53]-[58]. In [53] and [54], two different space voltage vector modulation schemes are implemented to eliminate common mode voltage/current in dual inverter-controlled open-end winding five-phase induction motor (FP-OEWIM). A 9-level torque controller-based DTC is implemented in [55] with the developed four sets of voltage

vectors in a dual inverter-controlled FPOEWIM to reduce torque and flux ripple but the author does not consider harmonic plane components which creates unnecessary power loss and common mode voltage not taken into consideration. In [56], a basic 3-level hysteresis torque controller is employed in DTC of dual inverter-controlled FPOEWIM with 10 virtual voltage vectors (VVV) and it exhibits high flux torque ripple and current harmonic content. A new 5-level torque controller is introduced in DTC of dual inverter fed FPOEWIM with 20 VVV to reduce flux ripple torque ripple and current THD [57] and still, it exhibits high torque-flux ripple, and current distortion and does not eliminate harmonic plane components. In [58], the author extended the work done in [57] by eliminating harmonic plane components in a dual inverter-controlled 5-phase induction motor

1.5 Motivations

From the extensive literature review, it is observed that

- The 5-phase induction motor has some special features like fault-tolerant capability, high torque density, lightweight, smooth operation, and reduced copper losses when compared with conventional 3-phase machines, which encourages the use of the 5-phase machine in battery-powered electrical mobility, electric traction, ship propulsion, electric aircraft.
- The 5-leg inverter is a simple circuit configuration to drive the 5-phase induction motor which avoids the neutral point balancing issues, clamping diodes, and capacitor balancing issues, unlike other inverter topologies.
- The existing hysteresis-based DTC schemes offer good dynamic performance, but these will exhibit poor steady-state performance in terms of torque ripple, flux ripple, current distortion, and variable switching frequencies due to the application of vectors over complete sample time.
- The existing duty cycle control-based DTC methods improve the steady-state performance of the FPIM drive, which requires extensive calculations and causes a computational burden. These duty-based DTC schemes depend on the accuracy of machine parameters and increase the switching frequency due to multiple vector selection in one sample period.
- The DTC control schemes for multi-level inverter topologies further improve the steady-state performance of the drive and it necessitates the use of MLIs in high power density industrial drives. Among various MLI topologies, dual inverter configuration gains good attention due to their simple structure,

increased fault tolerance, increased switching redundancies, and reduced switch voltage rating.

- Application of dual inverter configuration for 5-phase open-end winding induction motor triggers combined advantages of dual inverter and 5-phase motors.

1.6 Thesis Contributions

The contributions and the novelty of this thesis are presented below

1. A modified DTC on 2-level VSI-fed FPIM is implemented with a constant switching torque controller (CST) to improve the steady-state performance in terms of average torque ripple and current harmonic distortion with nearly constant switching frequency under various operating speeds without disturbing the dynamics. The CST controller allows the duty cycle of the active voltage vector to finely vary with rotor speeds, thereby influencing torque ripple with speed variations. Consequently, the proposed CST controller is expected to result in a substantial reduction of torque ripple at low speeds. The proposed CST undergoes state changes at regular intervals, causing the switching frequency to remain almost constant, as it primarily depends on changes in the torque controller status. The slower dynamics caused by the frequent zero selection in the proposed CST controller are improved by employing an FOPI controller within the CST controller.
2. A modified Direct Torque Control (DTC) scheme is proposed, incorporating a Constant Switching Flux (CSF) controller and a Constant Switching Torque (CST) controller, replacing the hysteresis-based flux and torque controllers, respectively. The aim is to reduce flux ripple, torque ripple, and current harmonic distortion without compromising dynamic behaviour. The proposed DTC scheme combines the advantages associated with both CSF and CST controllers. The proposed DTC scheme is implemented with virtual voltage vectors to make zero harmonic plane components. The proper design of the CSF controller and CST controller with the help of machine electrical dynamic equations reduces the flux ripple, torque ripple, and current harmonic distortion. The initial testing involves assessing the performance of the CSF controller within classical DTC. Subsequently, a CST controller is introduced alongside the CSF controller, replacing both hysteresis-based torque and flux controllers without disturbing the generality of the classical DTC method to improve both flux ripple and torque ripples and the current %THD of the 5-phase induction

motor. The slower dynamics of the proposed scheme improved with the FOPI controller to maintain a fast dynamic as that of the hysteresis-based DTC schemes.

3. A Slip Speed Control direct flux control (SSC-DFC) method introduces simplified lookup tables on a fed 5-phase induction motor to improve the torque profile, flux profile, and current profile. The proposed SSC-DFC scheme employs a voltage controller with a simple sample-based voltage error tracking using 20 virtual voltage vectors with simplified two lookup tables under high-speed and low speeds. The voltage controller changes the switching state for every sample period and hence maintains constant switching frequency at variable speeds under various loading conditions.
4. A DTC control scheme is proposed, incorporating two modified lookup tables applied to a dual inverter-fed open-end winding induction motor (DIFPOEWIM). This approach aims to combine the benefits of both the dual inverter configuration and the 5-phase induction motor. The proposed DTC method for DIFPOEWIM employs a 7-level torque controller at high speeds, utilizing all 30 voltage vectors to mitigate torque ripple and current harmonic distortion. Additionally, a 3-level torque controller is employed at lower speeds, utilizing a smaller set of voltage vectors to minimize both flux and torque ripple, as well as current harmonic distortion. The proposed method generates 30 voltage vectors in a dual inverter configuration by utilizing adjacent and nonadjacent virtual voltage vectors from individual inverters while maintaining 72^0 and 144^0 phase displacement. This ensures the zero resultant common mode voltage for the dual inverter configuration. Additionally, the proposed method eliminates harmonic plane components using virtual voltage vectors through the volt-sec balance method.

1.7 Organization of the Thesis

The thesis is organized as follows.

Chapter 1 provides an overview of the 5-phase induction drive and its modeling. The chapter discusses the fundamental concept of the 5-leg voltage source inverter and explains the locations of its switching vectors. Additionally, a literature survey is presented, covering the evolution of multi-phase induction motors, their speed control schemes, and the associated drawbacks and advantages. Finally, the motivations behind the proposed research work and its contributions are discussed in this chapter.

Chapter 2 presents the operation and drawbacks of the existing DTC method of 5-phase induction motor. This chapter discusses the design and functionality of the CST controller along with the implementation of the proposed CST-DTC scheme for reducing the torque ripple and current harmonic distortion along with dynamic behavior. This chapter presents the design constraints of the PI controller and FOPI controller of the CST controller with valid mathematical analysis. Experimental results of the proposed CST-DTC method are presented, and these findings are systematically compared with the experimental results obtained from classical DTC for a comprehensive and unbiased analysis.

Chapter 3 introduces the concept of the virtual voltage vector to eliminate harmonic plane components using the volt-sec balance technique. The chapter covers the conceptualization and design of a constant switching flux (CSF) controller and a constant switching torque (CST) controller. Design constraints for the proposed CSF controller are discussed based on the flux dynamic equations. The hardware results of the proposed method are initially presented with only a CSF controller, followed by the discussion of the hardware experimental results of the proposed scheme with both CST and CSF controllers. These results are then compared with the test outcomes of different existing DTC control schemes for a 5-phase induction motor.

Chapter 4 presents the operation of the proposed slip control-based direct flux control (SSC-DFC) in the 5-phase induction motor to reduce the torque ripple and flux ripple and current %THD along with the constant switching frequency. This chapter explains switching voltage vector selection with a simplified lookup table. In this chapter, the proposed SSC-DFC method is experimentally tested and the results are compared with existing DTC control schemes of 5-phase induction motor.

Chapter 5 presents the mathematical modeling and analysis of the open winding 5-phase induction motor using two 2-level 5-leg inverters having a common DC supply. Different voltage space vectors produced by dual inverter configuration across the open-end winding 5-phase induction motor with the concern of making zero common mode voltage are presented and discussed. The implementation of 30 vectors based on 7-level and 3-level DTC is discussed with modified lookup tables. The effectiveness of the proposed DTC of the OEWFPIM is discussed in this chapter with supporting hardware results.

Chapter 6 summarizes the key findings of the research work stated in this thesis. It also recommends possible extensions for the upcoming work.

Chapter 2

A novel Constant Switching Torque Controller-based DTC of 5-phase Induction Motor Drive

Chapter 2

A novel CSF Torque Controller-based DTC of 5-phase Induction Motor Drive

2.1 Introduction

The hysteresis-based direct torque control (DTC) technique is a widely used vector control technique in modern industrial drives due to its numerous advantages such as independent control of torque and flux, less parameter sensitivity, no complex coordination transformation required, and quick dynamics. The conventional DTC suffers from variable switching frequency and higher torque and flux ripples due to its hysteresis-based controller. The torque ripple can be reduced in DTC controlled drive with reduced band width of hysteresis controller with the cost of increased switching frequency. Also, the torque ripple cannot be reduced further by shortening the hysteresis band due to time delay with slow-operating DSP controllers while implementing control algorithms. So, it is mandatory to follow a tradeoff between switching frequency and torque ripple and processor computational speed while implementing DTC control of any electrical drive. Several modified DTC schemes were implemented on conventional 3-phase induction motor/PMSM drives in literature to improve the steady-state performance in terms of torque ripple, flux ripple, and variable switching frequency. The torque ripple can be reduced by implementing duty-based voltage vector selection in DTC control of the electric drive without changing the bandwidth of the torque controller. Various duty-based control techniques were implemented on a 5-phase induction motor to reduce torque ripple however these control schemes suffer from system complexity, computation burden, and high switching frequency.

In DTC, the torque ripple is influenced by the duration of the active voltage vector selection. This selection is controlled by the torque controller. To minimize torque ripple, it is essential to regulate the duration of the active voltage vector selection. This duration, in turn, relies on two key parameters: the hysteresis bandwidth and the sampling period. A narrower hysteresis bandwidth results in more frequent vector changes, potentially reducing torque ripple with the cost of increased switching frequency. A shorter sampling period allows the controller to respond more quickly to changes in motor conditions, affecting the duration of the active vector which needs fast-operating DSP controllers. The switching frequency mainly depends on the direct control technique's torque controller status change (T_{stat}) rate. In the

classical DTC scheme, the hysteresis torque controller changes its state irregularly and hence the switching frequency is variable throughout drive operation. The proposed DTC control scheme on 5-phase induction introduces the carrier-based constant switching torque controller (CST) to reduce torque ripple and current harmonic distortion and maintain nearly constant switching frequency without implementing complex duty-based control schemes. The CST controller replaces the classical hysteresis torque controller without disturbing the generality of the classical DTC structure.

2.2 Operation of Constant Switching Torque (CST) controller

Figures 2.1(a) and 2.1(b) show the implementation of the classical hysteresis torque controller and constant switching torque controller respectively. The CST controller is implemented with two triangular carrier waves (C_{upper} and C_{lower}) with 180^0 phase difference and PI controller and two comparators as shown in Figure 2.1(b). The proposed constant switching torque (CST) controller status will be +1, 0, or -1, similar to a classical 3-level hysteresis controller. The key difference is the proposed CST controller is forced to change its status based on triangular carrier frequency as shown in Figure 2.2(b). This operation of the CST controller ensures that the switching frequency remains nearly constant as the switching frequency mainly depends on the torque controller [59]. On the other hand, the hysteresis-based torque controller exhibits irregular torque status changes (T_{stat}) as shown in Figure 2.2(a) and it is influenced by operating speeds and applied DC link voltage.

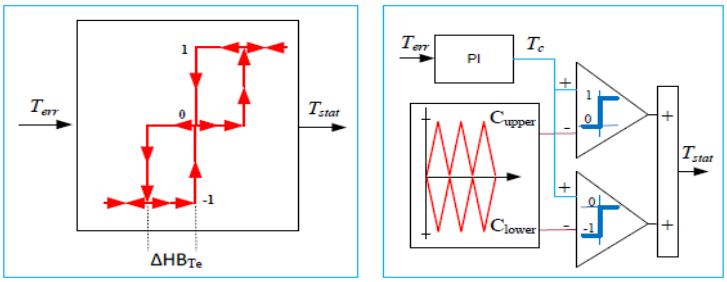

Figure 2.1 Implementation of three-level hysteresis torque controller and constant switching torque controller

The CST controller output status (T_{stat}) gives +1 or 0 or -1, as that of the hysteresis controller of the classical DTC as described below

$$\begin{aligned} T_{stat} &= 1 \quad T_c \geq C_{upper} \\ T_{stat} &= 0 \quad C_{lower} < T_c < C_{upper} \\ T_{stat} &= -1 \quad T_c \leq C_{lower} \end{aligned} \tag{2.1}$$

In equation 2.1, T_c is the output of the PI controller of the CST controller, and the CST controller output (T_{stat}) statuses are 1, –1, and 0 means torque needs to increase, decrease, and no change respectively.

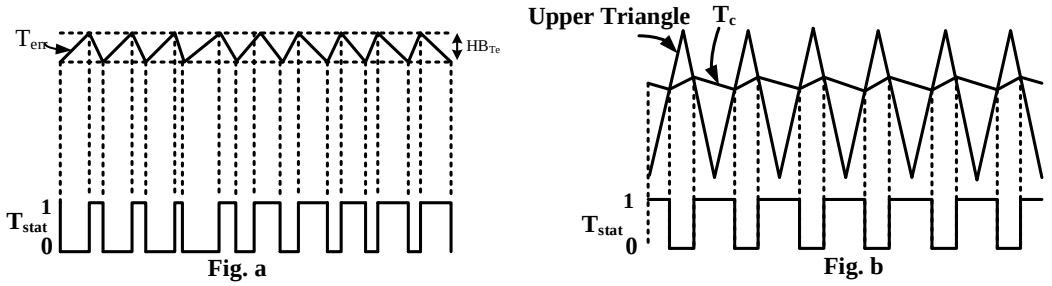

Figure 2.2 Operation of a) hysteresis-based torque controller b) constant switching torque controller

In the proposed CST-DTC control method, the duration of the active voltage vector mainly depends on the duty (T_c), which is the output of the PI controller in the CST controller. This duty changes w.r.t operating speeds through the actions of the PI controller. For higher speeds, T_c is more and the duration of the active voltage vector is more as in Figure 2.3(a). Similarly, the T_c is reduced for lowering the speeds, and the duration of the active vector is reduced as in Figure 2.3(b) causing more reduction of torque ripple. Hence the proposed CST-DTC control method greatly reduces the torque ripple under low speeds rather than high speeds. The PI controller is designed such that the value of T_c should be within triangular carrier bands under steady-state for rated speeds.

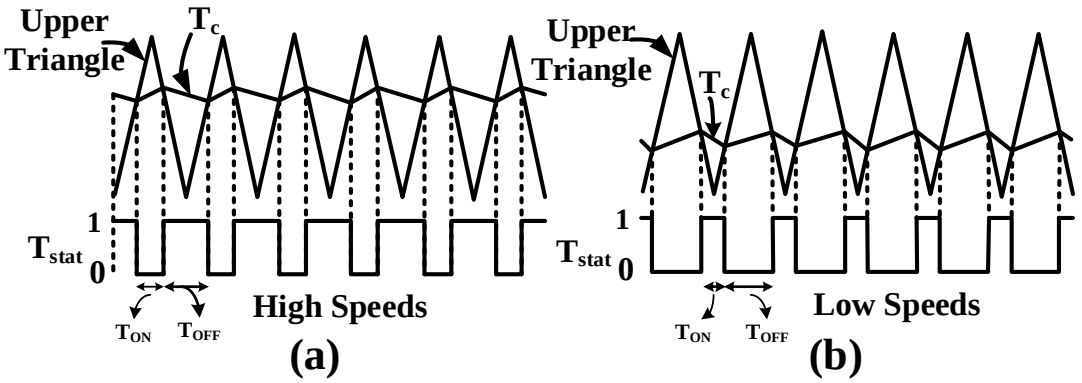

Figure 2.3 Variation of duty of CST controller output for a) high speeds and b) low speeds

During load torque transients, T_c may touch the C_{upper} peak value and fall back to carrier bands resulting in zero vector selection which causes slower transients when compared with hysteresis-controlled DTC schemes as shown in Figure 2.4. These poor dynamics are improved by using the fractional order PI controller in place of integer order PI control.

The dynamics are improved by the proper design of the FOPI-CST controller such that it should increase the duration of the active voltage vector during transient conditions.

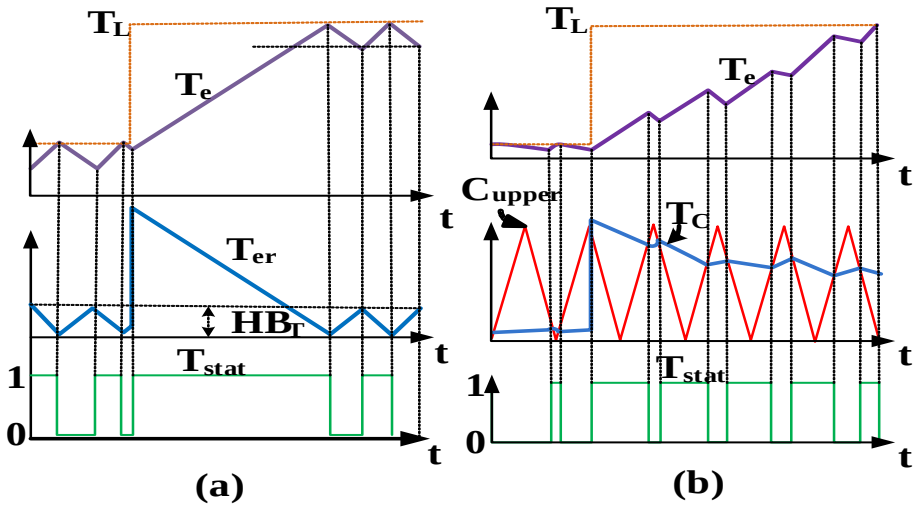

Figure 2.4 Load dynamics response for (a) Classical DTC method (b) CST-DTC method

2.3 Design of Constant Switching Torque (CST) controller

2.3.1 Design of PI-based CST controller

In the constant switching torque controller shown in Figure 2.1(b), the design of the K_p and K_i parameters of PI is significant for stable operation. The K_p and K_i parameters are designed using the torque loop transfer function which is designed based on five-phase induction motor torque dynamic equations along with the CST controller. The torque loop transfer function is averaged and linearized [43] for the design of K_p and K_i selection. As the PI controller output is assumed as constant within one triangular cycle, the relation between T_c and duty ratio (d) is reciprocal of peak to peak of triangular signal ($C_{p\text{-}p}$) as in (2.2).

$$\frac{d}{T_c} = \frac{1}{C_{P-P}} \tag{2.2}$$

The Transfer function between $d(s)$ and $T_e(s)$ can be obtained by averaging positive torque slope (2.3) and negative torque slope (2.4) [43].

$$\frac{dTe^{+}}{dt} = -T_e\left(\frac{1}{\sigma\tau_s}+\frac{1}{\sigma\tau_r}\right)+\frac{5}{2}\frac{P}{2}\frac{L_m}{\sigma L_s L_r}\left(-v_{ds}\,\Psi_{qr}+v_{qs}\,\Psi_{dr}-\omega_r\left(\Psi_{ds}\,\Psi_{dr}+\Psi_{qs}\,\Psi_{qr}\right)\right) \tag{2.3}$$

$$\frac{dTe^{-}}{dt} = -T_e\left(\frac{1}{\sigma\tau_s}+\frac{1}{\sigma\tau_r}\right)-\frac{5}{2}\frac{P}{2}\frac{L_m}{\sigma L_s L_r}\left(\omega_r(\Psi_{ds}\Psi_{dr}+\Psi_{qs}\Psi_{qr})\right) \tag{2.4}$$

In the stator flux reference frame theory, it is assumed as Ψ_{qs}=0, Ψ_{ds}= Ψ_s, and Ψ_{dr}= Ψ_r, and for the sake of simple design, the angle between the stator and rotor flux is negligible, and the d-axis voltage component is zero. From (2.3) and (2.4), it can be rewritten as

$$\frac{dTe^{+}}{dt} = -T_e\left(\frac{1}{\sigma\tau_s}+\frac{1}{\sigma\tau_r}\right)+\frac{5}{2}\frac{P}{2}\frac{L_m}{\sigma L_s L_r}\left(v_s\,\Psi_r-(\omega_r-\omega_s)\,(\Psi_s\,\Psi_r)\right) \tag{2.5}$$

$$\frac{dTe^{+}}{dt} = -T_e\left(\frac{1}{\sigma\tau_s}+\frac{1}{\sigma\tau_r}\right)+\frac{5}{2}\frac{P}{2}\frac{L_m}{\sigma L_s L_r}\left(-(\omega_r-\omega_s)(\Psi_s\,\Psi_r)\right) \tag{2.6}$$

Where ω_s=stator flux frequency=ω_e/d; ω_e=synchronous frequency;

d=duty cycle; ω_r=rotor frequency

Taking constant terms into consideration, equations (2.5), and (2.6) further can be simplified below

$$\frac{dTe^+}{dt} = -A_t T_e + B_t v_s + K_t\left(\frac{\omega_e}{d} - \omega_r\right) \tag{2.7}$$

$$\frac{dTe^-}{dt} = -A_t T_e + K_t \omega_r \tag{2.8}$$

Where

$$A_t = \frac{1}{\sigma\tau_s} + \frac{1}{\sigma\tau_r}$$

$$B_t = \frac{5}{2}\frac{P}{2}\frac{L_m}{\sigma L_s L_r}\ \Psi_r$$

$$K_t = \frac{5}{2}\frac{P}{2}\frac{L_m}{\sigma L_s L_r}\ \Psi_s \Psi_r$$

By averaging and simplifying (2.7) and (2.8),

$$\frac{dT_e}{dt} = -A_t T_e + B_t v_s d + K_t \omega_{slip} \tag{2.9}$$

Equation (2.9) can be linearized by inserting small perturbations in ω_{slip}, T_e, and d. The small-signal transfer function model can be obtained as

$$\hat{T}_e = \frac{B_t v_s \hat{d} + K_t \hat{\omega}_{slip}}{s + A_t} \tag{2.10}$$

$$0 = -A_t T_e + B_t v_s d + K_t \omega_{slip} \tag{2.11}$$

In (2.10), the slip frequency term is very small when compared with other adding terms and it can be neglected. The complete torque loop transfer function can be written as in (2.12).

$$\hat{T}_e = \frac{B_t v_s \hat{d}}{s + A_t} \tag{2.12}$$

The complete block diagram of the closed-loop torque transfer function model with a constant switching torque controller is represented in Figure 2.5 from (2.2) and (2.12).

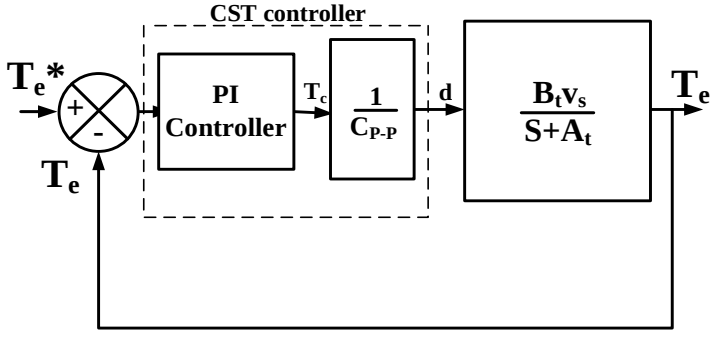

Figure 2.5 Block diagram of closed loop torque transfer function with CST controller

With the introduction of the PI controller in series with the torque loop, an integrator is introduced to the open-loop torque transfer function and it gives infinite steady-state gain and makes steady-state error zero because of the already existing pole in the open-loop torque transfer function.

The triangular carrier signal with a frequency of 1250 Hz with peak-peak magnitude (C_{p-p}) of 100 units is generated in MATLAB/Simulink software with a sample time of 100μs. So, the number of steps in the triangular carrier will be eight over a peak-to-peak magnitude (C_{p-p}) of 100 units. The slope of the triangular carrier will be 250000 units/sec.

The absolute slope of torque should not be more than the absolute slope of the triangular carrier signal henceforth proportional gain K_p is calculated from the below equations
from the positive slope equation (2.7)

$$|\textit{Slope of triangular carrier}| >= \left\{-A_t T_e + B_t v_s + K_t\left(\frac{\omega_e}{d} - \omega_r\right)\right\} * K_p \tag{2.13}$$

from negative slope equation (2.8)

$$|\textit{Slope of triangular carrier}| >= \{-A_t T_e + K_t \omega_r\} * K_p \tag{2.14}$$

The maximum slope of the torque signal that limits the gain K_p such that it should be less than the slope of triangular occurs at a maximum slip of 6.28 rad/sec and zero rotor speed. Substituting the machine parameters and numerical data in (2.13) gives $K_p \leq 88.71$. The inverter DC voltage is chosen as 100V to achieve maximum rotor speed and the maximum absolute negative slope occurs at the rated speed i.e., 150.72 rad/sec. From equation (2.14), the proportional gain K_p is calculated as $K_p \leq 614$. And the optimal value of K_p is chosen to satisfy both values i.e $K_p \leq 88.71$

The integral controller gain K_i has been selected such that the zero of the PI controller transfer function is the same as the pole in the averaged torque loop function in Figure 2.5 and shown in (2.15)

$$s + \frac{K_i}{K_P} = s + A_t$$

$$K_i = A_t K_p \tag{2.15}$$

If the zero of the PI controllers is chosen to be the same as the pole of the open-loop torque transfer function, the value of K_i is obtained and is $K_i < 18898.44$.

2.3.2 Design of FOPI Controller

The fractional-order PI controller is introduced based on fractional-order control theory [60] and used to improve the dynamic performance of the drive without affecting the system's steady-

state performance. The fractional order PI (FOPI) controller significantly enhances the dynamics of motor drives compared to traditional integer order PI control by using the principles of fractional calculus theory. Fractional calculus introduces fractional orders for the integral and derivative actions which provide additional degrees of freedom for tuning the controller. This added flexibility allows for more precise control adjustments, enabling the FOPI controller to fine-tune the dynamic response of the motor drive more effectively than a traditional PI controller[61]. As a general control system theory, increasing the order of the integrator in a control system typically reduces stability and increases oscillatory behavior, leading to decreased damping. This results in longer settling times and poorer system dynamics. Conversely, in the case of a fractional order integrator, the integrator's order is reduced, which improves stability and increases damping. This reduction in oscillatory behavior allows the system to settle more quickly, enhancing the overall dynamic performance. As a result, the FOPI controller can achieve reduced overshoot, reduced oscillations and faster settling times, leading to a smoother transient response and fastens the dynamics. Furthermore, the fractional order nature of the FOPI controller extends its frequency response capabilities like bandwidth, phase margin and gain margin, offering better robustness and stability across a wide range of operating conditions and disturbances[62]. This makes the motor drive system more resilient to load variations and external perturbations.

Increasing the bandwidth of a traditional Proportional-Integral (PI) controller enhances its dynamic response by enabling quicker correction of errors, thereby reducing settling time, minimizing overshoot, and improving overall system stability. This improvement is achieved through adjustments in proportional and integral gains, ensuring the controller responds more swiftly to changes in the error signal which may lead to unstable and peak overshoots. Whereas the fractional order PI (FOPI) controllers offer additional advantages through their ability to finely tune integral and derivative actions with non-integer orders, providing enhanced flexibility and potentially superior control dynamics.

Among different generations of fractional controllers, the fractional order PID (FOPID) controller exhibits a strong suppression effect of disturbances and hence the robustness of the FOPID controller is much better than the traditional integral order PI controller. Unlike integer order PI controller, which are limited to fixed integral and derivative actions, the FOPID controller allows for fractional orders to be finely tuned. This flexibility enables the FOPID controller to tailor its response more accurately to the dynamic characteristics of the controlled system. For example, in applications like motor drives where quick and precise adjustments are crucial to maintain desired speeds or positions, the FOPID controller can achieve faster settling

times and reduced overshoot compared to PI controllers. Different methods were proposed in the literature for tuning FOPID controllers such as optimization algorithms methods [63], dominant pole algorithms method [64], and phase-amplitude margin methods [63]-[64]. In this work, the phase-amplitude margin method [65]-[66] is followed to design a robust FOPID controller.

The fractional-order PID controller design procedure for selecting proportional gain K_p is the same as the design of proportional gain K_p in PI-based CST controller such that it should not disturb the steady-state performance as that of the PI-CST-DTC method and differs in the design of integrator gain K_i and integrator order (δ). The integrator gain (K_i) and integrator order (δ) are calculated from the phase margin φ_m and robustness of plant system conditions.

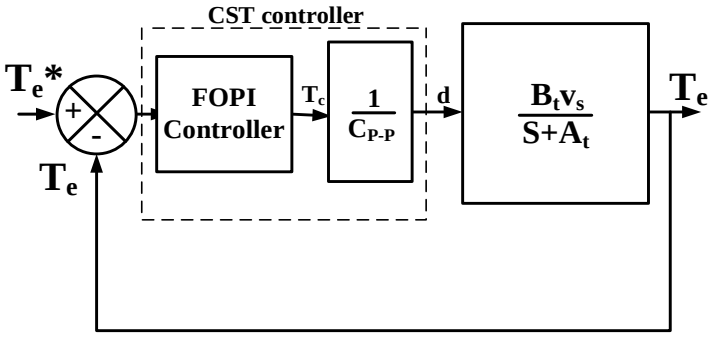

Figure 2.6 Block diagram of closed loop torque transfer function with FOPI-CST controller

The closed-loop diagram of the plant torque model with the FOPI controller is shown in Figure 2.6. The open-loop transfer function from Figure 2.6 can be written below

$$G(s) = K_p\left(1 + \frac{K_i}{S^\delta}\right)\left(\frac{1}{C_{p-p}}\right)\left(\frac{B_t v_s}{S+A_t}\right) \tag{2.16}$$

Equation (2.16) can be simplified as below

$$G(s) = C_t\left(1 + \frac{K_i}{S^\delta}\right)\left(\frac{1}{S\tau+1}\right) \tag{2.17}$$

Where $C_t = \frac{K_p B_t v_s}{C_{p-p} A_t}$, $\tau = \frac{1}{A_t}$, $S = j\omega$

The open-loop system transfer function *G(s)* would meet the following design specifications to design the FOPI controller.

i) The phase angle of *G(jω)* at the crossover frequency ω_c can be written as

$$Arg[G(j\omega)]_{\omega=\omega_c} = \varphi_m - \pi$$

$$-\frac{atan\left(K_i\omega_c^{-\delta} sin\left(\frac{\delta\pi}{2}\right)\right)}{1+K_i\omega_c^{-\delta} cos\left(\frac{\delta\pi}{2}\right)} - atan(\tau\omega_c) = \varphi_m - \pi \tag{2.18}$$

From equation (2.18), K_i can be expressed as a function of δ as below

$$K_i = \frac{-tan\,[atan(\tau\omega_c)+\varphi_m]}{\omega_c{}^{-\delta}\,cos\frac{\delta\pi}{2}+\omega_c{}^{-\delta}cos\,\frac{\delta\pi}{2}tan\,(atan(\tau\omega_c)+\varphi_m)} \tag{2.19}$$

ii) Robustness to gain margin (φ_m) variations of the plant can be expressed as

$$\frac{d}{d\omega}[arg\,(G(j\omega))]_{\omega=\omega_c} = 0$$

$$\frac{K_i\delta\omega_c{}^{-\delta}\,sin\left(\frac{\delta\pi}{2}\right)}{\omega_c{}^{2\delta}+2K_i\omega_c{}^{\delta}\,cos\left(\frac{\delta\pi}{2}\right)+K_i{}^2} = \frac{\tau}{1+(\tau\omega_c)^2} \tag{2.20}$$

For tuning the FOPI controller, the gain cross-over frequency and phase margin are considered 500 rad/sec and 45^0. The equations (2.19) and (2.20) can be solved for optimal integrator gain K_i and integrator fractional order (δ) such that it should satisfy both (2.19) and (2.20). A Simple graphical approach can be adopted for solving both equations (2.19) and (2.20) as shown in Figure 2.7. The graph is drawn between integrator order and integrator gain K_i by varying for both (2.19)and (2.20) as in Figure 2.7. The crossing point of two curves corresponding to (2.19) and (2.20) is treated as the optimal point for integrator gain (K_i) and integrator order (δ)and these values are 13500 and 0.305 respectively.

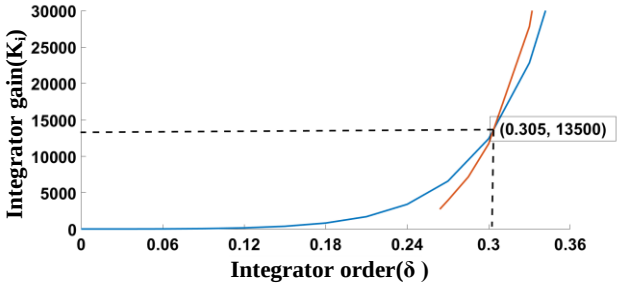

Figure 2.7 Variation of integrator gain (K_i) with integrator order (δ)

2.4 Implementation of the proposed DTC scheme in FPIM

The proposed CST DTC scheme improves both high and low-speed performance in terms of torque ripple and harmonic current distortion and inverter switching frequency using a single lookup table with fine adjustment of duty of active voltage vectors with different operating speeds without disturbing the fast dynamic performance of the drive.

In the Direct Torque Control (DTC) scheme [35], the desired changes in torque (ΔT_e) and flux ($\Delta \Psi_s$) can be achieved by applying suitable voltage vectors within a sample period T_s. This process directly influences the flux, as described in equation (2.21), where the flux is affected by the applied voltage throughout T_s. Moreover, the torque primarily responds to changes in the stator flux angle w.r.t the rotor flux vector ($\Delta\theta$), as outlined in equation (2.22) and shown in Figure. 2.8.

$$\Delta \Psi_s = (V_s - R_s i_s)\Delta T_s \tag{2.21}$$

$$\Delta T_e = \frac{5}{2}\frac{P}{2}\frac{L_m}{L_r L_{ss}}(|\Psi_s + \Delta \Psi_s|)(|\Psi_r|)\, sin(\Delta\theta) \tag{2.22}$$

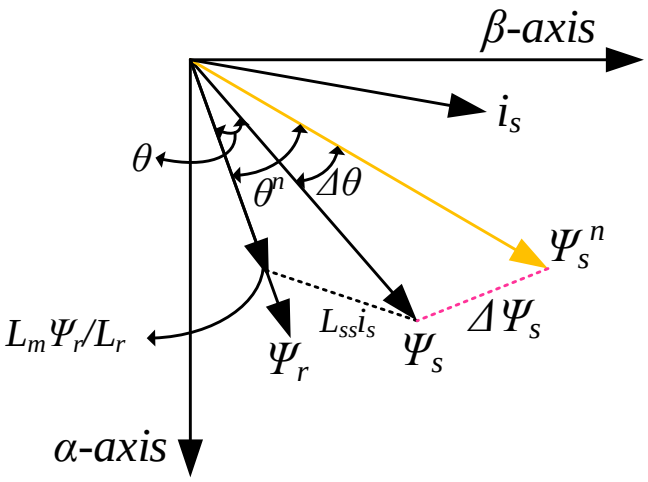

Figure 2.8 Phasor representation of basic DTC operation

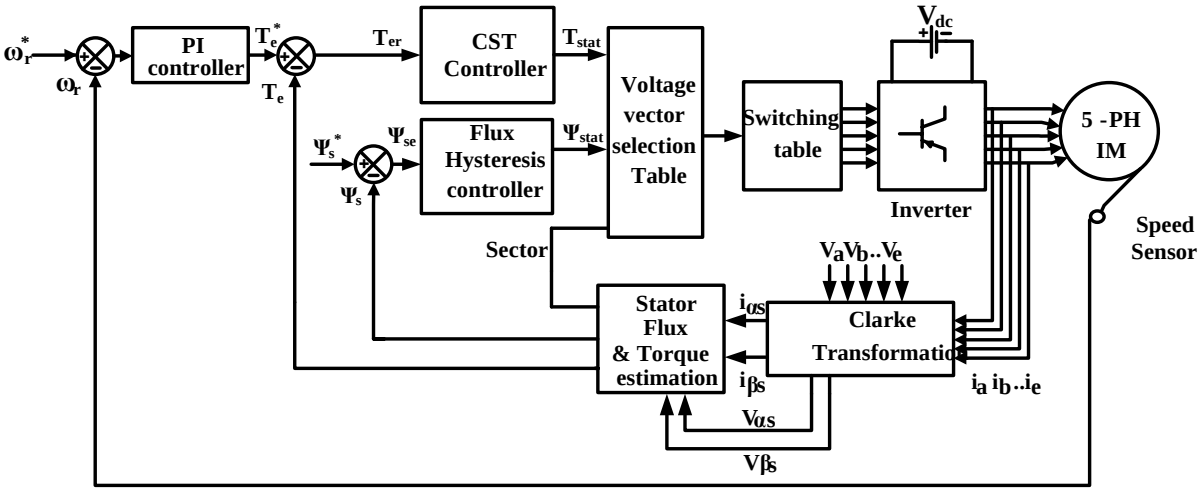

Figure 2.9 Block diagram representation of the proposed PI-CST-DTC, FOPI-CST-DTC schemes of five-phase Induction Motor

The block diagram representation of the proposed DTC method of a two-level voltage source inverter-fed five-phase induction drive is shown in Figure. 2.9 and the proposed DTC replaces the classical hysteresis torque controller with the proposed constant switching torque (CST) controller. The block diagram consists of a speed encoder, torque-flux estimation block, speed PI controller, constant switching torque controller, flux hysteresis controller, voltage source inverter, and five-phase induction motor drive. The speed error is processed with the PI controller and generates ref. torque (T_e^*) command. The estimated stator flux (Ψ_s) and electromagnetic torque (T_e) from (4), and (5) are compared with reference stator flux Ψ_s^* and

reference torque (T_e^*) respectively. With the information of torque error, stator flux error, and flux sector information; the suitable switching states are chosen as in lookup Table 2.1.

Table 2.1 Switching state table for C-DTC[35] & CST-DTC schemes

Ψ_{stat}	T_{stat}	Sector									
		1	2	3	4	5	6	7	8	9	10
1	1	24	28	12	14	6	7	3	19	17	25
	0	0	31	0	31	0	31	0	31	0	31
	-1	17	25	24	28	12	14	6	7	3	19
-1	1	14	6	7	3	19	17	25	24	28	12
	0	31	0	31	0	31	0	31	0	31	0
	-1	7	3	19	17	25	24	28	12	14	6

The stator flux and electromagnetic torque are estimated from motor dynamic equations as shown below.

The stator voltage balancing equation can be written as (5.16)

$$V_s = I_s R_s + \frac{d\Psi_s}{dt} \tag{5.16}$$

Where V_s = stator phase voltage in volts

I_s= stator phase current in amperes

R_s=stator resistance in ohms

The estimation of stator flux (Ψ_s) can be done as shown in (5.17)

$$\Psi_s = \int (V_s - I_s R_s)\, dt \tag{5.17}$$

The estimation of electromagnetic torque (T_e) can be done as below (5.18)

$$T_e = \frac{5}{2}\frac{P}{2} imag(\Psi_s^* I_s) \tag{5.18}$$

Where P- Induction motor stator poles

The constant switching torque (CST) controller replaces the classical three-level hysteresis torque controller of C-DTC in the proposed CST-DTC methods. Whereas the two-level flux hysteresis controller will be the same for both methods to control stator flux as shown in Figure 2.9. The CST and flux hysteresis controller give torque error status (T_{stat}) as 1, -1, 0, and flux error status (Ψ_{stat}) as 1, -1 respectively. Therefore, CST-DTC won't indulge the generality of C-DTC. The three-level CST controller is mainly equipped with PI controller, upper triangular (C_{upper}), and lower triangular (C_{lower}) carrier signals with 180^0 phase shift and comparators as in Figure. 2.1

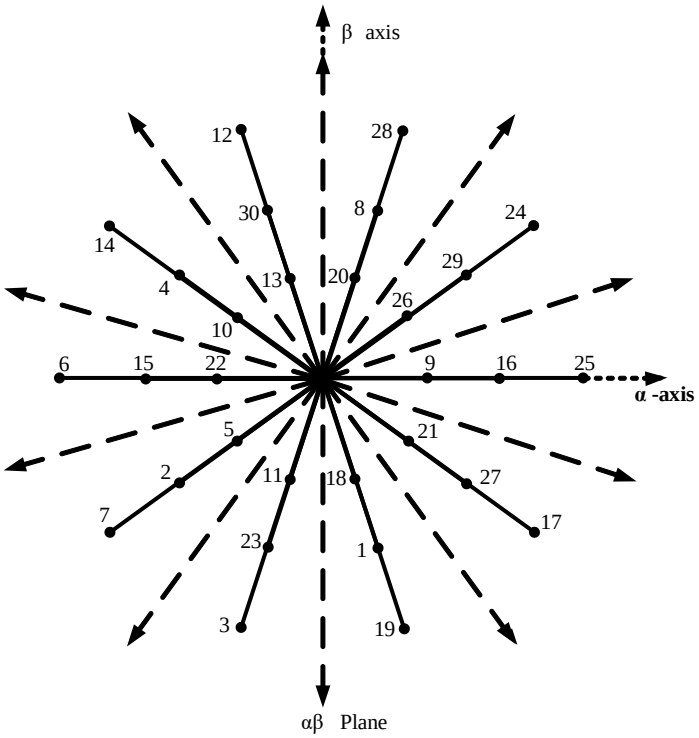

Figure 2.10 Space vector locations in fundamental (αβ) plane

2.5 Experimental Result and Discussion

The proposed CST-DTC methods are experimentally tested and compared with the C-DTC method on a five-leg inverter-fed five-phase induction motor to know the effectiveness of the proposed DTC scheme. The experimental setup shown in Appendix I is used for experimentation. To achieve a fair comparison, the C-DTC [35] is implemented with hysteresis bands, resulting in an average switching frequency of 1.25 kHz, which closely matches the switching frequency of the proposed PI and FOPI-based DTC schemes with a common sampling period of 100 μsec. In the experimental setup, the control algorithm is executed on a dSPACE-1202 controller using real-time interfacing with MATLAB/Simulink software. The motor drive being tested comprises a 5-phase 1 HP induction motor coupled with a 1 HP DC generator. This DC generator is loaded with resistive lamp loads. In the testing setup, the 5-leg inverter incorporates an IGBT-based five-phase inverter power module. This module features a built-in driver circuit board that receives gating signals from the dSPACE controller. This inverter module is supplied with a variable DC link voltage. The 1024 PPR digital speed encoder is utilized to accurately track the speed of the 5-phase induction motor. The 5-phase currents and DC link voltage are sensed using LEM LA-25P current sensors and LV-25P voltage sensors, respectively. The analog signals obtained from the sensors are converted to digital format through the onboard Analog-to-Digital Converter (ADC) on the dSPACE controller board.

These digital signals are then employed in the implementation of the control scheme. The classical Direct Torque Control (C-DTC) and the proposed PI-CST-DTC and FOPI-CST-DTC methods are implemented with a common flux hysteresis band ($HB_{\Psi e}$) set at 4% of the rated flux. Additionally, in the case of Conventional DTC (C-DTC) [35], a hysteresis torque band ($2*HB_{Te}$) is applied, representing 10% of the rated torque. The effectiveness of the proposed PI and FOPI-based Constant switching torque controller-based Direct Torque Control (CST-DTC) methods, as well as the classical DTC methods, is tested under both steady-state and transient conditions. The steady-state performance for both classical and proposed Direct Torque Control (DTC) methods is evaluated across various speeds and loads to test the performance and robustness of the proposed approach. This assessment includes the analysis of key parameters such as torque ripple, current harmonic distortion, and switching frequency. Transient conditions involve a step change in load and speed commands.

2.5.1. Steady state performance analysis

The steady-state performance, considering torque ripple, flux ripple, and current total harmonic distortion (*%THD*), is thoroughly examined at both high speed (1400 rpm) and low speed (50 rpm) under light load and load conditions in a 5-phase induction motor drive. This comprehensive analysis includes both classical Direct Torque Control (DTC) [35]and the proposed DTC schemes. The switching frequency and switching losses are computed across various speeds for both classical and proposed Direct Torque Control (DTC) schemes.

The average torque and flux ripples are determined from the recorded steady-state torque and flux patterns sample data for specific speeds and loads, utilizing (5.19). The calculation of average torque and flux ripple for Conventional DTC (C-DTC), PI-CST-DTC, and FOPI-CST-DTC methods is based on a dataset consisting of 10,000 samples per second (N/sec).

$$Torque/flux_{ripple} = \sqrt{\frac{1}{N}\sum_{i=1}^{N}\left(X(i) - X_{avg}\right)^2} \tag{5.19}$$

Where $X(i)$ =torque/flux at the i^{th} sample

X_{avg}=average torque/flux over N samples

In Figure 2.11, torque and flux patterns under no load are illustrated at speeds (I) 1400 rpm and (II) 50 rpm. Notably, I(a) and II(a) for the C-DTC exhibit torque ripples of 0.201 Nm and 0.206 Nm, respectively, at the corresponding speeds. Likewise, the proposed PI-based CST-DTC, in I(b) and II(b), showcases torque ripples of 0.17 Nm and 0.127 Nm, respectively, for speeds of 1400 rpm and 50 rpm. Additionally, the proposed FOPI-based CST-DTC, represented by I(c) and II(c), also achieves a notable reduction in torque ripples of 0.17 Nm

and 0.131 Nm, respectively, with respect to the C-DTC scheme at the corresponding speeds of 1400 rpm and 50 rpm.

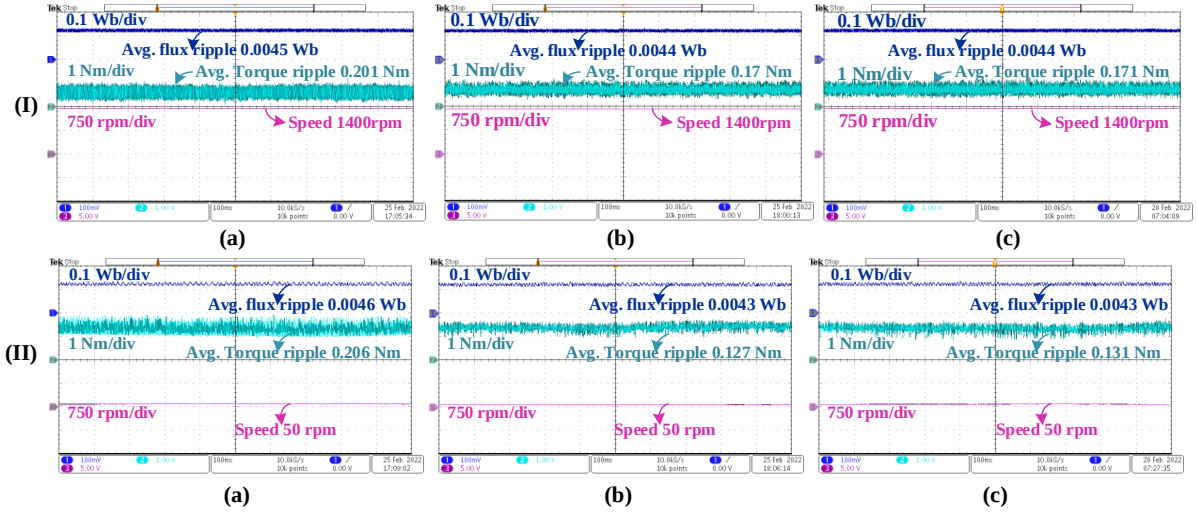

Figure 2.11 Flux and torque responses under a light load of 0.6 Nm for speeds (I) 1400 rpm and (II) 50 rpm in (a) Conventional DTC (C-DTC), (b) PI-CST-DTC, and (c) FOPI-CST-DTC schemes

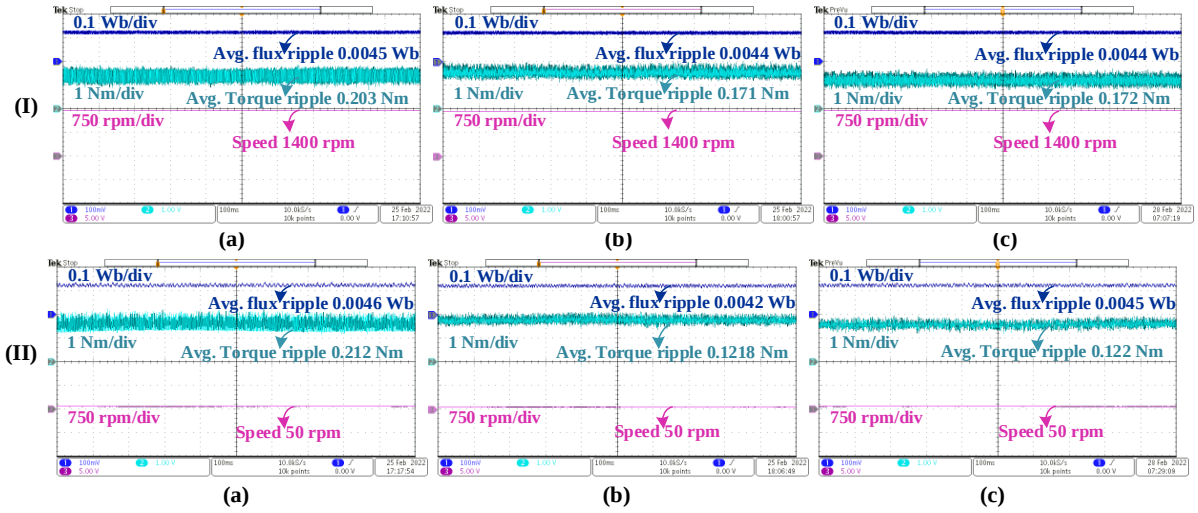

Figure 2.12 Flux and torque responses under a 1.4 Nm load for speeds (I) 1400 rpm and (II) 50 rpm in (a) Conventional DTC (C-DTC), (b) PI-CST-DTC, and (c) FOPI-CST-DTC schemes

Similarly, In Figure 2.12, the torque and flux patterns under a 1.4 Nm load are illustrated at speeds (I) 1400 rpm and (II) 50 rpm. Notably, I(a) and II(a) for C-DTC exhibit torque ripples of 0.203 Nm and 0.212 Nm at speeds of 1400 rpm and 50 rpm, respectively. In the proposed PI-based CST-DTC scheme, shown in I(b) and II(b), reduced torque ripples of 0.171 Nm and 0.122 Nm are observed for the corresponding speeds of 1400 rpm and 50 rpm.

Similarly, the proposed FOPI-based CST-DTC, depicted in I(c) and II(c), also demonstrates reduced torque ripples of 0.172 Nm and 0.122 Nm for speeds of 1400 rpm and 50 rpm. By combining insights from Figure 2.11 and Figure 2.12, it can be concluded that the proposed PI or FOPI-based CST-DTC consistently minimizes torque ripple across all operating speeds and loads, particularly showcasing a substantial reduction under low speeds. Since the same flux hysteresis band is applied to all three methods, the stator flux ripples are almost equivalent for C-DTC, PI-CST-DTC, and FOPI-CST-DTC.

In Figure 2.13, the bar chart illustrates the average torque ripple for different speeds under both light load and loaded conditions. The bar chart indicates that the proposed PI-CST-DTC and FOPI-CST-DTC methods exhibit an appreciable reduction in torque ripple at both high and low speeds, regardless of the load conditions. Notably, these proposed methods demonstrate a significant reduction in torque ripple under low speeds in both light-loaded and loaded cases compared to the C-DTC method, as depicted in Figure 2.13. This reduction is attributed to the precise adjustment of the duty of active voltage vectors relative to rotor speeds in the proposed PI-CST-DTC and FOPI-CST-DTC methods.

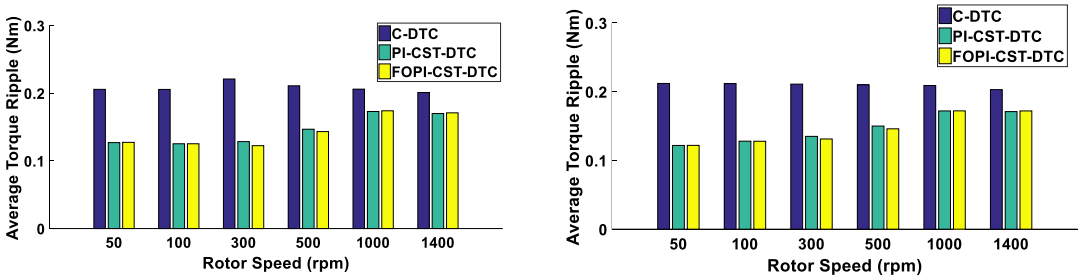

Figure 2.13 Steady-state torque ripple at various speeds under light load (0.6 Nm) and loaded (1.4 Nm) conditions for C-DTC, PI-CST-DTC, and FOPI-CST-DTC.

Figure 2.14 represents the phase current and *%THD* at 1000 rpm with a 1.4 Nm load, showcasing C-DTC with a *%THD* of 20.87%, while the proposed PI-CST-DTC and FOPI-CST-DTC schemes achieve 18.64% and 18.68%, respectively. Similarly, Figure 2.15 exhibits the phase current waveform and *%THD* at 100 rpm, illustrating *%THD* values of 13.4% and 13.7% for the proposed PI-CST-DTC and FOPI-CST-DTC methods, in contrast to C-DTC's *%THD* of 19.38%. Moving to Figure 2.16, the bar chart depicts the current *%THD* for various rotor speeds under both lightly loaded and loaded conditions. Notably, the proposed PI-CST-DTC and FOPI-CST-DTC methods consistently exhibit lower *%THD* values, demonstrating a remarkable reduction in harmonic distortion in current, especially at low operating speeds.

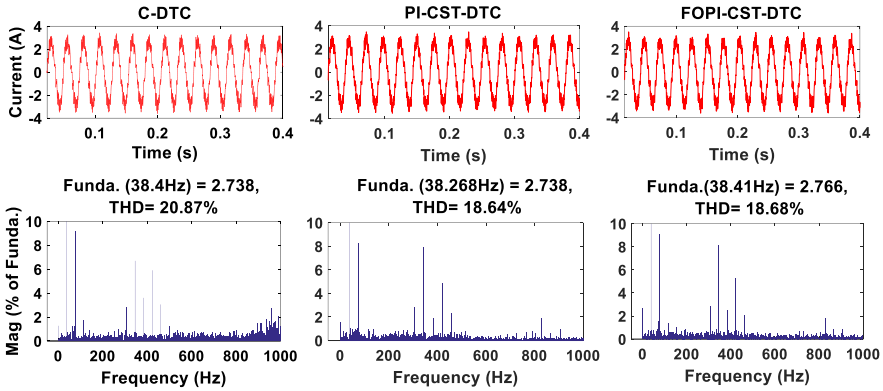

Figure 2.14 Phase current waveform and %THD at 1000 rpm in C-DTC, CST-DTC, and FOPI-based Current Source Torque FOPI-CST-DTC under a loaded condition (1.4 Nm)

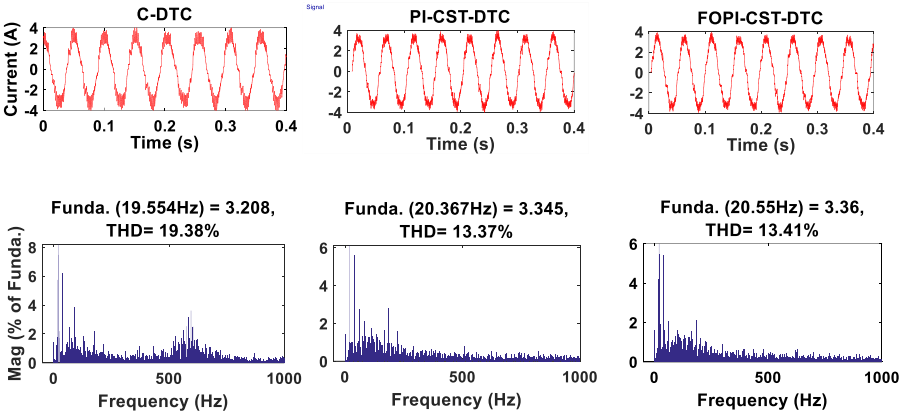

Figure 2.15 Phase current waveform and %THD at 100 rpm in C-DTC, CST-DTC, and FOPI-based Current Source Torque FOPI-CST-DTC under a loaded condition (1.4 Nm)

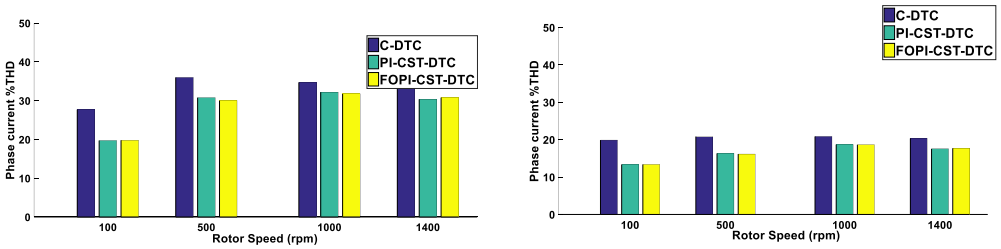

Figure 2.16 Current THDs for different speeds with a light load (0.6Nm) and loaded (1.4 Nm) condition in C-DTC, PI-CST-DTC, and FOPI-CST-DTC

Table 2.2 Steady-State Analysis Of C-DTC [35], PI-CST-DTC, FOPI-CST-DTC Methods

Method	**Average Torque Ripple (Nm)**					**Phase current %THD**			
	1400rpm	**1000rpm**	**500rpm**	**100rpm**	**50rpm**	**1400rpm**	**1000rpm**	**500rpm**	**100rpm**
C-DTC	0.203	0.21	0.21	0.2118	0.212	20.32	20.86	20.83	19.37
PI-CST-DTC	0.171	0.172	0.15	0.128	0.1218	17.54	18.64	16.33	13.37
FOPI-CST-DTC	0.172	0.1721	0.146	0.127	0.122	17.61	18.68	16.15	13.34
% reduction in PI-CST-DTC	**15.7%**	**18%**	**28.5%**	**39.6%**	**42.5%**	**13.6%**	**10.64%**	**21.6%**	**30.9%**
% reduction in FOPI-CST-DTC	**15.35%**	**18%**	**30.4%**	**40%**	**42.45 %**	**13.5%**	**10.4%**	**22.5%**	**31.1%**

The comparison Table 2.2 shows the overall steady-state performance analysis of C-DTC, PI-CST-DTC, and FOPI-CST-DTC methods in terms of average torque ripple and current *%THD* and expressed in percent improvement. From Table 2.2 proposed CST-DTC methods greatly improve low-speed performance.

The proposed PI-CST-DTC and FOPI-CST-DTC schemes maintain a constant switching frequency with minimal variation relative to rotor speeds, as discussed in the earlier sections. Switching frequencies for various speeds are calculated for both C-DTC and the proposed methods using experimental data and illustrated in Figure 2.17. The figure reveals that C-DTC exhibits a significant variation in switching frequency, ranging from 0.5 kHz to 2.45 kHz. In contrast, the proposed PI-CST-DTC and FOPI-CST-DTC methods show minimal variation, fluctuating between 0.8 kHz and 1.4 kHz, and this variation is due to the influence of the flux hysteresis controller.

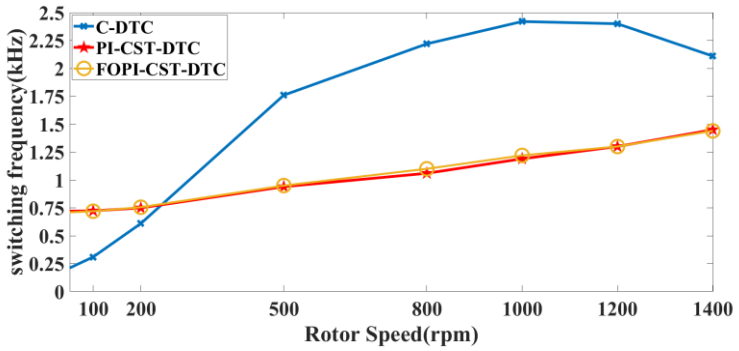

Figure 2.17 Switching frequency variation for varying rotor speed in C-DTC and CST-DTC

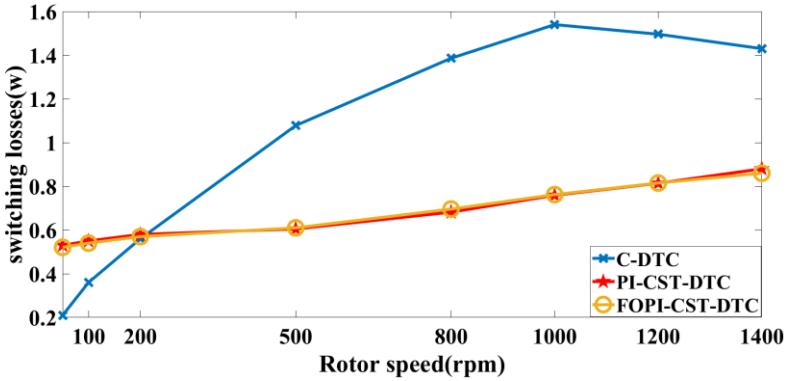

Figure 2.18 Variation of switching turn on/off losses for C-DTC and Proposed CST-DTC methods

Considering that switching power loss is proportional to the switching frequency, the PI-CST-DTC and FOPI-CST-DTC methods exhibit less variation in switching losses. This ensures the proper selection of ratings of switches. Switching losses are calculated for the real-time IGBT switch SKM75GB12T4 using the analytical instantaneous current-based loss calculation

method [67]. Figure 2.18 displays the switching turn ON/OFF losses of the inverter switch, indicating that the proposed PI-CST-DTC and FOPI-CST-DTC methods exhibit minimal switching loss variation, while C-DTC shows a substantial fluctuation in switching losses concerning different rotor speeds.

2.5.2 Dynamic Performance Analysis

The dynamic performance of C-DTC and the proposed PI-CST-DTC and FOPI-CST-DTC schemes were tested by introducing step speed disturbances and step load torque disturbances. The proposed PI-CST-DTC degrades dynamic performance while improving low-speed performance compared to the C-DTC method. These slower dynamics occur due to the frequent selection of zero voltage vectors in the PI-CST controller, as discussed in earlier Section 2.3.1. The robust FOPI controller has been introduced in place of the PI controller in the proposed CST to enhance the slower dynamics of the proposed CST-DTC method. This FOPI controller is designed based on the phase-amplitude margin method [63] as discussed in earlier section 2.3.1.

The dynamic performance of speed is observed by introducing step speed disturbances and step speed reversal disturbances in both classical DTC and the proposed CST-DTC methods. The load dynamic performance is analyzed by introducing sudden load disturbances for both C-DTC and proposed CST-DTC methods, as discussed below.

The step speed dynamics, from 1400 rpm to 1000 rpm and subsequently to 500 rpm, are illustrated in Figure 2.19. The data from Figure 2.19 indicates that the duration taken by C-DTC to transition from 1400 rpm to 1000 rpm and from 1000 rpm to 500 rpm is 1.7 seconds and 1.11 seconds, respectively. Conversely, for PI-CST-DTC, these durations extend to 2.65 seconds and 1.41 seconds, while with FOPI-CST-DTC, the times required are 1.58 seconds and 0.95 seconds, respectively. The comparison depicted in Figure 2.19 highlights that the dynamics of PI-CST-DTC are slower when compared to C-DTC, whereas the FOPI-CST-DTC dynamics closely rival those of the C-DTC method. Additionally, Figure 2.20 showcases the speed reversal response from 500 rpm to -500 rpm for C-DTC, PI-CST-DTC, and FOPI-CST-DTC, with corresponding times of 1.61 seconds, 1.79 seconds, and 1.35 seconds. Consequently, the overall speed dynamics of the proposed PI-CST-DTC are enhanced with the incorporation of the FOPI controller.

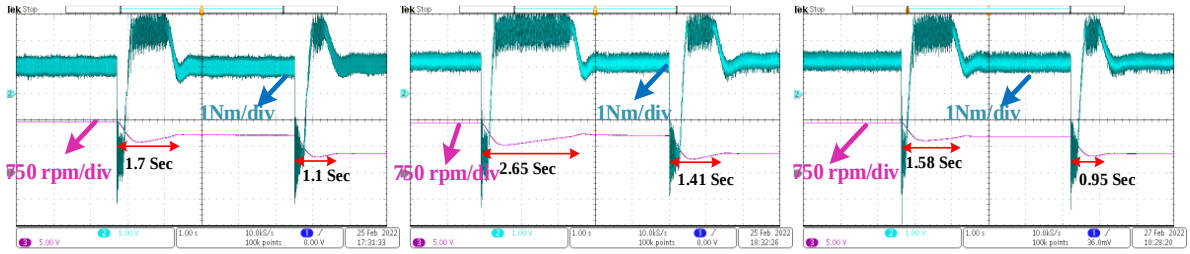

Figure 2.19 Speed dynamics from 1400 rpm to 1000 rpm to 500 rpm under load 1.1 Nm for C-DTC, PI-CST-DTC, FOPI-CST-DTC methods

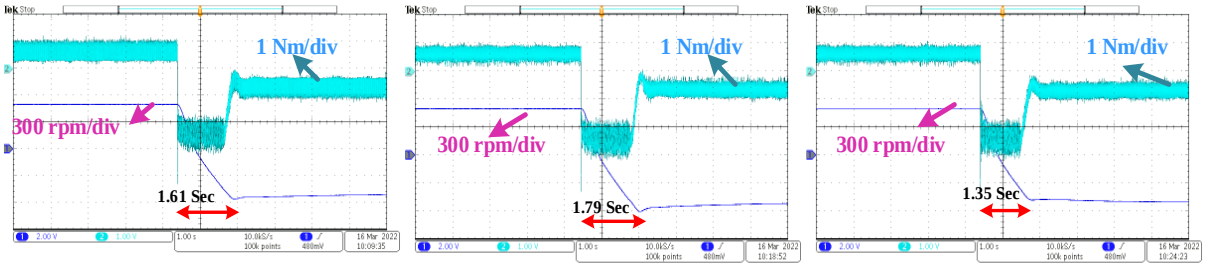

Figure 2.20 Speed reversal response from 500 rpm to -500 rpm for load 0.6Nm for C-DTC, PI-CST-DTC, FOPI-CST-DTC methods

Examining Figure 2.21 shows the load dynamics at a constant speed of 1000 rpm, subjected to various step load disturbances for C-DTC, PI-CST-DTC, and FOPI-CST-DTC methods. Notably, C-DTC achieves the required load torque to settle at speed in 0.45 seconds, 0.48 seconds, and 0.57 seconds. Conversely, in the case of PI-CST-DTC, the times are slightly increased, showing 0.51 seconds, 0.57 seconds, and 0.591 seconds, indicating comparatively slower dynamics. The slower dynamics of the PI-CST-DTC method are effectively improved with the introduction of the FOPI controller, resulting in increased duty of the active vector during load dynamics. The proposed FOPI-CST-DTC method improves, taking only 0.35 seconds, 0.41 seconds, and 0.45 seconds for respective load changes. The enhanced dynamics of the proposed FOPI-CST-DTC scheme compete with the C-DTC scheme.

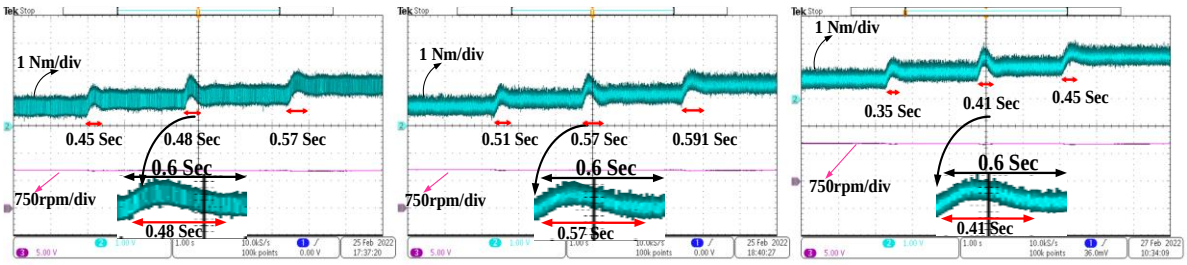

Figure 2.21 Load dynamic response for load 0.6Nm-1Nm-1.4Nm under the motor of 1000 rpm for C-DTC, PI-CST-DTC, FOPI-CST-DTC

Table 2.3 illustrates a comparison of speed dynamics and load dynamics between C-DTC, PI-CST-DTC, and FOPI-CST-DTC. It is evident from the table that the proposed FOPI-CST-DTC exhibits commendable dynamics comparable to those of the C-DTC method. Table 2.4 shows the machine parameters and controller parameters details.

Table 2.3 Dynamic Performance Analysis of C-DTC [35], PI-CST-DTC, FOPI-CST-DTC Methods

Method	**speed step response**		**Speed Reversal response**	**Torque dynamics**	
	1400-1000rpm	1000-500rpm	500rpm to -500rpm	0.6Nm-1Nm	1Nm-1.4Nm
C-DTC	1.7 sec	1.11 sec	1.61 sec	0.45 sec	0.48 sec
PI-CST-DTC	2.64 sec	1.41 sec	1.79 sec	0.51 sec	0.57 sec
FOPI-CST-DTC	1.58 sec	0.95 sec	1.35 sec	0.35 sec	0.41 sec
% improvement in FOPI-CST-DTC w.r.t PI-CST-DTC	**40%**	**32.6%**	**24.6%**	**31.3%**	**28%**

Table 2.4 Parameters of five-phase Induction motor

Five-phase induction motor & controller Parameters					
Parameter	***value***	***Parameter***	***Value***	***Parameter***	***Value***
Power Rating	1 HP	Rotor resistance (Rr)	1.42 Ω	No. of Poles (P)	4
Stator resistance (Rs)	1.05Ω	Rotor inductance (Lr)	90.73Mh	Rated Speed	1440 rpm
Stator inductance (Ls)	90.73mH	Mutual inductance (Lm)	84.73mH	Inertia constant (J)	0.148Kg-m^2
Speed PI controller	Kp=0.02, Ki=0.005	CST PI controller	Kp=86, Ki=18800	CST FOPI controller	Kp=86, Ki=13500, δ=0.35

2.6 Summary and conclusions

In this chapter, the focus is on implementing modified PI-CST-DTC and FOPI-CST-DTC methods on a 2-level inverter-fed FPIM to enhance the torque profile, current profile, and switching frequency variation without compromising the dynamics of the drive. The proposed methods employ the Constant Switching Torque (CST) controller instead of the hysteresis torque controller used in C-DTC, utilizing the same lookup table for fair comparison. These methods exhibit reduced torque ripple, flux ripple, and switching frequency variations compared to the classical hysteresis-based DTC scheme at various speeds under both no-load and loaded conditions. Particularly at low speeds, the steady-state performance is significantly improved for different loading conditions. The use of the constant switching torque (CST) controller minimizes switching frequency variations, almost maintaining a constant value under steady-state conditions, thereby facilitating the proper design of inverter switches. The slower dynamic performance of the proposed PI controller-based CST-DTC is further improved and competes with C-DTC by replacing the PI controller with the FOPI controller, with proper design equations. Hence, the proposed FOPI-CST-DTC scheme is recommended for 5-phase induction motor drives in high-power-density industrial applications where smooth operation and better dynamics are critical constraints.

Chapter 3

An Improved Steady-State Performance of 5-Phase Induction Motor with CSF and CST Controller-based DTC Techniques

Chapter 3

An Improved Steady-State Performance of 5-Phase Induction Motor with CSF and CST Controller-based DTC Techniques

3.1 Introduction

In the previous chapter, the discussion centered on the Modified Constant Switching Torque Controller-based Direct Torque Control (CST-DTC) scheme for a Five-Phase Induction Motor (FPIM) drive. The aim was to enhance the torque profile and current profile without affecting the system dynamics. The CST-DTC scheme employs only 10 active voltage vectors, replacing the hysteresis torque controller with the CST controller. However, it does not alter the hysteresis flux controller, resulting in no improvement in flux ripple. Despite using large voltage vectors of a 5-leg inverter, the harmonic (xy) plane components are only minimized rather than eliminated. To further improve the steady-state performance of the FPIM in terms of torque ripple, flux ripple, and harmonic distortion, both the Constant Switching Torque (CST) and Constant Switching Flux (CSF) controller introduced in in Direct Torque Control (DTC) scheme of 2-level VSI fed 5-phase induction motor in this chapter. This proposed method utilizes 10 virtual voltage vectors, ensuring the elimination of all harmonic plane components. A virtual voltage vector is created by activating two voltage vectors within a single sample period with a suitable duty ratio. This construction ensures that the resultant vector in the harmonic plane is zero, while the resulting voltage vector in the fundamental plane possesses a non-zero value.

In the initial part of this chapter, the focus is on the design and implementation of the Constant Switching Flux (CSF) controller. The CSF controller replaces the hysteresis flux controller without disturbing the hysteresis torque controller of the classical DTC scheme and named as CSFHTC-DTC (constant switching flux controller and hysteresis torque controller-based DTC) of 2-level Voltage Source Inverter (VSI) fed Five-Phase Induction Motor (FPIM). The performance assessment of the proposed CSFHTC-DTC method is done in comparison to the classical Direct Torque Control (C-DTC) method, considering factors such as torque ripple, flux ripple, and current harmonic distortion, along with the dynamic performance of the machine. The proposed CSFHTC-DTC scheme improves the flux profile, and current profile without disturbing the torque profile and mechanical dynamics as it is using the same hysteresis torque controller.

Subsequently, the chapter delves into the discussion of the Constant Switching Torque Controller and Constant Switching Flux Controller-based Direct Torque Control (CSTF-DTC) of a 2-level VSI-fed 5-phase induction motor. The CSTF-DTC scheme replaces both the hysteresis torque and flux controllers of classical DTC with constant switching torque and flux controllers. This combines the advantages associated with CST and CSF controllers. The design and implementation of the CST controller are discussed in the previous chapter (Chapter 2) and the same applies to this proposed CSTF-DTC scheme. The effectiveness of the proposed CSTF-DTC is tested in terms of flux ripple, torque ripple, and current harmonic distortion along with dynamic performance over other existing DTC schemes on a 2-level VSI-fed 5-phase induction motor. The proposed CSTF-DTC further reduces the torque ripple, flux ripple, and current harmonic component w.r.t existing DTC schemes of 5-phase induction motor.

3.2 Design and Implementation of constant switching flux controller

The two-level CSF controller contains a PI controller, triangular carrier wave, and comparator as in Figure 3.1. The flux error is processed with a PI controller which gives control signal Ψ_c. The Ψ_c is compared with the triangular carrier signal and gives output status (Ψ_{stat}) as +1,-1 (+1 means flux needs to increase, -1 means flux needs to decrease) with regular intervals as it follows the triangular carrier as in (3.1). The CSF controller produces the Ψ_{stat} as +1,-1 which resembles the classical hysteresis flux controller of the classical DTC scheme.

$$\Psi_{stat} = +1 \qquad \Psi c \geq C_{\Psi}$$
$$\Psi_{stat} = -1 \qquad \Psi c < C_{\Psi} \tag{3.1}$$

Where Ψ_c = CSF PI controller output

C_{Ψ}=CSF controller triangular carrier wave

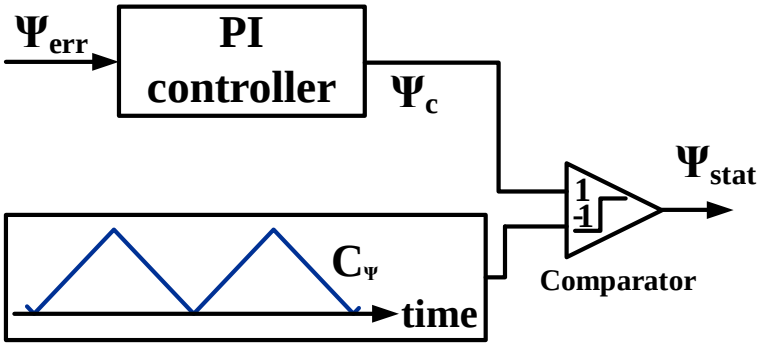

Figure 3.1 2-level constant switching flux controller

The design of a constant switching flux (CSF) controller can be done from the following equations below [68]-[69]

The stator voltage balancing equation of stationary reference can be written as below equation (3.2).

$$V_s = \frac{d\Psi_s}{dt} + i_s R_s \tag{3.2}$$

Where V_s=stator voltage

i_s=stator current

Ψ_s=stator flux linkages

R_s=stator resistance

The slope of stator flux ($\frac{d\Psi_s}{dt}$) can be written from (3.2) by neglecting stator resistance drop ($i_s R_s$) as shown in equation (3.3).

$$\frac{d\Psi_s}{dt} = V_s \tag{3.3}$$

The slope of the stator flux over the sample time T_s is equivalent to the tangential component of the selected space vector in the locus of the stator flux. Referring to Figure 3.2, if the stator flux reference lies in sector 1, then the voltage vectors V_2 and V_5 are chosen to increase or decrease the stator flux (resulting in positive slope and negative slope, respectively). Additionally, the positive flux slope and negative flux slope can be zero and maximum respectively, when the reference voltage vector is at the entrance of the sector. These positive or negative slopes will vary as the reference flux vector moves from the sector entrance. This variation is associated with the reference flux vector angle measured from the sector entrance.

Hence, the positive and negative stator flux slopes for an applied voltage vector over a sector range (0° to 36°) can be expressed as (3.4) and (3.5) respectively. From equations (3.4) and (3.5), the positive/negative torque slopes vary non-linearly w.r.t sin(θ).

$$\frac{d\Psi_s^+}{dt} = \frac{2}{5} V_{dc} \sin\theta \tag{3.4}$$

$$\frac{d\Psi_s^-}{dt} = \frac{2}{5} V_{dc} \sin\left(\theta + \frac{4}{5}\pi\right) \tag{3.5}$$

Where V_{dc}=inverter DC bus voltage

θ=Sector space angle (varies from 0 to π/5)

The average positive or negative slopes over a sector can be determined in terms of triangular frequency and synchronous speed. The total possible number of positive or negative slopes in a sector in terms of triangular carrier frequency and fundamental supply frequency is as follows (3.6)

$$N_f = \frac{2\pi f_{tri}}{10\omega_e} \tag{3.6}$$

Where, N_f =total no. of negative/positive slopes in a sector

f_{tri}=triangular wave frequency (Hz)

ω_e=stator flux synchronous speed (rad/sec)

10=total no. of sectors in flux locus

The average positive or average negative slopes over a sector can be determined from (3.4), (3.5), and (3.6) by assuming a constant slope during a flux state (Ψ_{stat}).

$$\frac{d\Psi_s^-}{dt} = \frac{1}{N_f}\sum_{n=1}^{N_f}\frac{2}{5}v_{dc}\,sin\left(\frac{\pi/5}{N_f}\right)n + \frac{2\pi}{5} = Q_\Psi \tag{3.7}$$

$$\frac{d\Psi_s^+}{dt} = \frac{1}{N_f}\sum_{n=1}^{N_f}\frac{2}{5}v_{dc}\,sin\left(\frac{\pi/5}{N_f}\right)n = P_\Psi \tag{3.8}$$

The resultant average flux slope of stator flux from (3.7) and (3.8) will be written by employing the duty ratio (d_Ψ) (during duty, positive slope occurs, during non-duty negative slope occurs)

$$\frac{d\Psi_s}{dt} = P_\Psi d_\Psi + (1 - d_\Psi)Q_\Psi$$

$$\frac{d\Psi_s}{dt} = (P_\Psi - Q_\Psi)d_\Psi + Q_\Psi \tag{3.9}$$

With the introduction of small perturbations in Ψ_s and d_Ψ the equation (3.9) can be written as in (3.10).

$$\frac{d(\Psi_s + \widehat{\Psi_s})}{dt} = (P_\Psi - Q_\Psi)(d_\Psi + (\widehat{d}_\Psi + Q_\Psi) \tag{3.10}$$

The small signal linear equation is obtained by equating small signal terms in (3.10)

$$\frac{\widehat{d\Psi_s}}{dt} = (P_\Psi - Q_\Psi)\widehat{d}_\Psi \tag{3.11}$$

Applying the Laplace transform on both sides of (3.11) the small signal flux loop transfer function can be obtained as (3.12)

$$\frac{\widehat{\Psi}_s(s)}{\hat{d}_\Psi(s)} = \frac{P_\Psi - Q_\Psi}{S} \tag{3.12}$$

From the obtained flux loop transfer function, the closed flux control diagram with the CSF controller is shown in Figure 3.2.

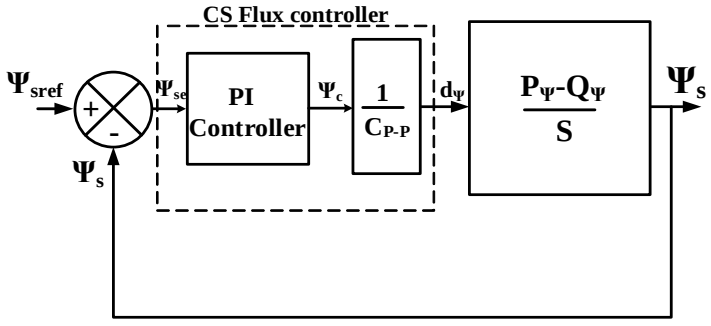

Figure 3.2 Closed loop diagram of flux transfer function with CSF controller

Based on Figure 3.2, it is noted that the flux open-loop transfer function incorporates an integral term with gain. The integral component of the PI controller for the flux loop is deemed unnecessary for achieving zero steady-state error in flux. Hence, the CSF PI controller only includes the proportional gain, denoted as K_{pf}.

The optimal value of K_{pf} for the PI controller is designed with the below-mentioned constraints for the optimal operation of the constant switching flux controller.

- The PI controller's output absolute slope must not be greater than the triangular carrier wave slope. From equations (3.4), and (3.5), the maximum positive and negative stator flux slopes occur at angles of $\pi/5$ and 0 respectively over a sector. Then

$$The\ slope\ of\ triangular \geq \frac{2}{5} v_{dc}\ sin\frac{\pi}{5} K_{pf} \tag{3.13}$$

  The triangular carrier frequency is chosen as 2500Hz with a peak-peak magnitude ($C_{P\text{-}P}$) of 70 hence the triangular carrier wave slope is 350000 sec^{-1} and the DC link voltage is 150V. Then the proportional gain K_{pf} can be obtained from (3.13) as $K_{pf} \leq 9924$.

- The bandwidth of the closed stator flux loop transfer function (shown in Figure 3.2) must not exceed half of the frequency of the triangular carrier wave

$$\frac{1}{2} f_{tri} \geq BW(closed\ loop\ flux\ transfer\ function) \tag{3.14}$$

The maximum positive and negative slopes for a DC voltage of 150V can be obtained from (3.7) and (3.8) as 22.56, and -22.56 respectively.

From the second constraint, the K_{pf} is calculated by assuming the bandwidth of the closed loop transfer function should not be greater than half the triangular carrier wave frequency i.e. 1250Hz. The bandwidth of the closed-loop flux transfer function from Figure 3.2 can be expressed by substituting the known values

$$\left|\frac{0.52K_{pf}}{s+0.52K_{pf}}\right|_{s=BW} = -3dB \tag{3.15}$$

Where, BW=Band width frequency in Rad/sec

The critical value of the proportional gain K_{pf} of the CSF PI controller can be obtained by taking the bandwidth of the closed-loop flux control system as $BW=s=2\pi(1250)$ rad/sec and the value of K_{pf} is ≤ 12271.

- Hence, the optimum value of K_{pf} can be selected by satisfying the above-mentioned two constraints i.e. the optimum value of $K_{pf} \leq 9924$.

3.3 Implementation of the proposed CSFHTC-DTC scheme

The CSFHTC-DTC scheme, presented in this work, incorporates a 2-level constant

switching flux (CSF) controller and 3-level hysteresis torque controllers (HTC) in a voltage source inverter-controlled five-phase induction motor. The primary objective of this scheme is to improve the flux profile and current profile without compromising the faster dynamics inherent in the classical hysteresis-based DTC (C-DTC) method that shares the same lookup table. Importantly, the proposed CSFHTC scheme modifies only the flux controller, ensuring that it does not impact torque profiles and dynamic behavior. The main focus of the proposed method is the reduction of average flux ripple and current harmonic distortion under varying rotor speeds and loads while preserving torque profiles and machine dynamics. The implementation utilizes 10 virtual voltage vectors and is compared against the classical DTC scheme to assess the effectiveness of the CSF controller.

3.3.1 Generation of Virtual Voltage Vectors

The 2-level 5-leg inverter generates 32 space voltage vectors and is grouped as large ($0.6472V_{dc}$), medium ($0.4V_{dc}$), small ($0.2472V_{dc}$), and null ($0V_{dc}$) vectors as discussed in Chapter 1.2 and these vectors are located in both the fundamental (αβ) and harmonic (xy) planes as seen in Figure 3.3.

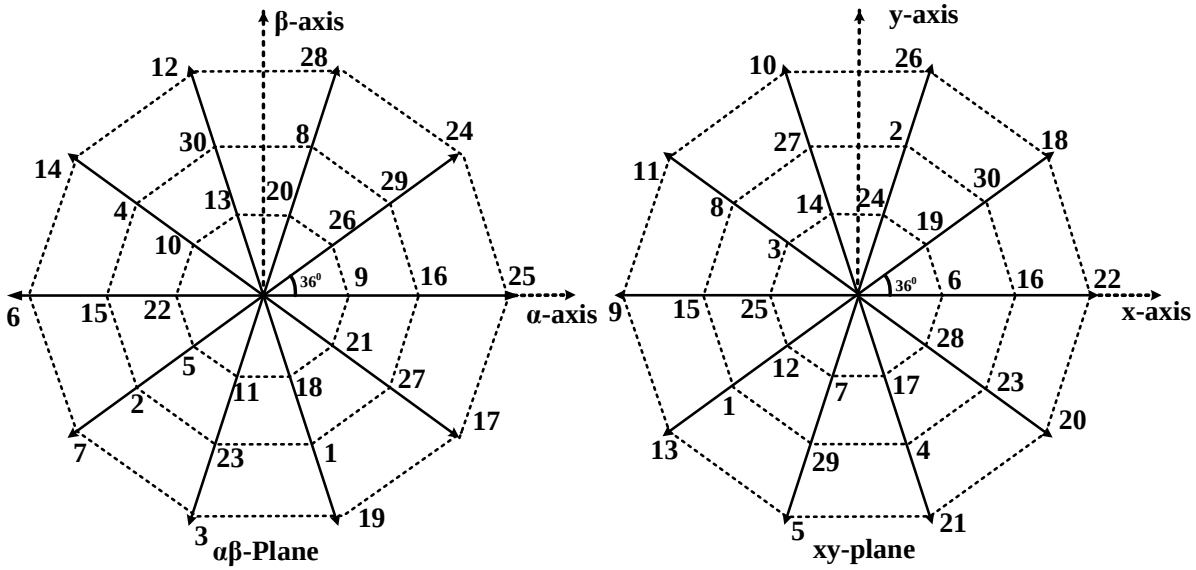

Figure 3.3 Space voltage vector location diagram in the both fundamental (αβ)-plane and harmonic (xy)-plane

In Figure 3.3, it is evident that the presence of large vectors in the fundamental plane appears as small vectors in the harmonic plane with an inverse direction, and conversely, medium vectors in the fundamental plane appear as medium vectors in the harmonic plane [35]. The essential function of the fundamental plane components lies in the generation of electromagnetic torque, while the harmonic plane components contribute to ohmic losses

within the distributed winding machine [36].

Therefore, the elimination of harmonic plane (xy) components is crucial to prevent excessive power loss caused by low-frequency harmonic plane currents. This elimination is achieved through the volt-second balancing technique, as explained in [35]. Given that the amplitude ratio of the medium vector (vector 16) to the small vector (vector 25) is 1/0.6181 in the xy plane, the dwell time ratio of the medium vector and small vector states can be set at 0.6181. This setting creates a zero-mean volt-second vector in the xy-plane, effectively eliminating low-frequency harmonic currents, as depicted in Figure 3.4(b). The resulting virtual voltage (VV) vector V_1 (25,16) in the fundamental (αβ) plane is then calculated using equation (3.16) and illustrated in Figure 3.4(a).

The VVV generation in the αβ plane from large and medium vectors can be generated.

$$VV_{\alpha\beta} = \frac{t_1}{T_s}V_L + \frac{t_2}{T_s}V_M = 0.553V_{dc}\angle\delta \qquad (3.16)$$

Where $VV_{\alpha\beta}$=virtual voltage vector in $\alpha\beta$ plane

V_M=medium voltage vector=$0.4V_{dc}\angle\delta$

V_L=Large vector=$0.642V_{dc}\angle\delta$

δ=angle=$2\pi n\ /\ 10$ (n=0….9)

t_1 =Dwell time of large vector=$0.618T_s$

t_2 =Dwell time medium vector=$0.382T_s$

T_s=control algorithm sample period

As the large voltage vector in the fundamental(αβ) plane will become the small voltage vector with the opposite direction in the harmonic (xy) plane, the resultant virtual voltage vector in the harmonic (xy) plane will become zero as in (3.17)

$$VV_{xy} = \frac{t_1}{T_s}V_S + \frac{t_2}{T_s}V_M = 0V_{dc}\angle\delta \qquad (3.17)$$

Where VV_{xy}=virtual voltage vector in xy plane

V_M=medium voltage vector=$0.4V_{dc}\angle\delta$

V_S=Small vector=$-0.2472V_{dc}\angle\delta$

δ=angle=$2\pi n/10$ (n=0….9)

t_1 =Dwell time of large vector=$0.618T_s$

t_2 =Dwell time medium vector=$0.382T_s$

T_s=control algorithm sample period

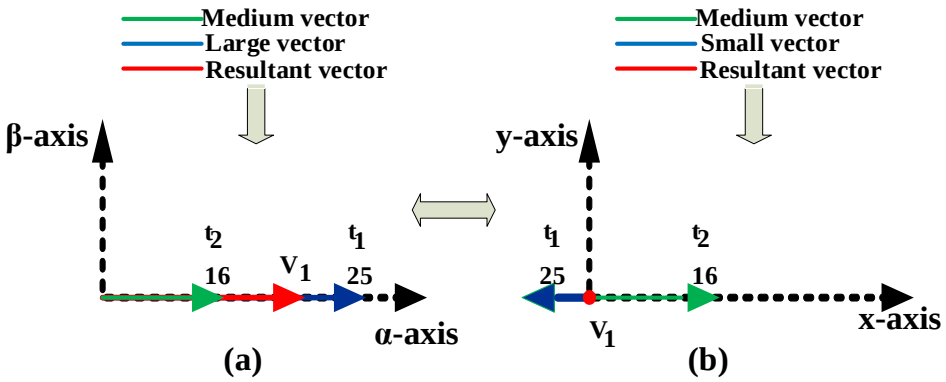

Figure 3.4 Virtual voltage vector V_1 generation from vector 25 and 16 in both the(a) αβ and(b) xy plane

The selected inverter switching states with the calculated dwell times (t_1, t_2) form 10 virtual voltage vectors V_1 to V_{10} with a magnitude of $0.553V_{dc}$ in the fundamental plane as shown in Figure 3.5. These ten active virtual voltage vectors, as well as the two null voltage vectors V_0 and V_{31}, are used to form a lookup table for the classical DTC method and proposed CSFHTC-DTC method.

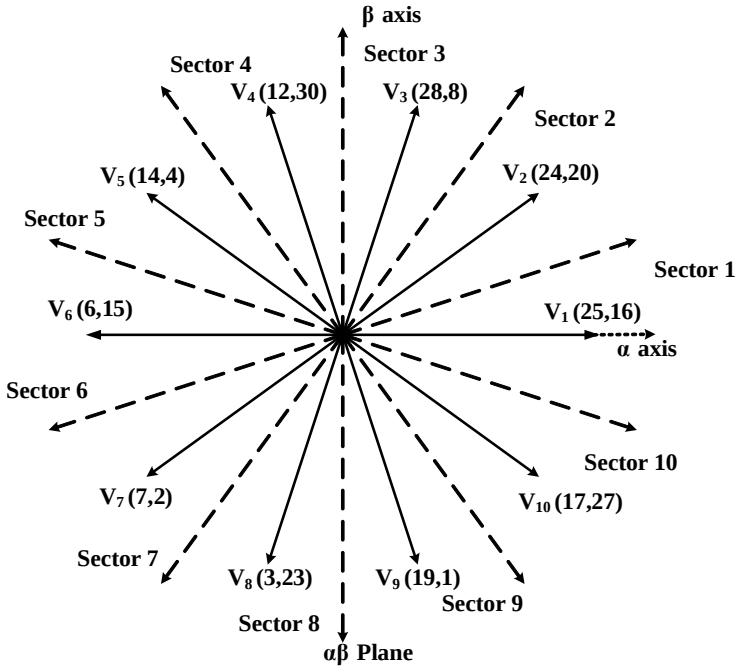

Figure 3.5 Space vector diagram of virtual voltage vectors in αβ plane

3.3.2 Operation of proposed CSFHTC-DTC method on FPIM

Figure 3.6 illustrates the block diagram of the proposed CSFHTC-DTC scheme for a 2-level VSI-fed FPIM. The control scheme comprises a speed PI controller, speed sensor, hysteresis torque controller, CSF controller, torque-flux estimation block, and a switching

table. The speed PI controller processes the speed error and generates the reference torque (T_e*). The estimated stator flux (Ψ_s) and electromagnetic torque (T_e) are compared with the reference torque (T_e*) and reference flux (Ψ_s^*) respectively. These errors are then processed by the hysteresis torque controller and CSF controller, leading to the selection of an appropriate switching state from the lookup table (Table 3.1) based on the information on torque status (T_{stat}), stator flux status (Ψ_{stat}), and sector number.

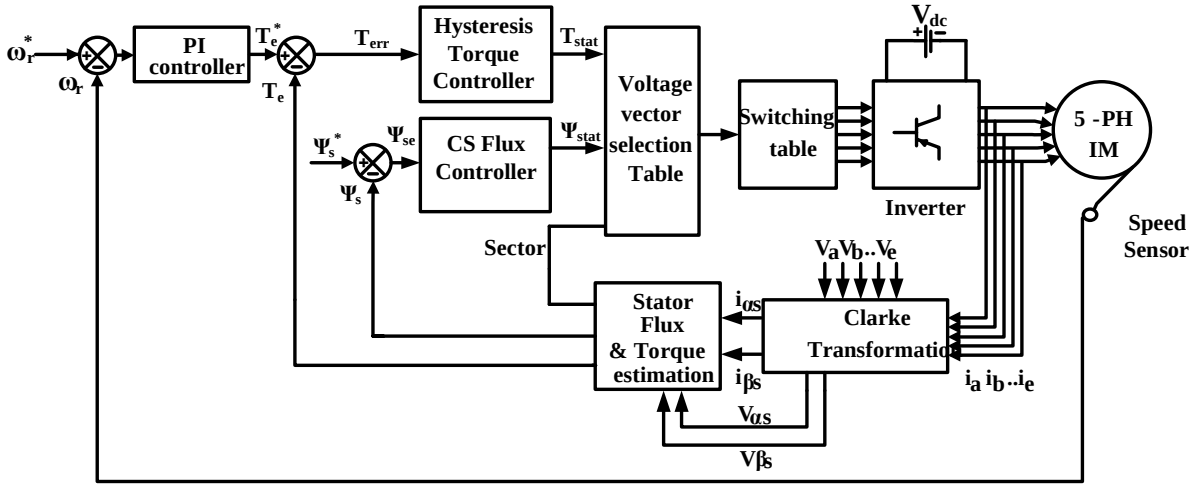

Figure 3.6 Implementation of the proposed CSFHTC-DTC control scheme of a five-phase induction motor

The selected switching vector for the control period T_s influences the stator flux and torque, as expressed in equations (3.18) and (3.19).

$$\Delta \Psi_s = (V_s - R_s i_s) T_s \tag{3.18}$$

$$\Delta T_e = \frac{5}{2}\frac{P}{2}\frac{L_m}{L_r L_{ss}}(|\Psi_s + \Delta \Psi_s|)(|\Psi_r|)\, sin(\Delta\theta) \tag{3.19}$$

Where $\Delta \Psi_s$=change in stator flux due to applied voltage in T_s

$\Delta\theta$=change in torque angle due to applied voltage in T_s

ΔT_e=change in torque due to applied voltage in T_s

The electromagnetic torque (T_e) and stator flux (Ψ_s) are estimated from the voltage and current information.

The stator voltage balancing equation in phase manner is written as (3.20)

$$V_s = I_s R_s + \frac{d\Psi_s}{dt} \tag{3.20}$$

Where V_s = stator phase voltage in volts

I_s= stator phase current in amperes

R_s=stator per phase resistance in ohms

The estimated stator flux (Ψ_s) from (3.20) can be written as below

$$\Psi_s = \int (V_s - I_s R_s)\, dt \tag{3.21}$$

The electromagnetic torque (T_e) estimation can be done as

$$T_e = \frac{5}{2}\frac{P}{2} imag(\Psi_s I_s) \tag{3.22}$$

Where P- no. of stator poles of five-phase induction motor

The same hysteresis torque controller for both C-DTC [35] and proposed CSFHTC-DTC is considered with a torque band of 10% of rated torque, whereas the flux hysteresis band of 5% is selected for the C-DTC method. The five-phase machine parameters and control algorithm parameters are tabulated in Table 3.4.

Table 3.1 Vector selection table for C-DTC [35] & CSFHTC-DTC methods

Ψ_{stat}	T_{stat}	Sector									
		1	2	3	4	5	6	7	8	9	10
1	1	V_2	V_3	V_4	V_5	V_6	V_7	V_8	V_9	V_{10}	V_1
1	0	V_0	V_{31}	V_0	V_{31}	V_0	V_{31}	V_0	V_{31}	V_0	V_{31}
1	-1	V_{10}	V_1	V_2	V_3	V_4	V_5	V_6	V_7	V_8	V_9
-1	1	V_5	V_6	V_7	V_8	V_9	V_{10}	V_1	V_2	V_3	V_4
-1	0	V_{31}	V_0	V_{31}	V_0	V_{31}	V_0	V_{31}	V_0	V_{31}	V_0
-1	-1	V_7	V_8	V_9	V_{10}	V_1	V_2	V_3	V_4	V_5	V_6

Note: (V_1-V_{10})-virtual voltage vectors with a magnitude of $0.553V_{dc}$

3.4 Implementation of the proposed CSTF-DTC scheme on VSI-fed FPIM

As the proposed CSFHTC-DTC uses the same hysteresis torque controller it won't improve torque profile in terms of torque ripple. To further improve the torque profile along with flux ripple reduction and current harmonic reduction, the constant switching torque (CST) controller and constant switching flux (CSF) controller-based DTC (CSTF-DTC) is implemented on 2-level VSI fed FPIM. The proposed CSTF-DTC replaces both hysteresis-based torque and flux controllers with CST and CSF controllers. The proposed technique mainly concentrates on reducing flux ripple, torque ripple, and phase current harmonic distortion under different possible rotor speeds with various loads without altering the dynamics.

The design procedure and implementation of the CST controller have been thoroughly explained in the previous chapter (Chapter 2.3), and the same procedure applies to designing the CST controller in the proposed CSTF-DTC scheme. Similarly, the design procedure and implementation of the constant switching flux (CSF) controller are explained in the previous section (Chapter 3, Section 3.2), and the same flux controller is used for the proposed CSTF-

DTC method.

3.4.1 Operation of the proposed CSTF-DTC scheme

The virtual voltage vectors are derived from large and medium voltage vectors such that it ensures the harmonic plane (xy) components become zero, as explained in Section 3.3.1. The proposed CSTF-DTC control method utilizes 10 active virtual voltage vectors (V_1-V_{10}) along with two null voltage vectors, V_0 and V_{31} (Figure 3.7) to form a lookup table. The space locus is divided into 20 sectors, leading to the construction of a lookup table (Table 3.2). This table facilitates the selection of the nearest virtual voltage vector to meet the required flux and torque demands of the 5-phase induction motor.

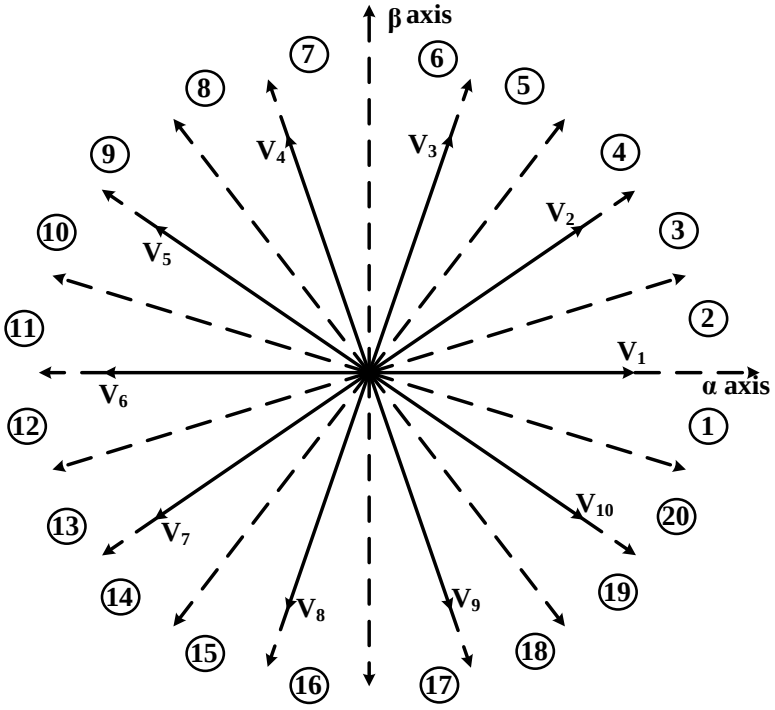

Figure 3.7 Virtual voltage vectors V_1-V_{10} space diagram in αβ-plane

The block diagram representation of the proposed CSTF-DTC method is shown in Figure 3.8 which replaces the hysteresis-based torque and flux controller with CST and CSF controller of a VSI-controlled 5-phase induction motor. Figure 3.8 contains a speed PI controller, speed sensor, flux and torque estimation block, CSF controller, CST controller, vector selection table, a 5-leg VSI, and FPIM. The flux and electro-magnetic torque are estimated based on machine equations (3.21), and (3.22). The mechanical speed error is treated in the speed PI controller and produces the reference electromagnetic torque (T_e^*). The flux and torque error are processed through triangular-based-constant switching torque and flux controllers and give torque statuses (T_{stat}) and flux statuses (Ψ_{stat}). Suitable voltage vectors are

selected from the lookup Table (Table 3.2) based on information on stator flux status (Ψ_{stat}), torque status (T_{stat}), and stator flux sector information.

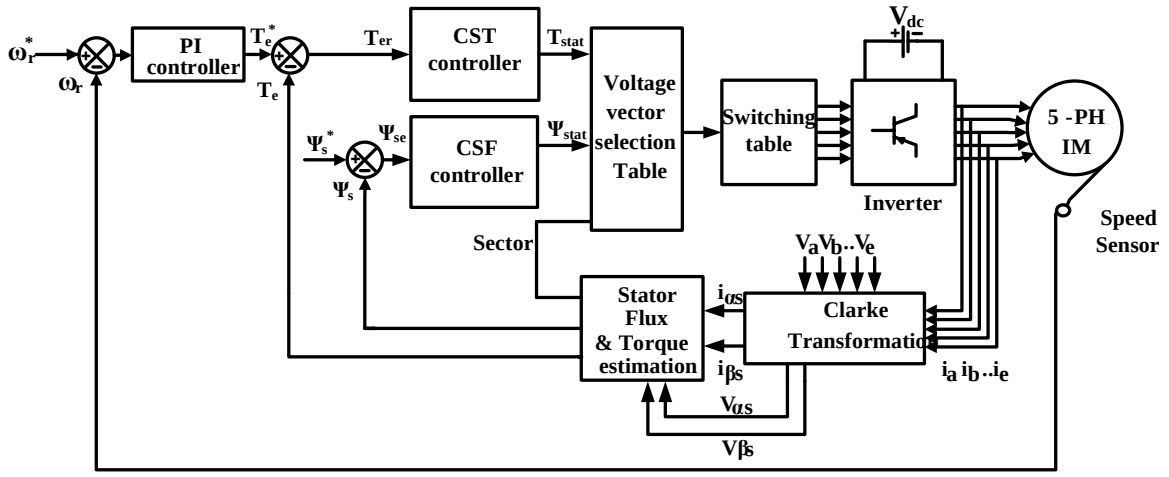

Figure 3.8 The block diagram representation of the proposed CSTF-DTC control scheme of VSI-controlled FPIM

The operation and design implementation of the CST controller and CSF controller are explained in previous sections (section 2.3 and section 3.2). The CST controller and CSF controller output statuses (T_{stat} and Ψ_{stat}) are given as +1, 0, -1, and +1, -1 respectively as indicated in (3.23), (3.24), and shown in Figure 3.9.

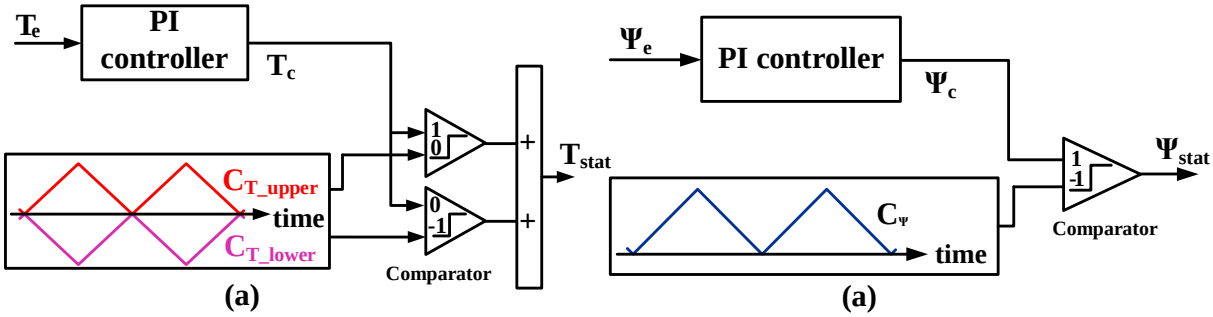

Figure 3.9 (a) 3-level CST controller (b) 2-level CSF controller

For the CST controller,

$$\begin{aligned} T_{stat} &= +1 \quad T_c \geq C_{T\_upper} \\ T_{stat} &= 0 \quad C_{T\_lower} < T_c < C_{T\_upper} \\ T_{stat} &= -1 \quad T_c \leq C_{T\_lower} \end{aligned} \tag{3.23}$$

Where T_c= CST PI controller output

C_{T_upper}=upper triangular carrier wave

C_{T_lower}=lower triangular carrier wave

For the CSF controller,

$$\Psi_{stat} = +1 \qquad \Psi c \geq C_{\Psi}$$
$$\Psi_{stat} = -1 \qquad \Psi c < C_{\Psi} \tag{3.24}$$

Where Ψ_c = CSF PI controller output

C_{Ψ}=CSF controller triangular carrier wave

Table 3.2 Voltage vector table for proposed CSTF-DTC and M-DTC [38] schemes

Ψ_{stat}	T_{stat}	Sector																			
		1	2	3	4	5	6	7	8	9	10	11	12	13	14	15	16	17	18	19	20
1	1	V_2	V_3	V_3	V_4	V_4	V_5	V_5	V_6	V_6	V_7	V_7	V_8	V_8	V_9	V_9	V_{10}	V_{10}	V_1	V_1	V_2
1	0	V_0	V_0	V_{31}	V_{31}	V_0	V_0	V_{31}	V_{31}	V_0	V_0	V_0	V_{31}	V_{31}	V_0	V_0	V_{31}	V_{31}	V_0	V_0	V_{31}
1	-1	V_9	V_{10}	V_{10}	V_1	V_1	V_2	V_2	V_3	V_3	V_4	V_4	V_5	V_5	V_6	V_6	V_7	V_7	V_8	V_8	V_9
-1	1	V_4	V_4	V_5	V_5	V_6	V_6	V_7	V_7	V_8	V_8	V_9	V_9	V_{10}	V_{10}	V_1	V_1	V_2	V_2	V_3	V_3
-1	0	V_{31}	V_0	V_{31}	V_0	V_{31}	V_0	V_{31}	V_0	V_{31}	V_0	V_7	V_7	V_7	V_7	V_7	V_7	V_7	V_7	V_7	V_7
-1	-1	V_7	V_8	V_8	V_9	V_9	V_{10}	V_{10}	V_1	V_1	V_2	V_2	V_3	V_3	V_4	V_4	V_5	V_5	V_6	V_6	V_7

Note: (V_1-V_{10})-virtual voltage vectors with a magnitude of $0.553V_{dc}$

3.4.2 Design of CST controller and CSF controller

The design of the CST controller and CSF controller is discussed for the proposed CSTF-DTC controller from the derived equation in previous sections.

For the design of proportional gain K_{pt} of CST PI controller, the torque slope equations derived in equations (2.2) - (2.12) are used.

The final expression for positive and negative torque slope equation from (2.7) and (2.8) can be rewritten as

$$\frac{dTe^+}{dt} = -A_t T_e + B_t v_s + K_t\left(\frac{\omega_e}{d} - \omega_r\right) \tag{3.25}$$
$$\frac{dTe^-}{dt} = -A_t T_e + K_t \omega_r \tag{3.26}$$

Where $A_t = \frac{1}{\sigma\tau_s} + \frac{1}{\sigma\tau_r}$, $B_t = \frac{5}{2}\frac{P}{2}\frac{L_m}{\sigma L_s L_r}\ \Psi_r$, $K_t = \frac{5}{2}\frac{P}{2}\frac{L_m}{\sigma L_s L_r}\ \Psi_s \Psi_r$

The linearized open torque loop transfer function can be rewritten from (2.12) and shown in Figure 3.10 along the CST controller.

$$\frac{\hat{T}}{\hat{d}} = \frac{B_t v_s}{s + A_t} \tag{3.27}$$

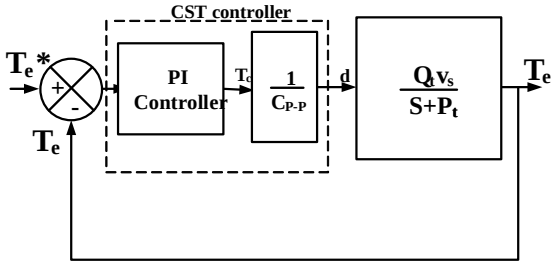

Figure 3.10 Closed-loop torque control equipped with CST controller

For the design of K_{pt}, the slope of the torque should not be more than the absolute slope of the triangular signal. Hence, from the positive torque slope (3.25), and negative torque slope (3.26), it can be written as follows

$$|Slope\ of\ triangular\ carrier| \geq \left\{ \left| -P_t T_e + Q_t v_s + R_t \left(\frac{\omega_e}{d} - \omega_r \right) \right| \right\} * K_{pt} \quad (3.28)$$

$$|Slope\ of\ triangular\ carrier\ | \geq \{ | -P_t T_e - R_t \omega_r | \} * K_{pt} \quad (3.29)$$

The triangular carriers with a frequency of 2500Hz are created in MATLAB/Simulink software with a discrete step interval of 100 μsec. The total number of discrete intervals over a triangular period can be obtained as 4. The slope of the triangular carrier will become 5,00,000 units/sec with a triangular frequency of 2,500Hz and magnitude of 100 units peak-peak.

The maximum positive slope that limits the proportional gain (K_{pt}) occurs at the rated slip speed and zero rotor speed, as seen in (3.28). Similarly, the maximum negative torque slope that limits the proportional gain (K_{pt}) happens at the rated rotor speed, as seen in (3.29). The 5-leg VSI DC link voltage is set to 150V to achieve the rated mechanical speed under full load. Utilizing the parameters of the 5-phase induction motor listed in Table 3.4, the proportional gain (K_{pt}) is calculated from (3.28) as ($K_{pt} \leq 112.53$). Similarly, the proportional gain (K_{pt}) is determined from the negative slope constraint (3.29) as ($K_{pt} \leq 397.2$). Considering the above two constrained values, the optimal value for (K_{pt}) is chosen as ($K_{pt} \leq 112.53$).

The integral controller gain K_i has been selected such that the zero of the PI controller transfer function is the same as the pole in the averaged torque loop function in Figure 3.10 and shown in (3.30)

$$s + \frac{K_{it}}{K_{Pt}} = s + A_t$$

$$K_{it} = A_t K_{pt} \quad (3.30)$$

If the zero of the PI controllers is chosen to be the same as the pole of the open-loop torque transfer function, the value of K_{it} is obtained and is K_{it}<23970

The design of the Constant Switching Flux (CSF) controller for the proposed Constant Switching Torque and Flux Direct Torque Control (CSTF-DTC) scheme has been detailed in the previous section (3.2), and the same controller parameters are employed for the implementation of the proposed CSTF-DTC scheme.

3.5 Experimental results analysis

The proposed Constant Switching Flux and Hysteresis Torque Controller-based Direct Torque Control (CSFHTC-DTC) and Constant Switching Torque and Flux controller-based Direct Torque Control (CSTF-DTC) schemes for the 2-level 5-leg inverter-fed 5-phase

induction motor drive have been experimentally tested and compared with existing Direct Torque Control (DTC) schemes. Initially, the CSFHTC-DTC scheme was implemented on a 2-level inverter-fed 5-phase induction motor, and a comparison was made with the classical DTC scheme [35] to assess the impact of the Constant Switching Flux (CSF) controller on flux ripple, torque ripple, and current harmonic distortion. Subsequently, the CSTF-DTC scheme, incorporating both the CSF controller and Constant Switching Torque (CST) controller, was implemented, and the effectiveness of the proposed scheme was evaluated in comparison with existing DTC control schemes [35], [38], and [70] through rigorous analysis of valid experimental results. The hardware experimental setup is shown in Appendix I. In the experimental work, the proposed CSFHTC-DTC scheme, proposed CSTF-DTC scheme, and other existing DTC schemes are implemented on the dSPACE 1202 controller using real-time interfacing with MATLAB/Simulink software. The motor drive being used for the experimentation test comprises of 1 HP 5-phase induction motor coupled with a 1HP DC generator. The hardware prototype comprises a 5-leg inverter power module with SEMIKRON IGBT switches with an inbuilt gate driver circuit and rectifier unit for DC voltage. The inverter switches are triggered by the gate signal from the dSPACE controller. The 1024 PPR incremental speed encoder is used for accurate speed measurement. The LA 25-P current sensors and LV 25-P voltage sensor are used to sense the phase currents and DC link voltage respectively. The proposed CSFHTC-DTC, CSTF-DTC, and existing DTC control schemes are executed at the same sampling time of 100e-6 sec. The torque hysteresis controller torque band is chosen as 10% rated torque and the flux hysteresis flux band is chosen as 5% of reference flux in existing DTC control schemes [35], [38], and [70]. The five-phase machine parameters and controller parameters are tabulated in Table 3.4.

The steady-state performance of the 5-phase induction motor under various Direct Torque Control (DTC) schemes is assessed by examining torque ripple, flux ripple, and current harmonic distortion. The evaluation involves calculating the average torque ripple and average flux ripple using equation (3.31), utilizing real-time data obtained from steady-state hardware results. The calculation is performed for 10,000 samples per second (N/sec). This analysis allows for a comprehensive comparison of the average torque and flux ripple among the different DTC schemes, providing insights into their performance characteristics under steady-state conditions.

$$Torque/flux_{ripple} = \sqrt{\frac{1}{N}\sum_{i=1}^{N}\left(X(i) - X_{avg}\right)^2} \tag{3.31}$$

Where $X(i)$ =torque/flux at the i^{th} sample

X_{avg}=average torque/flux over N samples

3.5.1 Experimental result analysis of the CSFHTC-DTC method

The effectiveness of the proposed CSFHTC-DTC is assessed under various speeds, both under no-load and loaded conditions, to know the impact of the Constant Switching Flux (CSF) controller. A comparative analysis is conducted with the classical Direct Torque Control (C-DTC) [35] scheme for a fair evaluation by replacing its flux hysteresis controller with a CSF controller. In Figure 3.11, torque and flux patterns are presented for (I) C-DTC and (II) proposed CSFHTC-DTC at speeds of (a) 1400 rpm, (b) 500 rpm, and (c) 100 rpm under no-load conditions. C-DTC exhibits flux ripple of 0.008 Wb, 0.009 Wb, 0.0092 Wb, and torque ripple of 0.156 Nm, 0.146 Nm, 0.14 Nm for the corresponding speeds. Conversely, the proposed CSFHTC-DTC scheme shows reduced flux ripple (0.0056 Wb, 0.006 Wb, 0.0056 Wb) and comparable torque ripple (0.157 Nm, 0.147 Nm, 0.138 Nm) for the corresponding speeds.

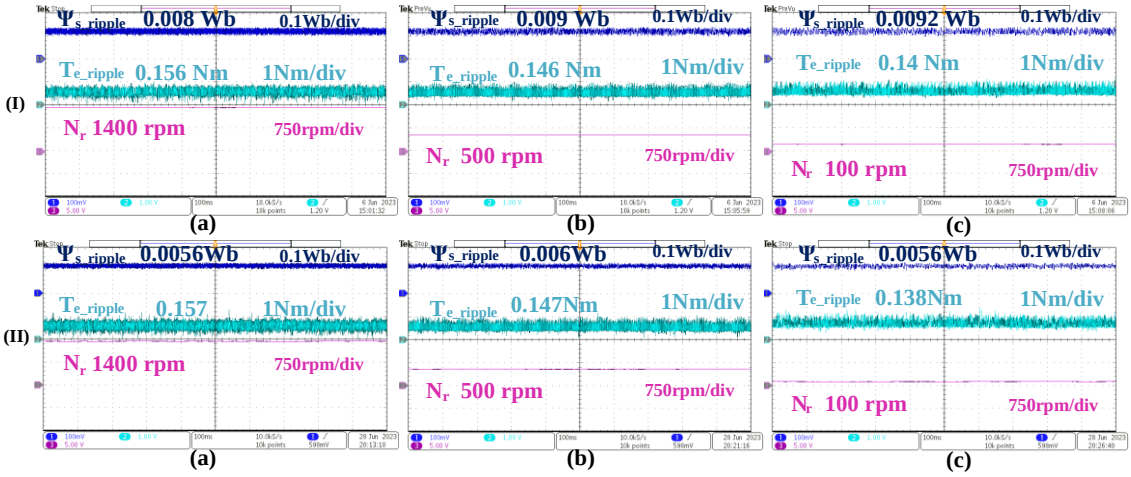

Figure 3.11 Torque flux pattern at (I) C-DTC (II) proposed CSFHTC-DTC method under at (a)1400 rpm, (b) 500rpm, (c)100 rpm under no load

Similarly, Figure 3.12 illustrates the flux and torque patterns for (I) C-DTC [35] and (II) CSFHTC-DTC at (a) 1400 rpm, (b) 500 rpm, and (c) 100 rpm under loaded conditions. From Figure 3.12, it is observed that C-DTC produces flux ripple of 0.0079 Wb, 0.0084 Wb, 0.0085 Wb, and torque ripple of 0.165 Nm, 0.146 Nm, 0.15 Nm, respectively, for the corresponding speeds. In comparison, the proposed CSFHTC-DTC exhibits flux ripple of 0.0056 Wb, 0.0057 Wb, 0.0063 Wb, and torque ripple of 0.161 Nm, 0.145 Nm, and 0.15 Nm, respectively, for the corresponding speeds. Based on the analysis of Figures 3.11 and 3.12, it is concluded that the CSF controller in the proposed CSFHTC-DTC scheme improves the flux

profile without significantly disturbing the torque profile, as the CSFHTC-DTC employs the same hysteresis torque controller.

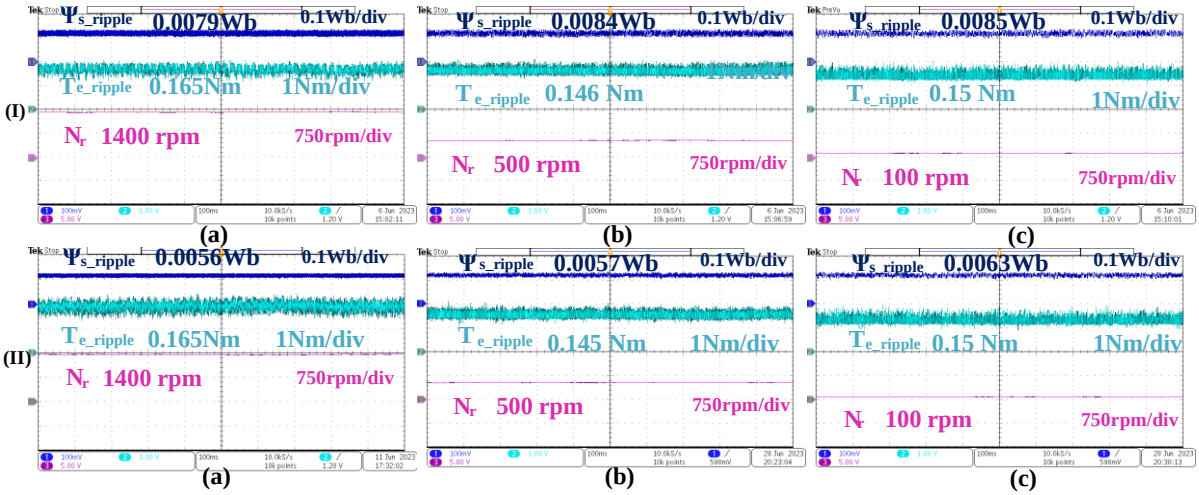

Figure 3.12 Torque flux pattern at (I) C-DTC (II) proposed CSFHTC-DTC method under at (a)1400 rpm, (b) 500rpm, (c)100 rpm under load case

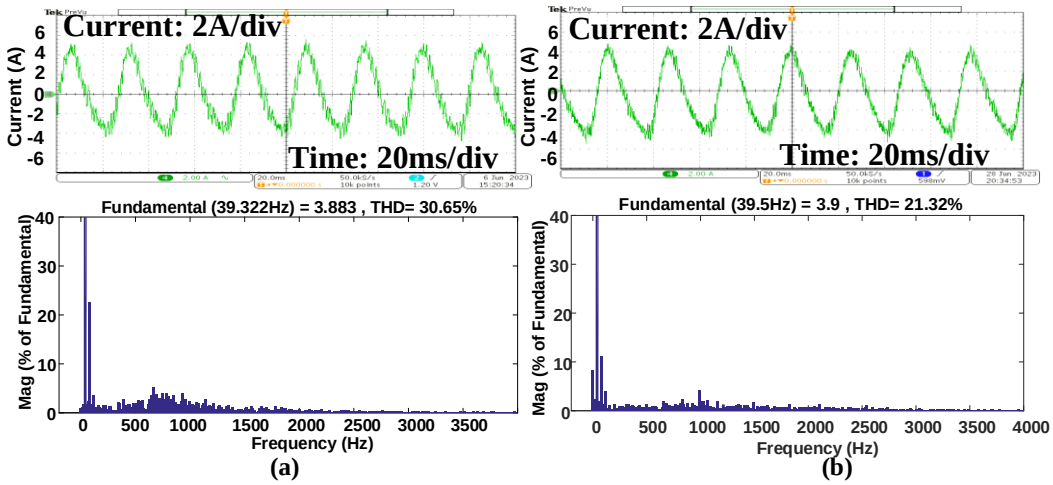

Figure 3.13 Current profile and %THD under load at 1000rpm for (a) C-DTC, and (b) proposed CSFHTC-DTC method

Figure 3.13 presents the phase current and its harmonic profile for (a) Classical Direct Torque Control (C-DTC) and (b) CSFHTC-DTC schemes. As the current harmonic distortion is influenced by the flux profile, the proposed CSFHTC-DTC demonstrates a notable reduction in current harmonic distortion compared to the classical C-DTC, as illustrated in Figure 3.13.

The proposed CSFHTC-DTC employs the same hysteresis torque controller as the C-DTC method; hence, the CSFHTC-DTC scheme does not disrupt the dynamic performance, as these dynamics are entirely dependent on the torque controller.

3.5.2 Experimental result analysis of the proposed CSTF-DTC scheme

The performance of an FPIM is examined in terms of flux ripple, torque ripple, and current harmonic distortion for a speed of high-speed of 1400 rpm, medium speed of 500 rpm, and low speed of 100 rpm under both load and no-load cases for proposed CSTF-DTC, existing DTC schemes [35], [38], and [70].

Figure 3.14 illustrates the torque and flux patterns under no load at speeds (I) 1400 rpm, (II) 500 rpm, and (III) 100 rpm for (a) C-DTC [35], (b) M-DTC [38], (c) CST-DTC [70], and (d) the proposed CSTF-DTC methods. Notably, I(a), II(a), and III(a) for C-DTC show flux ripples of 0.008 Wb, 0.009 Wb, and 0.0092 Wb, along with torque ripples of 0.153 Nm, 0.146 Nm, 0.14 Nm, respectively, at the corresponding speeds. I(b), II(b), and III(b) for M-DTC display flux ripples of 0.0065 Wb, 0.0064 Wb, 0.0064 Wb, and torque ripples of 0.16 Nm, 0.147 Nm, 0.1 Nm, respectively, for the corresponding speeds of 1400 rpm, 500 rpm, and 100 rpm. I(c), II(c), III(c) for CST-DTC exhibit a flux ripple of 0.0082 Wb, 0.0087 Wb, 0.0089 Wb, and torque ripples of 0.126 Nm, 0.11 Nm, 0.13 Nm, respectively, for the corresponding speeds of 1400 rpm, 500 rpm, and 100 rpm. In contrast, the proposed CSTF-DTC scheme represented by I(d), II(d), and III(d) reveals a notable reduction in flux ripples (0.004 Wb, 0.0041 Wb, 0.004 Wb) and torque ripples (0.11 Nm, 0.095 Nm, 0.1 Nm) at the corresponding speeds of 1400 rpm, 500 rpm, and 100 rpm.

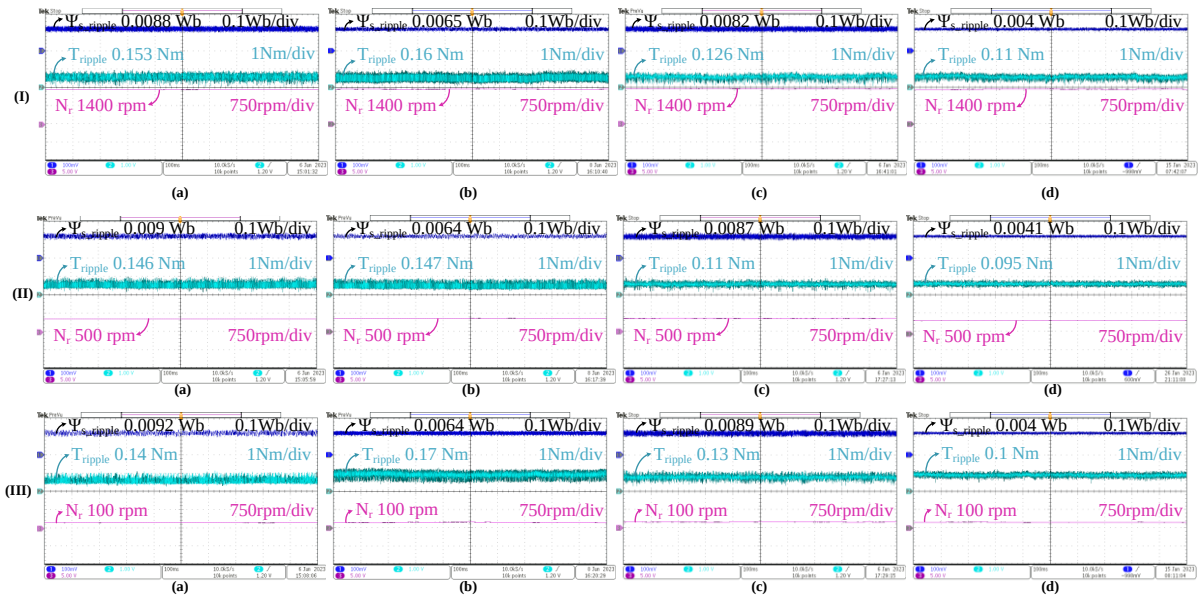

Figure 3.14 Flux, torque patterns at the speeds of (I) 1400 rpm (II) 500 rpm (III) 100 rpm for (a) C-DTC, (b) M-DTC, (c) CST-DTC, and (d) proposed CSTF-DTC at no load

Figure 3.15 illustrates the flux and torque patterns under a load of 2 Nm at speeds (I) 1400 rpm, (II) 500 rpm, and (III) 100 rpm for (a) C-DTC, (b) M-DTC, (c) CST-DTC, and (d) the proposed CSTF-DTC method. Notably, I(a), II(a), and III(a) for C-DTC show flux ripples of 0.0088 Wb, 0.0081 Wb, and 0.0085 Wb, along with torque ripples of 0.176 Nm, 0.146 Nm, 0.153 Nm, respectively, at the corresponding speeds. I(b), II(b), and III(b) for M-DTC display flux ripples of 0.006 Wb, 0.006 Wb, 0.0061 Wb, and torque ripples of 0.17 Nm, 0.152 Nm, 0.2 Nm, respectively, for the corresponding speeds of 1400 rpm, 500 rpm, and 100 rpm. I(c), II(c), III(c) for CST-DTC exhibit a flux ripple of 0.0082 Wb, 0.0082 Wb, 0.0083 Wb, and torque ripples of 0.146 Nm, 0.12 Nm, 0.134 Nm, respectively, for the corresponding speeds of 1400 rpm, 500 rpm, and 100 rpm. In contrast, the proposed CSTF-DTC scheme represented by I(d), II(d), and III(d) reveals a notable reduction in flux ripples (0.0036 Wb, 0.0032 Wb, 0.004 Wb) and torque ripples (0.12 Nm, 0.097 Nm, 0.11 Nm) at the corresponding speeds of 1400 rpm, 500 rpm, and 100 rpm.

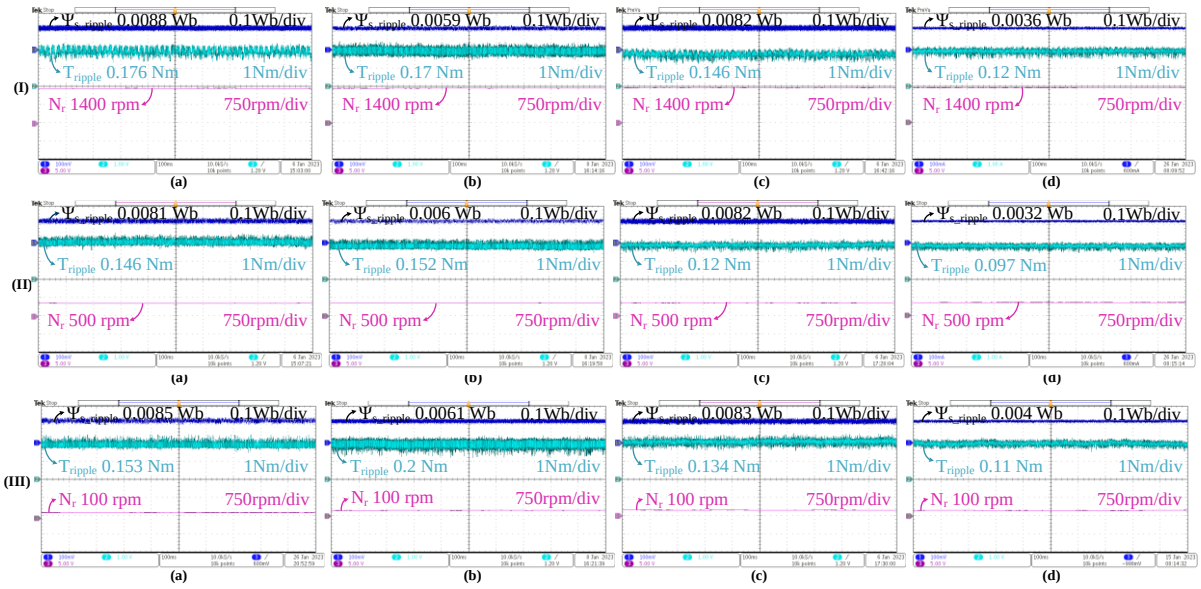

Figure 3.15 Flux, torque patterns at the speeds of (I) 1400 rpm (II) 500 rpm (III) 100 rpm for (a) C-DTC, (b) M-DTC, (c) CST-DTC, and (d) proposed CSTF-DTC at 2 Nm load

In Figure 3.16, depicting the current profile and harmonic distortion spectrum for speeds (I) 1000 rpm and (II) 500 rpm under a load of 2 Nm, the comparative analysis includes (a) C-DTC, (b) M-DTC, (c) CST-DTC, and (d) the proposed CSTF-DTC method. Notably, C-DTC (I(a), II(a)) yields *%THD* values of 30.65% and 27.93%, respectively, at speeds of 1000 rpm and 500 rpm. Similarly, M-DTC (I(b), II(b)) exhibits *%THD* values of 27.85% and 26.55% for the corresponding speeds. In comparison, CST-DTC (I(c), II(c)) produces %THD values of 23.06% and 22.66% at speeds of 1000 rpm and 500 rpm. Conversely, the proposed CSTF-DTC

scheme (I(d) and II(d)) achieves a substantial reduction in *%THD*, registering values of 16.58% and 13.36%, respectively. This suggests that the proposed CSTF-DTC method significantly diminishes phase current harmonic distortion when compared to other established control schemes [35], [38], and [70].

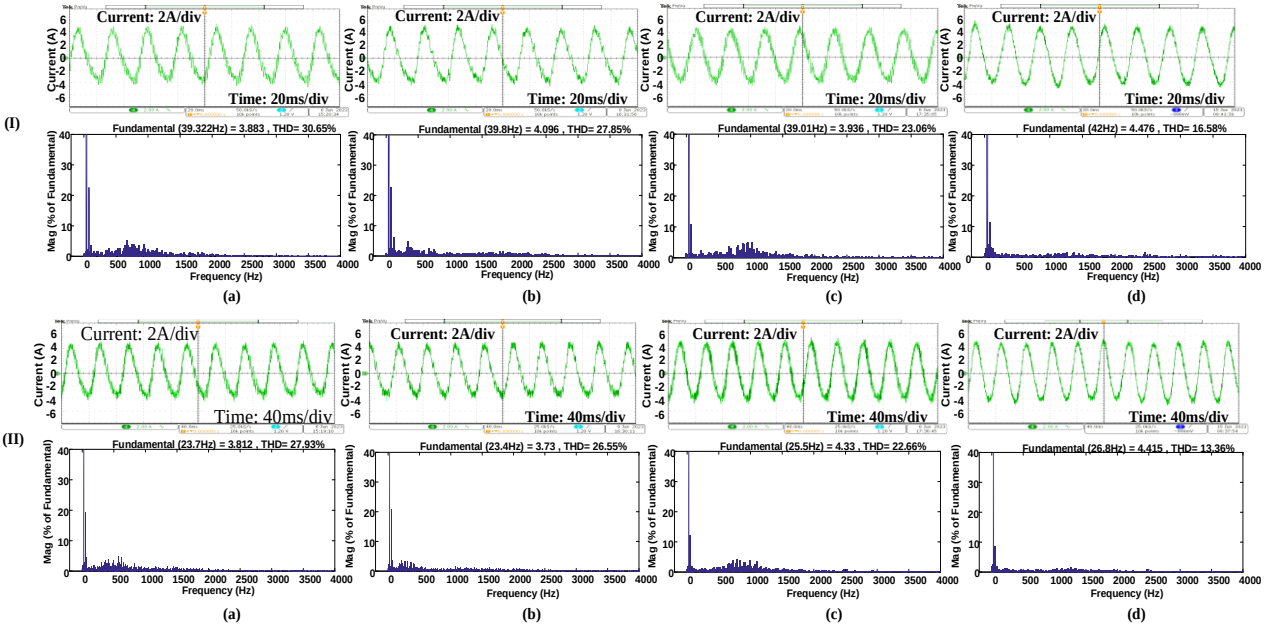

Figure 3.16 Current profile and %THD under load 2 Nm for (I)1000 rpm (II) 500 rpm for (a) C-DTC, (b) M-DTC, (c) CST-DTC and (d) proposed CSTF-DTC method

Table 3.3 Comparative Results Analysis Table for C-DTC, M-DTC, CST-DTC and proposed CSTF-DTC Methods

	Torque ripple (Nm)						**Flux ripple (Wb)**						**Current %THD**	
Speed (rpm)	**1400 rpm**		**500 rpm**		**100 rpm**		**1400 rpm**		**500 rpm**		**100 rpm**		**1000rpm**	**500rpm**
Load (Nm)	**0**	**2**	**0**	**2**	**0**	**2**	**0**	**2**	**0**	**2**	**0**	**2**	**2**	**2**
C-DTC method	0.153	0.176	0.146	0.146	0.14	0.153	0.0088	0.0088	0.009	0.0081	0.0092	0.0085	30.65	27.93
M-DTC method	0.16	0.17	0.147	0.152	0.17	0.2	0.0065	0.0059	0.0064	0.006	0.0064	0.0061	27.85	26.55
CST-DTC method	0.126	0.146	0.11	0.12	0.13	0.134	0.0082	0.0082	0.0087	0.0082	0.0089	0.0083	23.06	22.66
Proposed CSTFDTC method	**0.11**	**0.12**	**0.095**	**0.097**	**0.1**	**0.11**	**0.004**	**0.036**	**0.0041**	**0.0032**	**0.004**	**0.004**	**16.58**	**13.36**

Table 3.3 presents a comparative analysis of results for C-DTC, M-DTC, CST-DTC, and the proposed CSTF-DTC in terms of torque ripple, flux ripple, and current harmonic distortion across various speeds and loads. The findings indicate that the proposed CSTF-DTC demonstrates significant improvements in steady-state performance compared to other existing DTC techniques.

The dynamic performance of the proposed CSTF-DTC scheme is similar to proposed CST-DTC scheme as the same FOPI controller is used in the CSTF-DTC. The concept and design of FOPI controller in the CST controller is clearly discussed in the previous chapter (Chapter 2.3.2) and same process is followed in CSTF-DTC method. As the dynamics mainly depends on torque controller, FOPI only introduced in torque controller. To evaluate the dynamic profile of a 2-level VSI-controlled FPIM for C-DTC [35], M-DTC [38], CST-DTC [70], and the proposed CSTF-DTC schemes, the 5-phase induction motor is subjected to step load and step speed disturbances.

Figure 3.17 illustrates the step speed reversal disturbance from -500 rpm to 500 rpm for C-DTC, M-DTC, CST-DTC, and the proposed CSTF-DTC techniques. The proposed CSTF-DTC control scheme exhibits a comparable speed reversal response to existing DTC control techniques. Additionally, Figure 3.18 displays step speed disturbances from 500 rpm to 1000 rpm and 1000 rpm to 1400 rpm for C-DTC, M-DTC, CST-DTC, and the proposed CSTF-DTC scheme, showing similar response to other existing DTC schemes[35], [38], and [70]. Similarly, Figure 3.19 depicts the step load disturbance at 1000 rpm speed for C-DTC, M-DTC, CST-DTC, and the proposed CSTF-DTC, revealing that the proposed CSTF-DTC demonstrates comparable load dynamics to other existing DTC schemes. Based on the observations from Figure 3.17 to Figure 3.19, it can be concluded that the proposed CSTF-DTC control technique does not disturb the fast-speed dynamics characteristic of classical DTC control schemes.

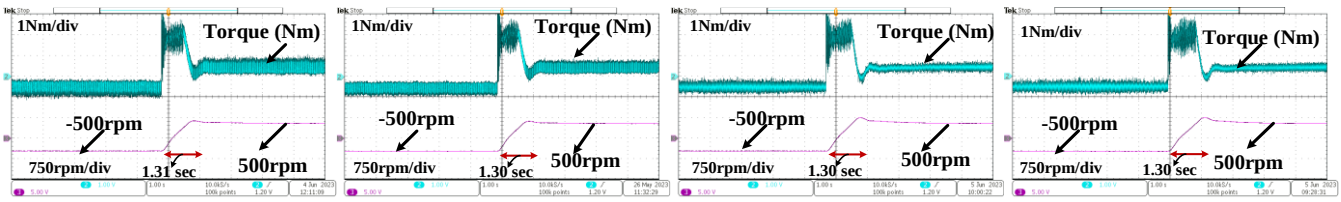

Figure 3.17 step speed reversal disturbance response from -500rpm to 500rpm for (a) C-DTC , (b) M-DTC (c) CST-DTC (d) proposed CSTF-DTC

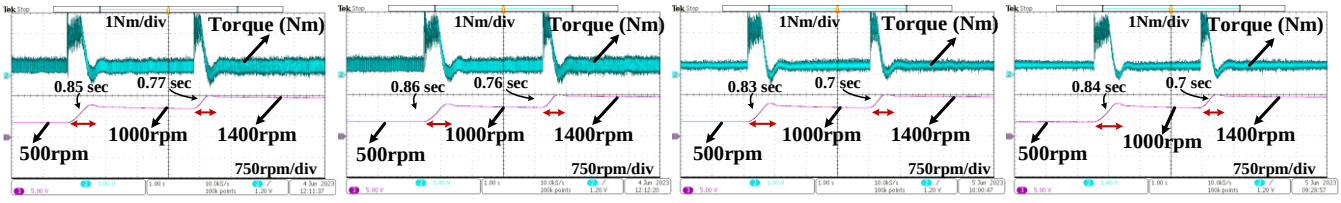

Figure 3.18 Step speed disturbance response from 500rpm-1000rpm-1400rpm for (a) C-DTC , (b) M-DTC (c) CST-DTC (d) proposed CSTF-DTC

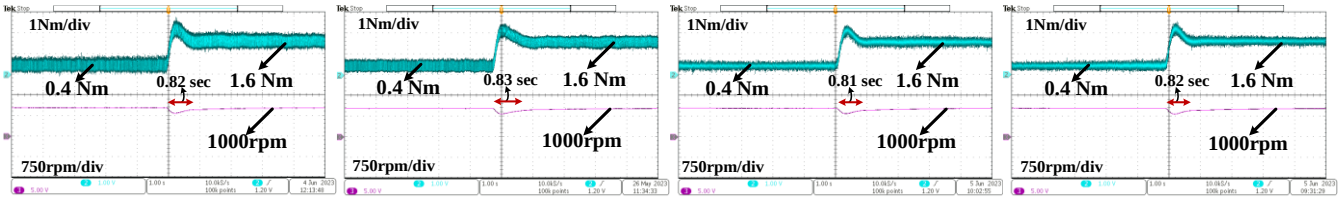

Figure 3.19 Step load disturbance response at a speed of 1000 rpm for (a) C-DTC, (b) M-DTC (c) CST-DTC (d) proposed CSTF-DTC

Table 3.4 displays the experimental parameters, including induction motor nameplate details and control algorithm control parameters.

Table 3.4 Parameters of 5-phase induction motor and Control scheme

Parameter	Value	parameter	Value	Parameter	Value
Power Rating	1 HP	No. of Poles (P)	4	DC link voltage(V)	150V
Stator inductance (L_s)	90.73mH	Rotor inductance (L_r)	90.73mH	Rated speed (rpm)	1400rpm
Stator resistance (R_s)	1.05Ω	Rotor resistance (R_r)	1.42 Ω	Speed PI controller	K_{ps}=0.02, K_{is}=0.005
Leakage inductance (L_{ls})	6mH	Inertia constant (J)	0.148Kg-m^2	CST PI controller	K_{pt}=110, K_{it}=23900
Mutual inductance (L_m)	84.73mH	Current rating (A)	3.4 A	CSF PI controller	K_{pf}=9900, K_{if}=0

3.6 Summary and conclusions

In this chapter, the initial focus is on replacing the Hysteresis Flux Controller of Classical DTC with a Constant Switching Flux Controller, tested on a VSI-fed 5-phase induction motor to assess its impact on steady-state performance in terms of torque ripple, flux ripple, and current harmonic distortion. The proposed CSFHTC-DTC demonstrates improvement in flux and current profiles without disturbing the torque profile and dynamics. Subsequently, a Constant Switching Torque Controller and Flux Controller-based Direct Torque Control (CSTF-DTC) are implemented on a VSI-fed 5-phase induction motor to enhance steady-state performance, emphasizing average flux ripple, average torque ripple, and current harmonic distortion without compromising fast dynamic performance. The efficacy of the proposed DTC control scheme is validated through experimental results and compared with recent existing DTC schemes for both steady-state and dynamic performances across different speeds and loading conditions. The proposed DTC methods utilize 10 virtual voltage vectors with a modified lookup table to eliminate harmonic plane components. The proposed CSTF-DTC exhibits fast dynamics as that of existing modified DTC control schemes for 5-phase induction motors, attributed to the use of FOPI in the CST controller, without compromising the generality of existing DTC control schemes. Therefore, the proposed CSTF-DTC technique

is recommended for applications in the field of high torque-density industries, addressing challenges such as smooth operation, good dynamics, and excellent fault-tolerant capability.

Chapter 4

Slip Speed Control-based DFC of 5-Phase Induction Motor to Improve Steady-State Performance

Chapter 4

Slip Speed Control-based DFC of 5-Phase Induction Motor to Improve Steady-State Performance

4.1 Introduction

In the previous chapters (Chapter 2, Chapter 3), the discussion primarily centered around constant switching torque and flux controller-based DTC schemes, aiming to enhance the steady-state performance of the 5-phase induction motor drive without compromising dynamic performance while maintaining the general structure of the classical DTC scheme. The proposed DTC methods such as CST-DTC, CSFHTC-DTC and CSTF-DTC in the previous chapters address the basic problems associated with classical DTC schemes. These proposed DTC control schemes suffer from complex concepts, complex computations, poor stability, and parameter sensitivity-based design constraints.

In this chapter, a slip speed/slip angle controller-based direct flux control (SSC-DFC) method is implemented with reference voltage error-based voltage vector selection to improve the steady-state performance indexes of the 5-phase induction motor drive with reduced control algorithm complexity. The DFC control avoids both hysteresis torque and flux controllers and replaces them with a simple voltage controller with a simplified lookup table. The DFC control method uses slip angle control which is obtained from processed speed error and torque error through the PI controller. In this chapter, the implementation of the proposed SSC-DFC scheme is discussed with relevant basic equations. The proposed SSC-DFC scheme is implemented with 20 virtual voltage vectors which are generated from 2 active vectors (10 vectors from large-medium set and 10 vectors from medium-small set vectors) over a control period to make xy-plane component zero. The DFC control scheme uses 2 separate lookup tables under high speeds and low speeds to get a better low-speed profile.

The SVM-DTC approach is developed in [40]-[43] to control the FPIM and maintain a constant switching frequency, which requires additional PI controllers, needs a coordinate transformation block and also affects low-speed performance. It also needs fast processors to track accurate dwell times over a control period. In [70], a modified DTC is suggested with a constant switching torque controller to achieve a nearly constant switching frequency. However, this scheme still exhibits a larger flux ripple due to the hysteresis flux controller, and xy components are not eliminated. The single-loop SVM-DTC scheme is implemented on a 3-phase induction motor with vector selection based on SVM and duty cycle optimization to

improve steady performance. This approach requires fast processors to obtain accurate dwell times for proper vector selection [71]. The proposed SSC-DFC scheme maintains a constant switching frequency for different rotor speeds by selecting a voltage vector for every control period and it avoids coordination transformation block, complex SVM, and optimum duty ratio-based calculations.

4.2 Implementation of the proposed SSC-DFC Scheme

In the conventional hysteresis-based DTC, the voltage vector is selected based on independent hysteresis-based torque and flux error statuses along with the flux vector location. In contrast, the proposed SSC-DFC uses a reference voltage vector error, which is obtained after processing the speed error, torque error, and flux angle correction stages sequentially to select a suitable voltage vector. The reference voltage error magnitude controls the stator flux, and the reference voltage vector angle controls the torque simultaneously. The vector selected in the proposed SSC-DFC control scheme utilizes a single-loop three-stage control method (speed control, torque control, flux angle control) to meet the torque and flux demands with a single control variable.

In the basic induction motor concept, the electromagnetic torque is proportional to slip speed under the assumption of constant airgap flux under low slip regions. The quick change in slip speed or slip frequency directly influences the electromagnetic torque. Due to high rotor inertia, the rotor flux position is treated as constant over one control period hence the electromagnetic torque is influenced by the change in the rotational angle of the stator flux over one control period [71]. The torque PI controller provides the necessary stator flux angle correction to the estimated stator flux angle ($\angle\Psi_s$) by processing the torque error (T_{err}) between the estimated torque (T_e) and the reference torque (T_e*) as in Equation (4.1).

$$\angle\Psi_s^{ref} = \angle\Psi_s + T_{err}\left(K_{pt} + \frac{K_{it}}{s}\right) \tag{4.1}$$

Where, $\angle\Psi_s$= estimated stator flux space angle

$\angle\Psi_s^{ref}$ = reference stator flux space angle

K_{pt}, K_{it} =torque PI controller constants

From the information on the ref. stator flux space angle ($\angle\Psi_s^{ref}$), the ref. stator flux vector (Ψ_s^{ref}) can be obtained with the given ref. stator flux magnitude $\left|\Psi_s^{ref}\right|$ as in (4.2).

$$\Psi_s^{ref} = \left|\Psi_s^{ref}\right| e^{j\angle\Psi_s^{ref}} \tag{4.2}$$

The reference voltage vector v_s^{ref} can be achieved from (4.2) as in (4.3)

$$V_s^{ref} = I_s R_s + \left(\frac{\Psi_s^{ref} - \Psi_s}{T_s}\right) \tag{4.3}$$

The voltage controller is introduced to trace the reference voltage space vector which helps to meet the demanded stator flux and electromagnetic torque of a FPIM. The difference in reference voltage vector from the previous sample to the present sample will trigger the suitable voltage vector to meet the updated reference vector and it indirectly affects the stator flux and torque.

The voltage controller is implemented as in (4.4).

$$V_{stat} = +1 \quad (V_s^{ref}(k) - V_s^{ref}(k-1)) > 0$$
$$V_{stat} = -1 \quad (V_s^{ref}(k) - V_s^{ref}(k-1)) < 0 \qquad (4.4)$$

Where, $V_s^{ref}(k)$=Present sample of ref. voltage vector

$V_s^{ref}(k-1)$=Previous sampled ref. voltage vector

The voltage controller status V_{stat} is +1, or -1, which means to select forward voltage vector or backward voltage vector respectively. The reference voltage space vector arbitrarily lies on the αβ-complex plane with the help of the proposed voltage controller.

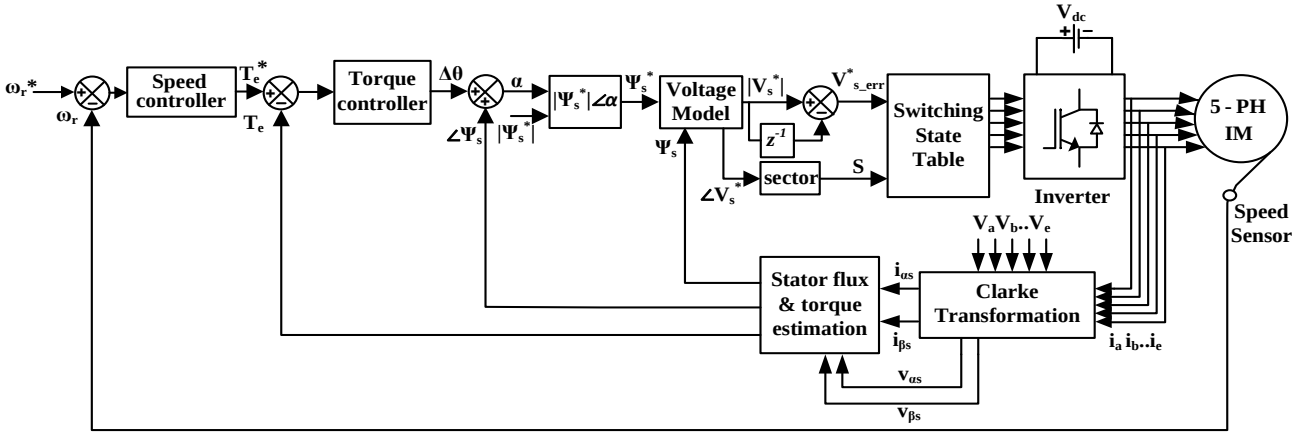

Figure 4.1 Control diagram proposed SSC-DFC control scheme of FPIM

The control diagram of the proposed SSC-DFC control scheme is illustrated in Figure 4.1. In this figure, the speed error is processed through the speed PI controller, yielding the reference torque (T_e*). The reference torque is then compared with the estimated torque, and the torque error is processed through the torque PI controller, providing slip angle correction information. Adding the slip angle to the estimated flux angle results in the reference flux angle information. Using the reference flux angle and reference flux magnitude, the reference stator flux vector is formed. The reference voltage vector is obtained from the voltage model equation (4.3) based on the reference stator flux vector over a sample period. Depending on the voltage reference vector error, the suitable voltage vector is selected to meet the required torque and flux demands.

The electromagnetic torque (T_e) and stator flux (Ψ_s) are estimated from the below equations of an FPIM.

The stator voltage equation is written below (4.5)

$$V_s = I_s R_s + \frac{d\Psi_s}{dt} \tag{4.5}$$

Where I_s = stator phase current

R_s= stator resistance

The estimated stator flux (Ψ_s) will be expressed as

$$\Psi_s = \int (V_s - I_s R_s)\, dt \tag{4.6}$$

The estimation of electromagnetic torque can be expressed in terms of flux linkages and stator currents as below (4.7)

$$T_e = \frac{5}{2}\frac{P}{2} imag(\Psi_s^* I_s) \tag{4.7}$$

Where P- no. of stator poles

Figure 4.2 shows the space vector diagram in αβ plane and xy plane, and it is observed that the small vectors in the αβ plane are mapped as large vectors with counter direction in the xy plane or vice versa. Similarly, the medium vectors in the αβ plane will be mapped as medium vectors in the xy plane [35] as in Figure 4.2. The 20 virtual voltage vectors are generated from large-medium and medium-small sets of vectors (10 large virtual vectors from large medium vectors, and 10 small virtual vectors from medium-small vectors) by using the volt-sec balance technique [35] to make zero xy-plane currents. The suitable voltage vectors are selected with proper dwell times over a sample period such that the resultant voltage vector magnitude in the xy plane will become zero.

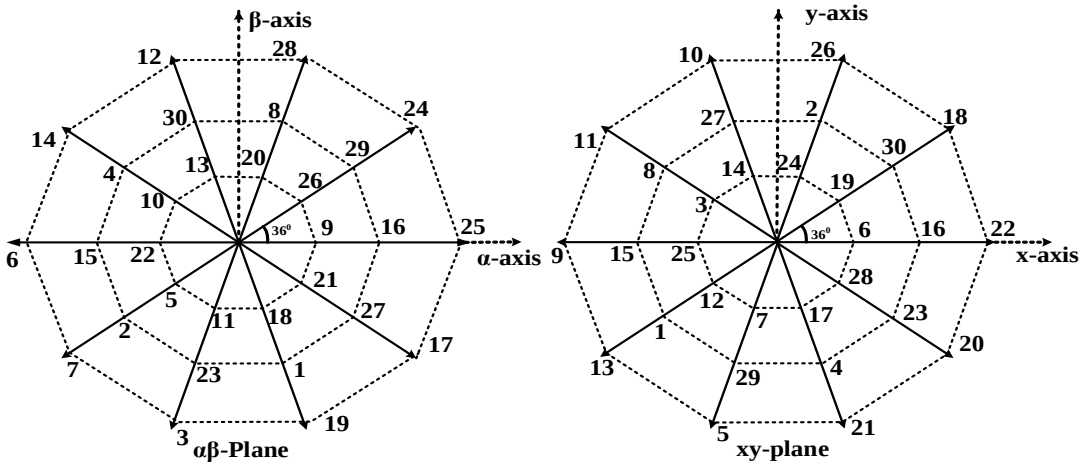

Figure 4.2 Voltage spacer vector locations of a 2-level 5-leg VSI in both the fundamental (αβ) and harmonic (xy) planes

The generation of virtual voltage vectors from large and medium vectors is explained in the previous section 3.3.1. In the same manner, the 10 large virtual vectors are generated from large medium vectors, and 10 small virtual vectors are generated from medium-small vectors of αβ plane as shown in Figure 4.3. The location of large virtual vectors (V_1 to V_{10}), and small virtual vectors (V_{11} to V_{20}) are shown in Figure 4.4 with 10 sectors in the αβ plane. These 20 *VVs* (V_1-V_{20}) are used to form a lookup table for the proposed method. The suitable virtual vectors are selected to synthesize the reference voltage vector from lookup table 1(Table 4.1) with large virtual vectors under high-speed cases and lookup table 2 (Table 4.2) with small virtual vectors under low-speed cases.

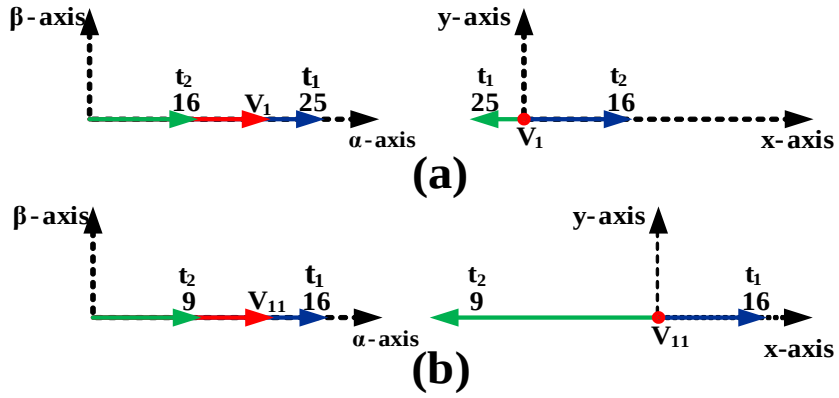

Figure 4.3 Virtual vector generation (red color) in both αβ-plane and xy-plane for (a) large *VVs* and (b) small *VVs*

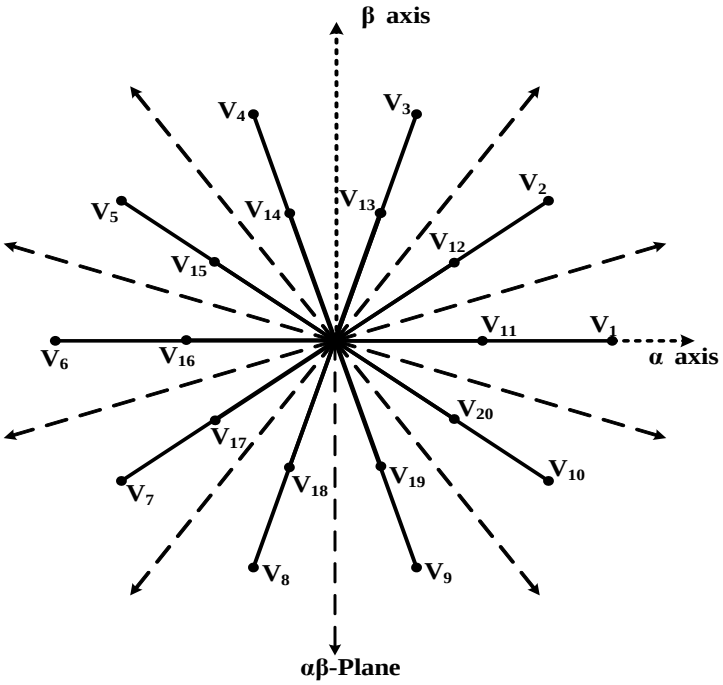

Figure 4.4 Virtual voltage vectors V_1-V_{20} location diagram

Table 4.1 Virtual vector selection table for proposed SSC-DFC scheme under high-speed

V_{stat}	Sector									
	1	2	3	4	5	6	7	8	9	10
+1	V_2	V_3	V_4	V_5	V_6	V_7	V_8	V_9	V_{10}	V_1
-1	V_1	V_2	V_3	V_4	V_5	V_6	V_7	V_8	V_9	V_{10}

Table 4.2 Virtual vector selection table for proposed SSC-DFC scheme under low-speed

V_{stat}	Sector									
	1	2	3	4	5	6	7	8	9	10
	V_{12}	V_{13}	V_{14}	V_{15}	V_{16}	V_{17}	V_{18}	V_{19}	V_{20}	V_{11}
-1	V_{11}	V_{12}	V_{13}	V_{14}	V_{15}	V_{16}	V_{17}	V_{18}	V_{19}	V_{20}

The proposed controller checks for voltage error for every sample time i.e. 100 µsec, the controller changes its status for every 100 µsec and hence the switching frequency is maintained constant irrespective of operating speeds and load conditions. The proposed SSC-DFC scheme changes the vector for every control period unlike the hysteresis-based DTC scheme hence it gives the reduced torque ripple. Also proposed SSC-DFC scheme voltage model checks for stator flux error for every sample rate, the possible precise flux control causes reduced flux ripple. Hence the proposed SSC-DFC control scheme reduces the torque ripple, flux ripple, and current distortion with constant switching frequency while maintaining the fast dynamics.

4.3 Experimental result analysis

The proposed SSC-DFC method has been experimentally tested on a VSI-fed FPIM and compared with existing DTC schemes to assess its effectiveness in terms of torque ripple, flux ripple, and current harmonic distortion without affecting fast dynamics present in existing DTC schemes. The experimental hardware setup details are provided in Appendix I. For a fair comparison, the existing hysteresis-based DTC schemes and the proposed SSC-DFC schemes are implemented at a sampling rate of 100 µsec. The existing DTC schemes are implemented with a 4% flux hysteresis band and a 10% torque hysteresis band with respect to their rated quantities. The control algorithms are executed on a dSPACE-1202 RTI controller using MATLAB/Simulink software. The motor drive under test features a 5-phase induction motor coupled with a 1HP DC generator, loaded with resistive lamp loads. The hardware test setup includes an IGBT-based 5-leg inverter module with a built-in gate driver board, receiving gate pulses directly from the dSPACE 1202 controller. A 1024 PPR encoder is used for accurate measurement of rotor speeds. The 5-phase currents and DC link voltages are measured using

LEM LA-25P current sensors and LV-25P voltage sensors, respectively. These sensed signals are fed to the control circuit through ADC ports of the dSPACE 1202 controller.

4.3.1 Steady state performance analysis

The performance of the proposed control scheme is evaluated based on reduced torque ripple, flux ripple, current %THD, and switching frequencies at various speeds and loading cases when compared with existing DTC schemes such as C-DTC [35], and M-DTC [38].

The average flux ripple and torque ripples are computed from the recorded flux and torque patterns using the equation (4.8). The calculations are based on the captured data points at a rate of 10000 samples per second for C-DTC, M-DTC, and the proposed SSC-DFC schemes.

$$Torque/flux_{ripple} = \sqrt{\frac{1}{N}\sum_{i=1}^{N}\left(X(i) - X_{avg}\right)^2} \tag{4.8}$$

Where $X(i)$ =torque/flux at the i^{th} sample

X_{avg}=average torque/flux over N samples

Figure 4.5 illustrates the torque and flux patterns at speeds of (I) 1400 rpm, (II) 500 rpm, (III) 100 rpm for (a) C-DTC, (b) M-DTC, and (c) the proposed SSC-DTC schemes under no-load conditions. It can be observed that (a) C-DTC exhibits flux ripple of 0.008 Wb, 0.009 Wb, 0.0091 Wb, and torque ripple of 0.153 Nm, 0.146 Nm, and 0.142 Nm, respectively, for the corresponding speeds. Similarly, (b) M-DTC shows flux ripple of 0.0065 Wb, 0.0064 Wb, 0.0064 Wb, and torque ripple of 0.16 Nm, 0.147 Nm, and 0.17 Nm, respectively, for the corresponding speeds. In contrast, (c) the proposed SSC-DFC scheme exhibits reduced flux ripple of 0.0055 Wb, 0.0034 Wb, 0.0034 Wb, and torque ripple of 0.14 Nm, 0.094 Nm, 0.1 Nm, respectively, for the corresponding speeds.

Similarly, Figure 4.6 presents the flux and torque patterns at (I) 1400 rpm, (II) 500 rpm, (III) 100 rpm for (a) C-DTC, (b) M-DTC, and (c) the proposed SSC-DFC scheme under loaded conditions. C-DTC produces flux ripple of 0.008 Wb, 0.008 Wb, 0.0085 Wb, and torque ripple of 0.176 Nm, 0.156 Nm, and 0.153 Nm, respectively, for the corresponding speeds. M-DTC exhibits flux ripple of 0.006 Wb, 0.006 Wb, and 0.0061 Wb, and torque ripple of 0.17 Nm, 0.152 Nm, 0.191 Nm, respectively, for the corresponding speeds. The proposed SSC-DFC scheme shows reduced flux ripple of 0.005 Wb, 0.0033 Wb, 0.0034 Wb, and torque ripple of 0.161 Nm, 0.11 Nm, and 0.11 Nm, respectively. From Figures 4.5 and 4.6, it can be concluded

that the proposed SSC-DTC control scheme exhibits a great reduction in average flux ripple across a wide range of speeds and various loads. This improvement is due to the precise stator flux control scheme implemented in the proposed algorithm. Furthermore, an appreciable reduction in torque ripple is observed at high speeds, while a significant reduction in torque ripple is achieved at low speeds. This advantageous outcome is a result of employing two switching tables, one for high speeds and another for low speeds, in the proposed SSC-DTC scheme.

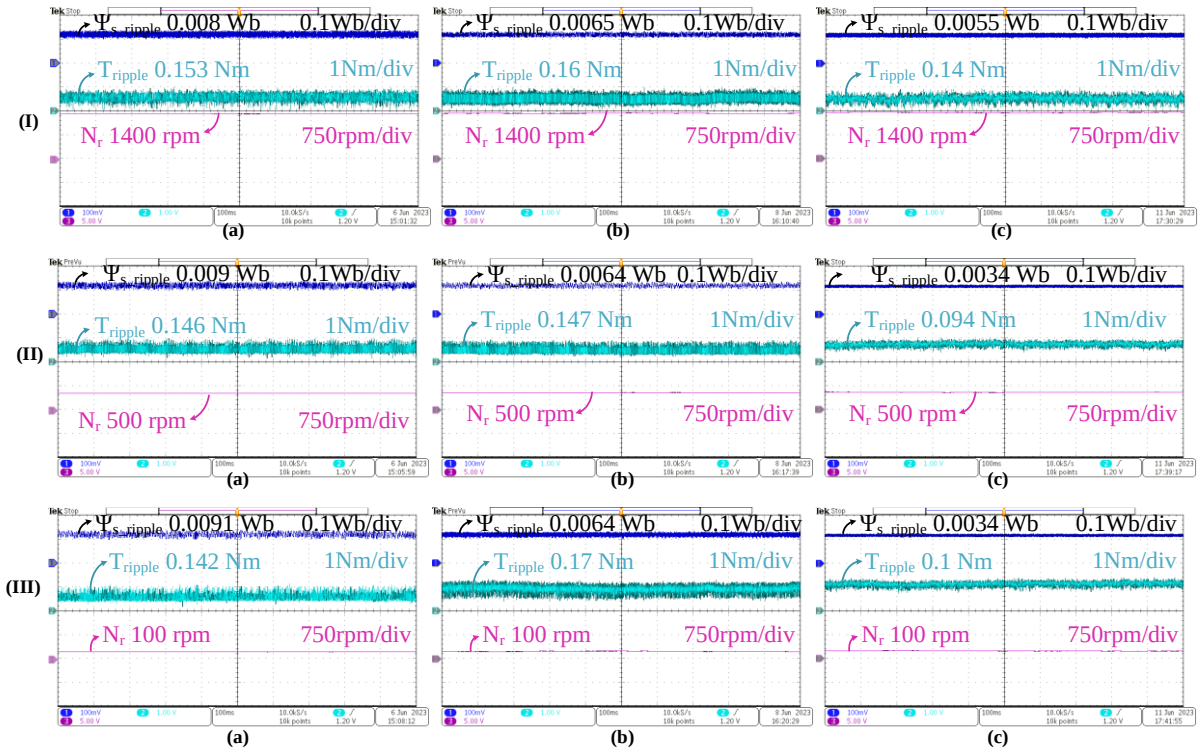

Figure 4.5 Torque and flux profile at (I) 1400 rpm (II) 500 rpm (III) 100 rpm for (a) C-DTC (b) M-DTC (c) proposed SSC-DFC scheme under no load case

Figure 4.7 illustrates the fundamental and harmonic plane currents for the three methods, showcasing the elimination of harmonic plane components through the virtual voltage vector concept. The proposed SSC-DFC scheme exhibits superior fundamental plane current profiles compared to existing DTC schemes, due to the precise flux control scheme employed. The analysis of phase current harmonic distortion under different speeds for classical C-DTC [35], M-DTC [38], and the proposed SSC-DFC methods is presented in Figure 4.8. The phase current waveforms and their harmonic spectra at (I) 1000 rpm and (II) 500 rpm for (a) C-DTC, (b) M-DTC, and (c) proposed SSC-DFC methods are depicted. It is observed that C-DTC shows a total harmonic distortion (*%THD*) of 30.86% and 27.93% for the corresponding speeds. M-DTC produces a *%THD* of 27.86% and 26.55%, while the proposed SSC-DFC scheme exhibits a

reduced *%THD* of 16.44% and 15.48% for the corresponding speeds. This reduction is due to the precise flux control method, as harmonic distortion is significantly influenced by the flux profile. It is also observed that there is a spike in the harmonic spectra at 1700 Hz in the proposed SSC-DFC scheme, representing the inverter switching frequency. This frequency remains consistent across different speeds, indicating the change of switching state for every sampling instant T_s with the proposed voltage controller.

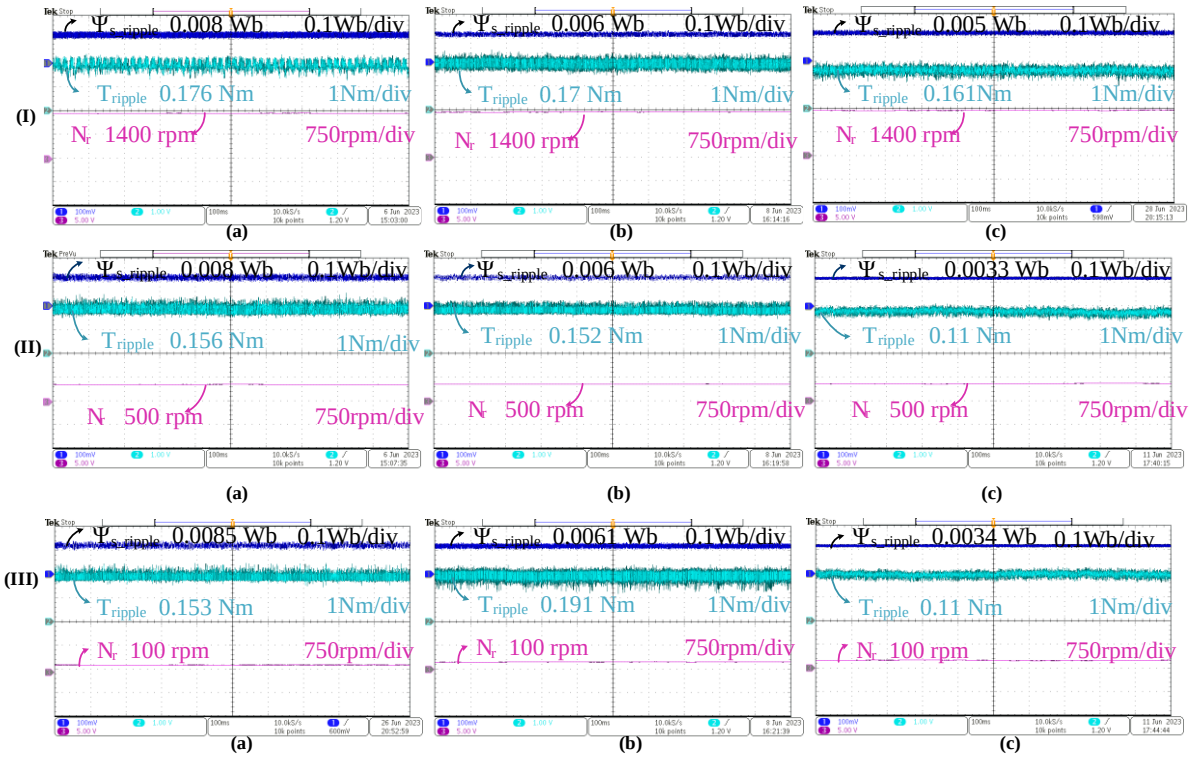

Figure 4.6 Torque and flux profile at (I) 1400 rpm (II) 500 rpm (III) 100 rpm for (a) C-DTC (b) M-DTC (c) proposed SSC-DFC scheme under load case

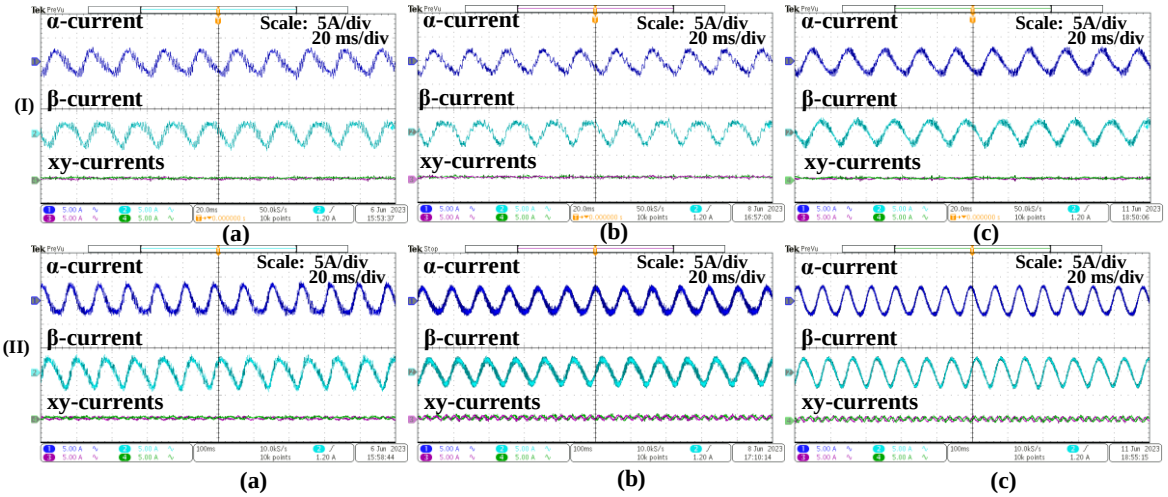

Figure 4.7 Fundamental and harmonic plane currents (I) 1000 rpm (II) 100 rpm for (a) C-DTC (b) M-DTC (c) proposed SSC-DFC scheme

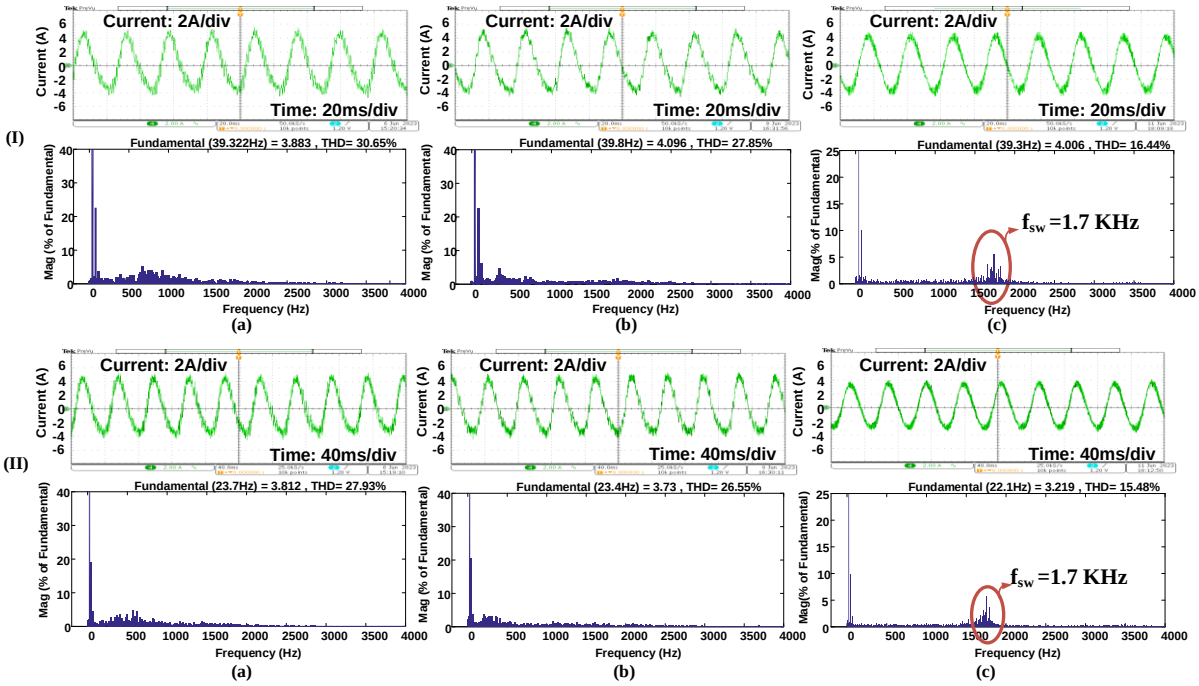

Figure 4.8 The phase current waveforms and %THD at (I) 1000 rpm and (II) 500 rpm for (a) C-DTC, (b) M-DTC, and (c) the proposed SSC-DFC scheme under load.

Table 4.3 shows the comparative analysis report of the C-DTC, M-DTC, CSFHTC-DTC (explained in chapter 3), and the proposed SSC-DFC methods in terms of torque ripple, flux ripple, and current %THD for various speeds under no load and loaded conditions. It is observed that the proposed SSC-DFC scheme shows better steady-state performance compared to other DTC methods.

Table 4.3 Comparative Results Analysis Table for C-DTC, M-DTC, CSFHTC-DTC and proposed SSC-DFC Methods

Method	**Average Torque Ripple (Nm)**						**Average Flux Ripple (Wb)**						**Phase current %THD (load)**	
Speed	**1400 rpm**		**500 rpm**		**100 rpm**		**1400 rpm**		**500 rpm**		**100 rpm**			
Load	**No load**	**Load**	**No load**	**load**	**No load**	**load**	**No load**	**load**	**No load**	**load**	**No load**	**load**	**1000rpm**	**500rpm**
C-DTC	0.153	0.176	0.146	0.156	0.142	0.153	0.008	0.008	0.009	0.008	0.0091	0.0085	30.86	27.93
M-DTC	0.16	0.17	0.147	0.152	0.17	0.191	0.0065	0.006	0.0064	0.006	0.0064	0.0061	27.86	26.55
CSFHTC-DTC	0.157	0.165	0.147	0.145	0.138	0.15	0.0056	0.0056	0.006	0.0057	0.006	0.0063	21.32	20.4
SSC-DFC	0.14	0.161	0.094	0.11	0.1	0.11	0.0055	0.0050	0.0034	0.0033	0.0034	0.0034	18.44	15.48

4.3.2 Dynamic Performance Analysis

The dynamic performance is analyzed by introducing step speed and load disturbances to the induction motor drive for C-DTC, M-DTC, and the proposed SSC-DFC schemes. In Figure 4.9, (I) depicts the step speed reversal response, (II) shows the step speed disturbance response, and (III) illustrates the step load disturbance response for (a) C-DTC, (b) M-DTC, and (c) the proposed SSC-DFC schemes. From Figure 4.9, it is observed that the proposed SSC-

DFC scheme exhibits dynamics similar to classical DTC methods due to the error-based voltage vector selection method.

4.4 Summary and Conclusions

In this chapter, a Slip Speed Control-based Direct Flux Control method (SSC-DFC) is implemented on a 2-level VSI-fed 5-phase induction motor to improve steady-state performance in terms of average flux ripple, torque ripple, current harmonic distortion, and switching frequencies without disturbing the fast dynamics, as seen in existing DTC schemes. The proposed control scheme simplifies the control structure without complex and vague design equations. Also, the proposed SSC-DFC scheme uses two simplified lookup tables during high speeds and low speeds, respectively, for proper voltage vector selection to meet the required torque and flux demands.

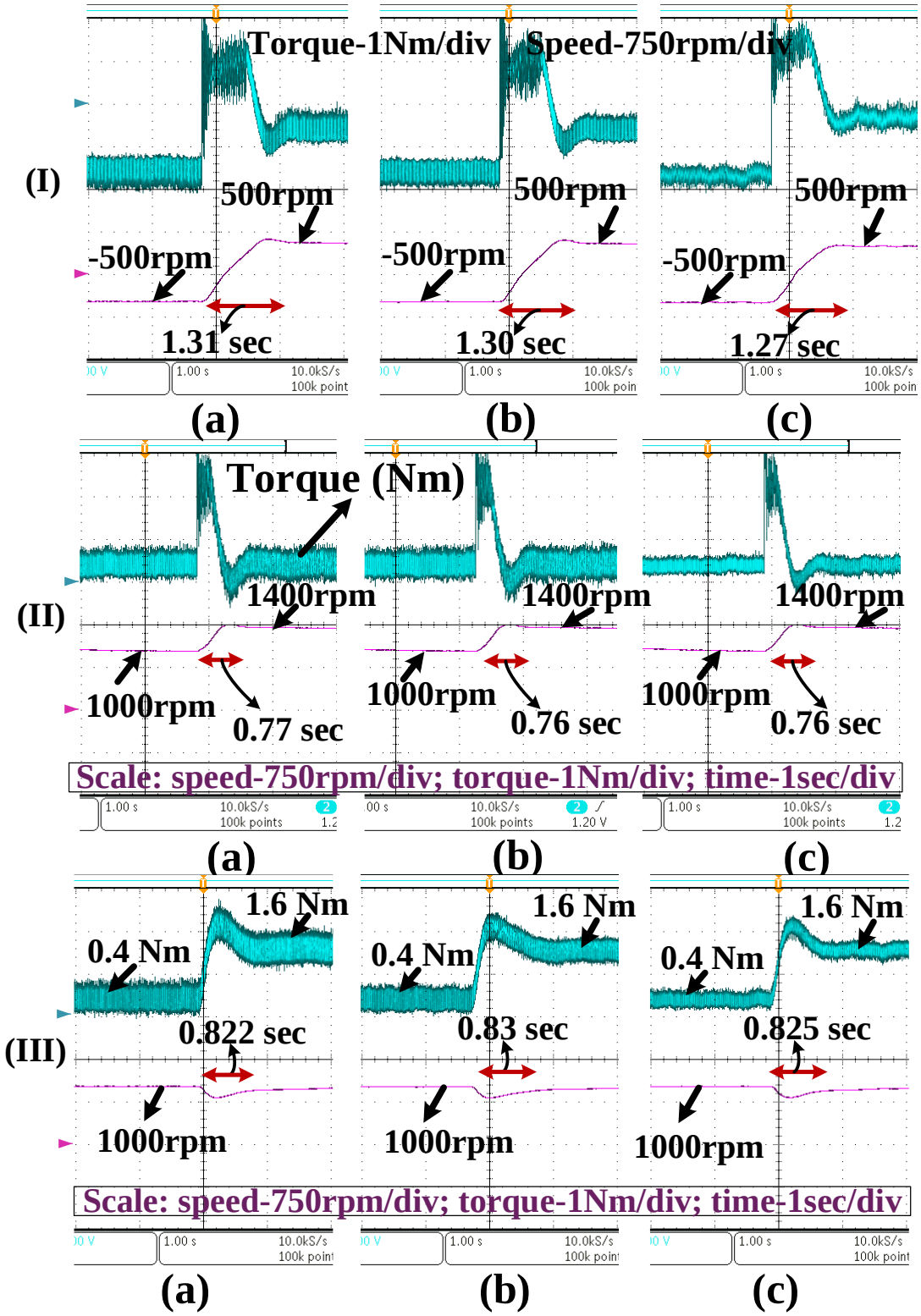

Figure 4.9 Dynamic response analysis at (I) speed reversals (II) step speed disturbance (III) step load disturbance for (a) C-DTC, (b) M-DTC, (c) proposed SSC-DTC scheme

The effectiveness of the proposed SSC-DFC scheme is tested experimentally for various speeds and loading conditions, and notable reductions in average flux ripple, torque ripple, and current harmonic distortion are observed while maintaining constant switching frequencies. The

proposed DTC exhibits fast dynamics, as that of the hysteresis-based DTC methods since the proposed DTC uses error-based voltage vector selection. Therefore, it is advised that the proposed SSC-DFC technique is beneficial for high torque-density industrial appliances where the key limitations are smooth steady-state operation, good dynamics, and great fault-tolerant capability.

Chapter 5

A Modified Lookup Table-based DTC Scheme for Dual Inverter fed Open-End Winding Five-Phase Induction Motor Drive

Chapter 5

A Modified Lookup Table-based DTC Scheme for Dual Inverter fed Open-End Winding Five-Phase Induction Motor Drive

5.1 Introduction

In previous chapters, modified DTC control schemes were implemented on single VSI-fed 5-phase induction motors to improve the steady-state profile. The single inverter-fed 5-phase induction motor has limited switching states and produces only 2-level inverter voltages. The single 2-level VSI-fed induction motor drive suffers from unavoidable common-mode voltage, high voltage stress across switches, a limited number of levels in inverter output voltages, and less fault-tolerant capability. This necessitates the use of multi-level inverter topologies for induction motor drives, and they have several advantages, such as fault tolerance, redundant switching states, modularity, reduced torque and flux ripple, fault-tolerant capacity, and multi-levels in inverter output voltages. The open-end winding 5-phase induction motor configuration is obtained by opening the neutral point of the motor and connecting two 2-level inverters on both stator winding end connections, as shown in Figure 5.1. The switching states in a dual inverter system are determined by the combination of switching states from both inverters. The combination of these switching states plays a crucial role in controlling the output voltage, common mode voltage, and overall performance of the drive. Understanding and optimizing these switching states are essential for achieving desired performance characteristics such as reduced harmonics, zeroed common mode voltage, and precise control of motor drives.

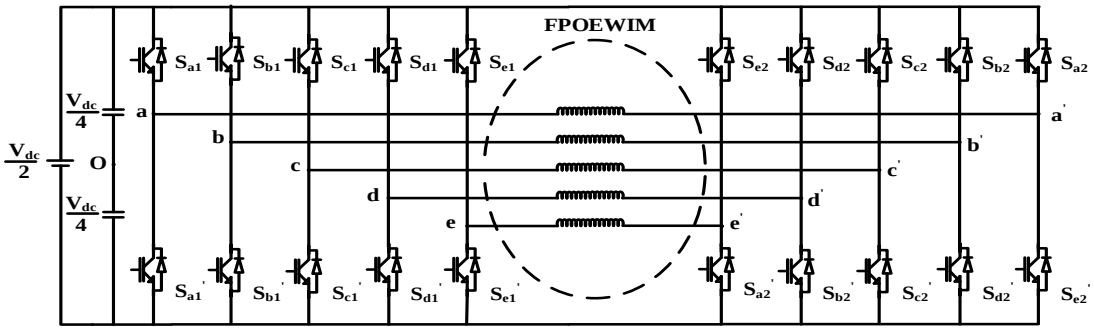

Figure 5.1 Single DC source fed dual inverter controlled open-end winding 5-phase induction motor

The dual inverter-fed 5-phase open-end winding induction motor (DIFPOEWIM) produces 3-level voltages with 1:1 DC link voltage ratios of both inverters. Utilizing specialized switching schemes that effectively eliminate common mode voltages from the windings enables the use of a single DC source to power both inverters in dual inverter-fed open-end winding drives. A key benefit of this strategy is the substantial reduction in the required DC link voltage for a given motor voltage w.r.t star-connected motor fed with a single inverter and it also avoids the use of bulky isolation transformers. However, this specific switching scheme essential for dual inverter-fed open-end winding with a single DC source typically involves the reduction of switching state possibilities across the motor windings. In addition to eliminating common mode voltage, the removal of xy-plane components in five-phase machines is also necessary, and this is accomplished through the use of the virtual voltage vector concept. Despite these challenges, the exploration of direct torque control (DTC) schemes for multiphase dual inverter-fed open-end winding induction motor drives has not been explored much, providing an avenue for further research and potential advancements in this field. Limited research exists on DTC control for dual inverter-fed multi-phase induction motor drives [55]-[58]. Further exploration is crucial to uncover the potential benefits of DIFPOEWIM and to further improvement of the steady-state performance.

In this chapter, a modified lookup table-based DTC control scheme is implemented on DIFPOEWIM, featuring 30 virtual voltage vectors to enhance steady-state performance, while concurrently eliminating harmonic plane components and common mode voltage. The proposed DTC control scheme for DIFPOEWIM effectively mitigates torque ripple, flux ripple, and current harmonic distortion in comparison to existing DTC schemes, as classical DTC approaches on DIFPOEWIM tend to underutilize available switching states, resulting in higher torque ripple, flux ripple, and harmonic distortion, whereas the proposed DTC scheme improves these factors by expanding the range of switching state combinations.

5.2 Modelling of dual inverter fed five-phase open-end winding induction motor

The circuit of DIFPOEWIM is shown in Figure 5.1 and it contains an open-end winding induction motor supplied with two 2-level VSIs fed from a common DC source. And it produces a 3-level voltage across each phase. The modeling of a 5-phase open-end winding induction motor can be done as follows.

The 5-phase voltages of DIFPOEWIM $V_{aa'}\ldots.V_{ee'}$ are converted into a stationary reference model in the fundamental(αβ) plane as $V_{\alpha s}$, $V_{\beta s}$, and harmonic (xy) plane as (V_{xs}, V_{ys}) and V_0 as shown in 5.1.

$$\begin{bmatrix} V_{\alpha s} \\ V_{\beta s} \\ V_{xs} \\ V_{ys} \\ V_{os} \end{bmatrix} = \frac{2}{5}\begin{bmatrix} cos(0) & cos(\alpha) & cos(2\alpha) & cos(3\alpha) & cos(4\alpha) \\ sin(0) & sin(\alpha) & sin(2\alpha) & sin(3\alpha) & sin(4\alpha) \\ cos(0) & cos(3\alpha) & cos(\alpha) & cos(4\alpha) & cos(2\alpha) \\ sin(0) & sin(3\alpha) & sin(\alpha) & sin(4\alpha) & sin(2\alpha) \\ 1/2 & 1/2 & 1/2 & 1/2 & 1/2 \end{bmatrix}\begin{bmatrix} V_{aa'} \\ V_{bb'} \\ V_{cc'} \\ V_{dd'} \\ V_{ee'} \end{bmatrix} \quad (5.1)$$

The stator phase voltages($V_{aa'}\ldots V_{ee'}$) of FPOEWIM in (5.1) are expressed in terms of pole voltages of inverter I ($V_{a0}\ldots V_{b0}$) and inverter II ($V_{a'0}\ldots V_{b'0}$) as in (5.2). The inverter pole voltages may be ($V_{dc}/2$) or *0* depending on the switch state *1* or *0*.

$$\begin{bmatrix} V_{aa'} \\ V_{bb'} \\ V_{cc'} \\ V_{dd'} \\ V_{ee'} \end{bmatrix} = \frac{1}{5}\begin{bmatrix} 4 & -1 & -1 & -1 & -1 \\ -1 & 4 & -1 & -1 & -1 \\ -1 & -1 & 4 & -1 & -1 \\ -1 & -1 & -1 & 4 & -1 \\ -1 & -1 & -1 & -1 & 4 \end{bmatrix}\begin{bmatrix} V_{a0} - V_{a'0} \\ V_{b0} - V_{b'0} \\ V_{c0} - V_{c'0} \\ V_{d0} - V_{d'0} \\ V_{e0} - V_{e'0} \end{bmatrix} \quad (5.2)$$

Where V_{a0}, V_{b0}, V_{c0}, V_{d0}, V_{e0}=Inverter I pole voltages ($V_{x0}=S_x*V_{dc}/2$)

$V_{a'0}$, $V_{b'0}$, $V_{c'0}$, $V_{d'0}$, $V_{e'0}$= Inverter II pole voltages ($V_{x'0}=S_{x'}*V_{dc}/2$)

S_x and $S_{x'}$ =*0* or *1*; *x*=phase *a..e.*; *x'*=phase *a'..e'*.

The induction motor can be modelled by assuming the machine is distributed winding and hence only fundamental (αβ) plane components are responsible for torque production and the harmonic plane only creates ohmic losses. The harmonic plane components can be neglected in (5.1). The induction motor modelling can be done with the equations (5.3) - (5.6).

The stator voltage balancing equations 5-phase induction motor in a stationary reference frame can be written as follows.

$$V_{\alpha s} = I_{\alpha s}R_s + \frac{d\,\Psi_{\alpha s}}{dt}$$
$$V_{\beta s} = I_{\beta s}R_s + \frac{d\,\Psi_{\beta s}}{dt} \quad (5.3)$$

Where $V_{\alpha s}$, $V_{\beta s}$ = stator phase voltage in volts

I_s= stator phase current in amperes

R_s=stator resistance in ohms

$\Psi_{\alpha s}$, $\Psi_{\beta s}$= stator flux linkages in the stationary frame

The rotor voltage balancing equations in stationary reference frame can be written below

$$V_{\alpha r} = I_{\alpha r}R_s + \frac{d\,\Psi_{\alpha r}}{dt} - \omega_r\,\Psi_{\beta r}$$
$$V_{\beta r} = I_{\beta r}R_s + \frac{d\,\Psi_{\beta r}}{dt} + \omega_r\,\Psi_{\alpha r} \quad (5.4)$$

Where $V_{\alpha r}$, $V_{\beta r}$ = rotor phase voltage in volts

I_r= rotor phase current in amperes

R_r=rotor resistance in ohms

$\Psi_{\alpha r}$, $\Psi_{\beta r}$ =Rotor flux linkages in the stationary frame

ω_r=Rotor speed in electrical rad/sec

The electromagnetic torque (T_e) produced in 5-phase induction motor is expressed as (5.5)

$$T_e = \frac{5}{2}\frac{P}{2}\left(\Psi_{\alpha s} i_{\beta s} - \Psi_{\beta s} i_{\alpha s}\right) \tag{5.5}$$

The mechanical torque balancing equation can be written as (5.6)

$$\frac{J}{P/2}\frac{d\omega_r}{dt} = T_e - T_l \tag{5.6}$$

Where P= Induction motor stator poles

T_l=load torque in Nm

5.3 Virtual voltage vector generation for DIFPOEWIM drive

The 32-switching states of a single 2-level 5-leg inverter are categorized into large vectors ($0.6472V_{dc}$), medium vectors ($0.4V_{dc}$), small vectors ($0.2472V_{dc}$), and null vectors ($0V_{dc}$) in both the harmonic (xy) and fundamental (αβ) planes, as depicted in Figure 5.2. Notably, in Figure 5.2, it is observed that the large voltage vectors in the fundamental (αβ) plane appear as small vectors in the harmonic (xy) plane, and vice versa, with opposite directions. Similarly, the medium voltage vectors in the αβ plane are reflected as medium voltage vectors in the xy plane with the same direction, as illustrated in Figure 5.2. The xy plane components contribute to ohmic losses in the distributed winding machine, while the components in the αβ plane generate useful torque. Therefore, eliminating the xy plane components is crucial to prevent excessive power loss associated with these currents.

The elimination of xy plane components employs the volt-second balance method, as detailed in [38] by selecting a dwell time ratio of 0.6181 for the medium vector (e.g., *16*) and the small vector (e.g., *25*) in the xy plane, following the ratio of their magnitudes, a zero mean vector is achieved in the xy plane, as depicted in Figure 5.3(a). This strategy results in zero harmonic currents [38]. The corresponding voltage V_1 in the αβ plane, generated by switching states *25* and *16,* is calculated as per (5.7) and illustrated in Figure 5.3(a).

$$T_s V_1 = t_1 * 25 + t_2 * 16$$
$$V_1 = 0.553 V_{dc} \angle 0^0 \tag{5.7}$$

Where *16*=Medium vector=$0.4V_{dc}\angle 0^0$

25=Large vector=$0.642V_{dc}\angle 0^0$

t_1 =Dwell time of large vector=$0.618T_s$

t_2 =Dwell time medium vector=$0.382T_s$

T_s=Total sample time=$t1+t2$

By similar analysis of the volt-sec balance scheme, small virtual vectors V_{11} generated from the medium vector *16* and small vector *9* of the inverter as shown below (5.8).

$$T_s V_{11} = t_1 * 16 + t_2 * 9$$

$$V_{11} = 0.342 V_{dc}\angle 0^0 \quad (5.8)$$

Where *16*=Medium vector=$0.4V_{dc}\angle 0^0$

9=Small vector=$0.247V_{dc}\angle 0^0$

t_1 =Dwell time of large vector=$0.618T_s$

t_2 =Dwell time medium vector=$0.382T_s$

T_s=Total sample time=t_1+t_2

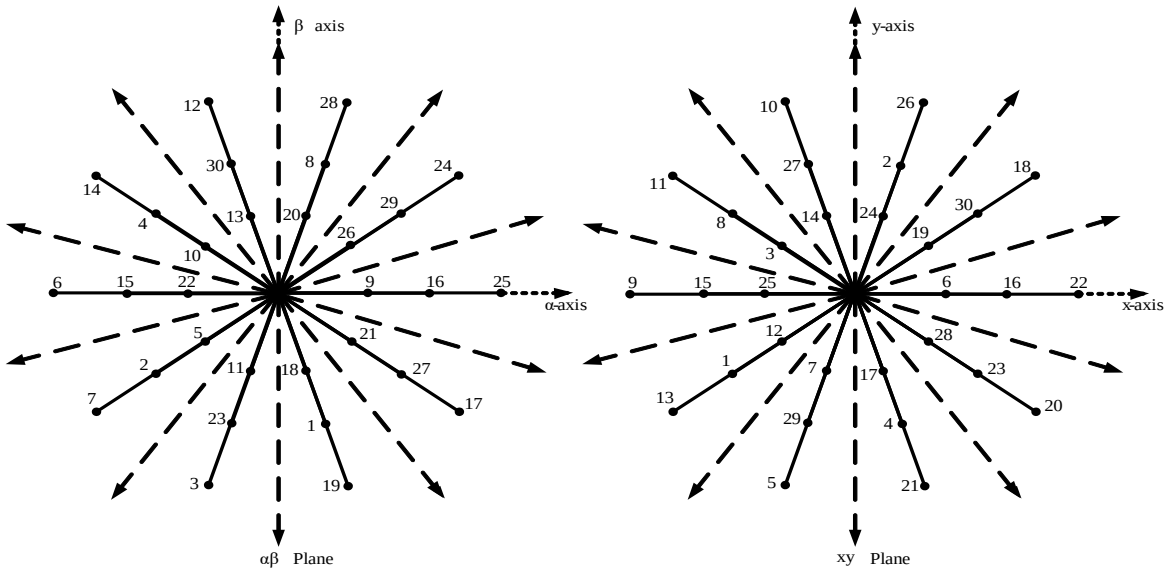

Figure 5.2 Switching vectors space location of 5-phase inverter in αβ plane and xy plane

As previously discussed, the deliberate computation of dwell periods for inverter switching states, aiming to nullify harmonic plane components, results in the creation of 10 large virtual voltage vectors (V_1 to V_{10}) and 10 small virtual voltage vectors (V_{11} to V_{20}) with magnitudes of $0.553V_{dc}$ and $0.342V_{dc}$, respectively, as illustrated in Figure 5.3(b).

The zero common mode voltage (CMV) in DIFPOEWIM prompts the utilization of a common DC bus for both inverters, eliminating the need for bulky isolation transformers typically employed to isolate DC supplies for each inverter.

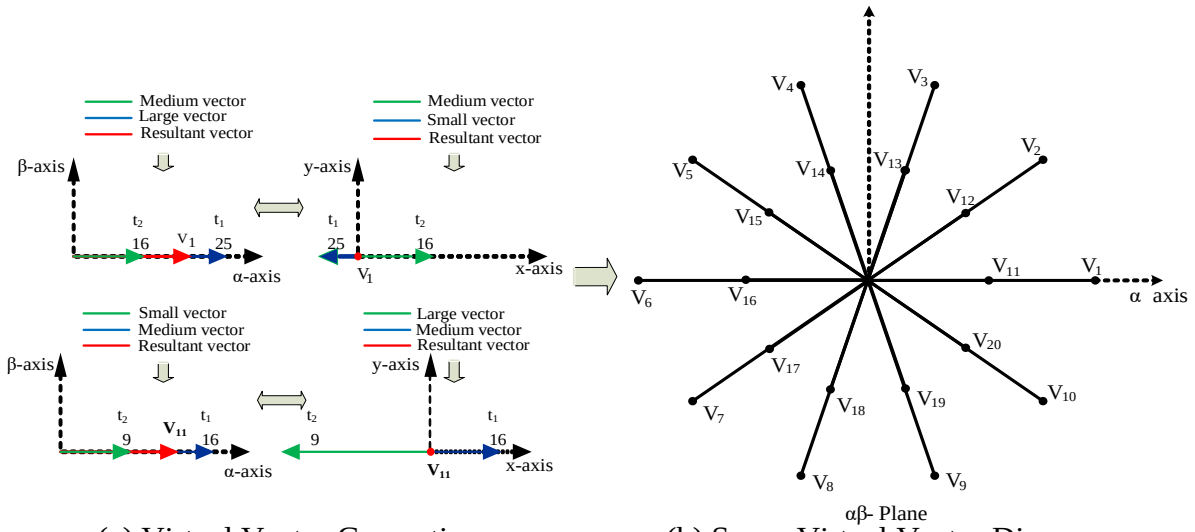

(a) Virtual Vector Generation (b) Space Virtual Vector Diagram

Figure 5.3 (a) Resultant virtual voltage vector V_1 and V_{11} generation in both αβ- plane and xy-plane (b) Virtual voltage vector space diagram in αβ- plane

The common mode voltage of inverter I and inverter II in a dual inverter fed 5-phase open-end winding induction motor can be expressed as below (5.9)

$$V_{cmvI} = \left(\frac{1}{5}\right) * (V_{a0} + V_{b0} + V_{c0} + V_{d0} + V_{e0})$$
$$V_{cmvII} = \left(\frac{1}{5}\right) * (V_{\acute{a}0} + V_{\acute{b}0} + V_{\acute{c}0} + V_{\acute{a}0} + V_{\acute{e}0}) \quad (5.9)$$

Where V_{a0}, V_{b0}, V_{c0}, V_{d0}, V_{e0}=Inverter I pole voltages $(V_{x0}=S_x*V_{dc}/2)$

$V_{a'0}$, $V_{b'0}$, $V_{c'0}$, $V_{d'0}$, $V_{e'0}$= Inverter II pole voltages $(V_{x'0}=S_{x'}*V_{dc}/2)$

S_x and $S_{x'}=0$ or 1; x=phase $a..e.$; x'=phase $a'..e'$.

The resultant CMV across the windings of a dual 5-leg inverter (DI) configuration can be expressed as (5.10).

$$V_{cmvDI} = V_{cmvI} - V_{cmvII} \quad (5.10)$$

When selecting switching vectors for inverter I and inverter II to form the combined vector in a dual inverter system, a phase difference of $n*2\pi/5$ $(n=1, ...,5)$ is maintained between the switching states of inverter I and inverter II. This ensures that both inverters generate equal common mode voltages ($V_{cmvI}=V_{cmvII}$), consequently leading to zero common mode voltage in the dual 5-leg inverter from (5.10). From the twenty active virtual voltage vectors for each inverter, a total of 30 voltage vectors are created in the dual inverter configuration, ensuring zero common mode voltage (CMV). These 30 vectors are categorized into medium (V_M), small (V_S), and large (V_L) vectors, as illustrated in Figure 5.4.

The vector V_{M1} is formed by combining inverter I vector V_1 and inverter II vector V_9, as shown in equation (5.11). Likewise, the V_{S1} vector is formed by combining inverter I vector V_{11} and inverter II vector V_{19}, as demonstrated in equation (5.12). Similarly, the V_{L1} vector is

created by combining inverter I vector V_1 and inverter II vector V_7, as expressed in equation (5.13).

$$V_{M1} = V_1 - V_9$$

$$V_{M1} = 0.553V_{dc}\angle 0 - 0.553V_{dc}\angle\left(\frac{9\pi}{5}\right) = 0.623V_{dc}\angle\left(\frac{3\pi}{10}\right) \quad (5.11)$$

$$V_{S1} = V_{11} - V_{19}$$

$$V_{S1} = 0.342V_{dc}\angle 0 - 0.342V_{dc}\angle\left(\frac{9\pi}{5}\right) = 0.385V_{dc}\angle\left(\frac{3\pi}{10}\right) \quad (5.12)$$

$$V_{L1} = V_1 - V_7$$

$$V_{L1} = 0.553V_{dc}\angle 0 - 0.553V_{dc}\angle\left(\frac{6\pi}{5}\right) = 1.05V_{dc}\angle\left(\frac{\pi}{10}\right) \quad (5.13)$$

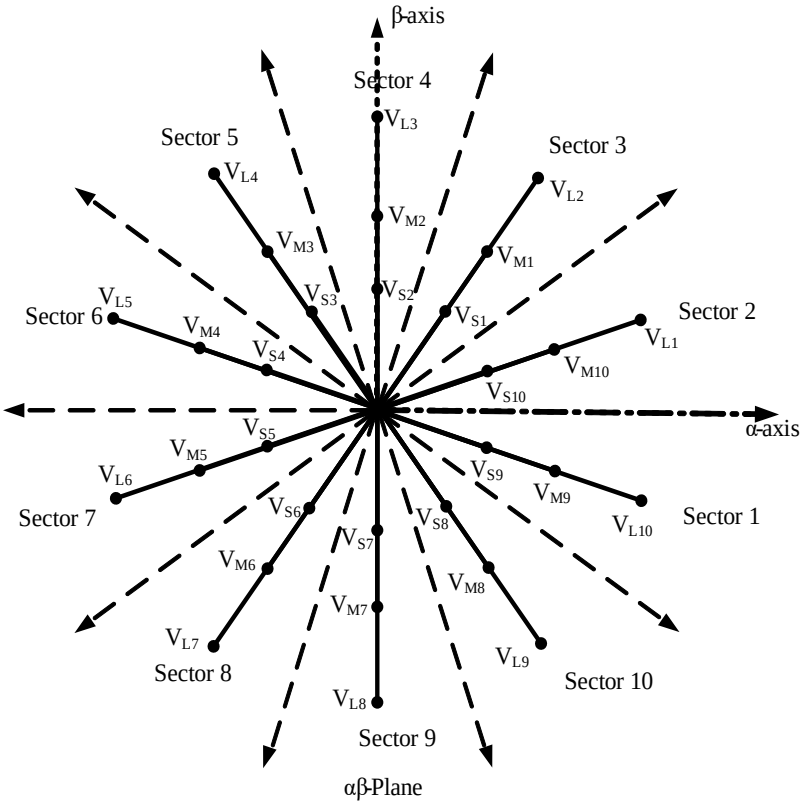

Figure 5.4 Space vector diagram of virtual voltage vectors for DI-FPOEWIM

5.4 Implementation of proposed DTC scheme in DIFPOEWIM

The conventional direct torque control (DTC) method [56] implemented in the dual inverter-fed five-phase open-end winding induction motor (FPOEWIM) employs a 3-level torque hysteresis controller utilizing only 10 large virtual voltage (V_L) vectors. However, this approach results in significant torque and flux ripples, as well as increased current harmonic distortion. Furthermore, it underutilizes the inherent potential of the 5-phase dual inverter configuration. To address these limitations, a 5-level DTC scheme was introduced, incorporating a total of 20 virtual voltage vectors (including both large V_L and medium V_M vectors) specifically designed for a five-phase dual inverter configuration [58]. Despite this

enhancement, the 5-level scheme still exhibits considerable harmonic current distortion and torque ripple. Both the proposed methods in [56] and [58] share a common challenge: they underutilize the full switching state possibilities offered by the dual inverter configuration.

The proposed DTC scheme for a 5-phase induction motor, driven by dual inverters, incorporates 30 voltage vectors to enable the implementation of a 7-level torque hysteresis controller. Specifically, during high-speed conditions (speed ≥ 300 rpm), the proposed DTC scheme utilizes all 30 voltage vectors shown in a lookup table (Table 5.1) with the 7-level torque controller to lessen torque ripple and decrease harmonic current distortion. Additionally, for low-speed operations (speed < 300 rpm), a separate 3-level torque hysteresis controller is employed along with another lookup table (Table 5.2), with the help of small voltage vectors. This approach is designed to further reduce both torque and flux ripples, while concurrently minimizing current harmonic distortion under low speeds. The comparison among the 3-level DTC [56], 5-level DTC [58] and the proposed DTC scheme involves same torque hysteresis controller bands (0.3 Nm or 10% of rated torque) and flux hysteresis controller bands (0.005 Wb or 4% of rated flux) for fair comparison. The sample time for all the DTC schemes is set at 100 μsec.

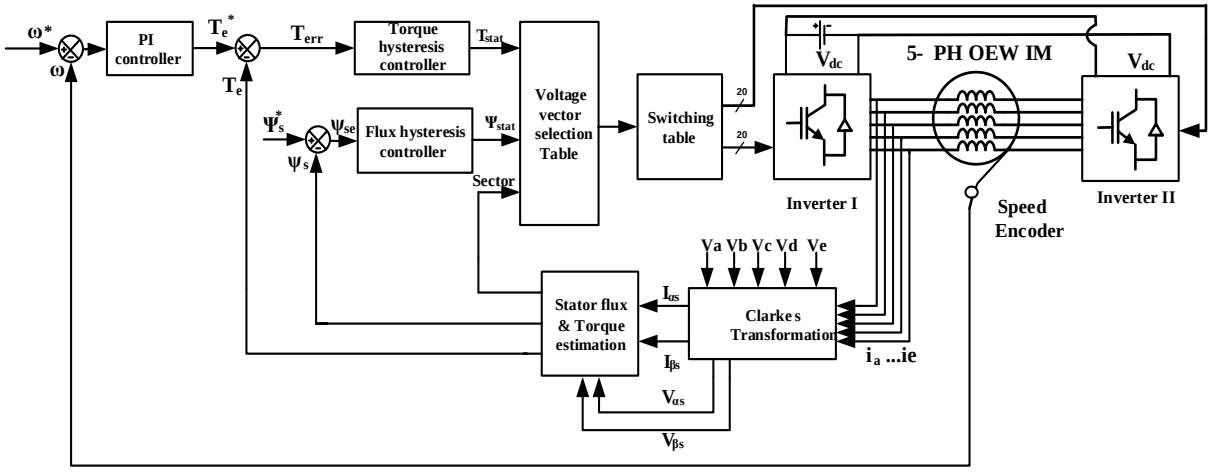

Figure 5.5 Block diagram representation of the DTC control of dual inverter-fed five-phase open-end winding Induction Motor

The block diagram illustrating the proposed direct torque control (DTC) method for the dual inverter-controlled five-phase open-end winding induction motor (FPOEWIM) is presented in Figure 5.5. The components include a speed Proportional-Integral (PI) controller, speed encoder, torque-flux estimation block, 7-level/3-level torque hysteresis controller, 2-level flux hysteresis controller, 2-level 5-leg inverters, and a five-phase open-end winding induction motor. In block diagram Figure 5.5, the speed error is processed through the PI

controller and generates a reference torque (T_e^*). The reference torque (T_e^*) and a reference flux (Ψ_s^*) are then compared with the actual torque and actual flux, resulting in torque error (T_{err}) and flux error (Ψ_{serr}). The suitable voltage vector is subsequently chosen based on these errors and sector information obtained from a lookup table to meet the required torque and flux.

In the direct torque control (DTC) scheme, the desired changes in torque (ΔT_e) and flux ($\Delta \Psi_s$) can be achieved by applying suitable voltage vectors within a sample period T_s. This process directly influences the flux, as described in equation (5.14), where the flux is affected by the applied voltage throughout T_s. Moreover, the torque primarily responds to changes in the stator flux angle w.r.t the rotor flux vector ($\Delta\theta$), as outlined in equation (5.15) and shown in Figure. 5.6.

$$\Delta \Psi_s = (V_s - R_s i_s)\Delta T_s \tag{5.14}$$

$$\Delta T_e = \frac{5}{2}\frac{P}{2}\frac{L_m}{L_r L_{ss}}(|\Psi_s + \Delta \Psi_s|)(|\Psi_r|)\, sin(\Delta\theta) \tag{5.15}$$

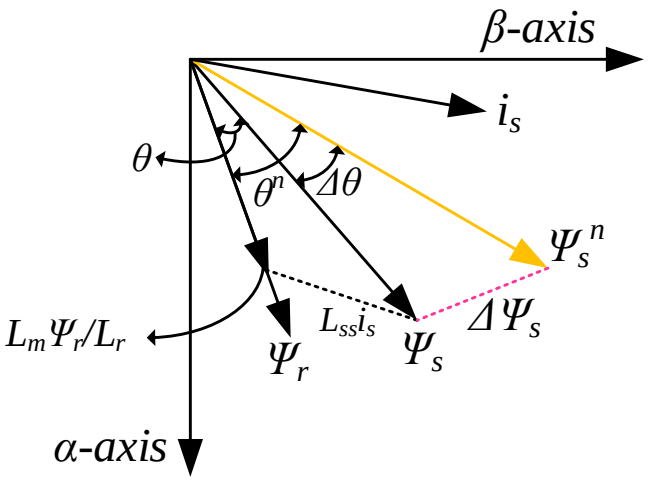

Figure 5.6 Phasor representation of basic DTC operation

The stator flux and electromagnetic torque are estimated from motor dynamic equations as shown below.

The stator voltage balancing equation can be written as (5.16)

$$V_s = I_s R_s + \frac{d\Psi_s}{dt} \tag{5.16}$$

Where V_s = stator phase voltage in volts

I_s= stator phase current in amperes

R_s=stator resistance in ohms

The estimation of stator flux (Ψ_s) can be done as shown in (5.17)

$$\Psi_s = \int (V_s - I_s R_s)\, dt \tag{5.17}$$

The estimation of electromagnetic torque (T_e) can be done as below (5.18)

$$T_e = \frac{5}{2}\frac{P}{2} imag(\Psi_s^* I_s) \quad (5.18)$$

Where *P*- Induction motor stator poles

In the proposed DTC control method of DIFPOEWIM, 30 virtual voltage vectors ($V_{L1}...V_{L10}$; $V_{M1}...V_{M10}$; $V_{S1}...V_{S10}$) and two null voltage vectors (V_0, V_{31}) are used to control the speed of the induction motor.

Table 5.1 Switching voltage vector selection table for high speeds

Ψ_{stat}	T_{stat}	Sector									
		1	2	3	4	5	6	7	8	9	10
1	3	V_{L2}	V_{L3}	V_{L4}	V_{L5}	V_{L6}	V_{L7}	V_{L8}	V_{L9}	V_{L10}	V_{L1}
1	2	V_{M1}	V_{M2}	V_{M3}	V_{M4}	V_{M5}	V_{M6}	V_{M7}	V_{M8}	V_{M9}	V_{M10}
1	1	V_{S1}	V_{S2}	V_{S3}	V_{S4}	V_{S5}	V_{S6}	V_{S7}	V_{S8}	V_{S9}	V_{S10}
1	0	Null									
1	-1	V_{S8}	V_{S9}	V_{S10}	V_{S1}	V_{S2}	V_{S3}	V_{S4}	V_{S5}	V_{S6}	V_{S7}
1	-2	V_{M8}	V_{M9}	V_{M10}	V_{M1}	V_{M2}	V_{M3}	V_{M4}	V_{M5}	V_{M6}	V_{M7}
1	-3	V_{L9}	V_{L10}	V_{L1}	V_{L2}	V_{L3}	V_{L4}	V_{L5}	V_{L6}	V_{L7}	V_{L8}
-1	3	V_{L4}	V_{L5}	V_{L6}	V_{L7}	V_{L8}	V_{L9}	V_{L10}	V_{L1}	V_{L2}	V_{L3}
-1	2	V_{M3}	V_{M4}	V_{M5}	V_{M6}	V_{M7}	V_{M8}	V_{M9}	V_{M10}	V_{M1}	V_{M2}
-1	1	V_{S3}	V_{S4}	V_{S5}	V_{S6}	V_{S7}	V_{S8}	V_{S9}	V_{S10}	V_{S1}	V_{S2}
-1	0	Null									
-1	-1	V_{S6}	V_{S7}	V_{S8}	V_{S9}	V_{S10}	V_{S1}	V_{S2}	V_{S3}	V_{S4}	V_{S5}
-1	-2	V_{M6}	V_{M7}	V_{M8}	V_{M9}	V_{M10}	V_{M1}	V_{M2}	V_{M3}	V_{M4}	V_{M5}
-1	-3	V_{L7}	V_{L8}	V_{L9}	V_{L10}	V_{L1}	V_{L2}	V_{L3}	V_{L4}	V_{L5}	V_{L6}

Table 5.2 Switching voltage vector selection table for low speeds

Ψ_{stat}	T_{stat}	Sector									
		1	2	3	4	5	6	7	8	9	10
1	1	V_{S1}	V_{S2}	V_{S3}	V_{S4}	V_{S5}	V_{S6}	V_{S7}	V_{S8}	V_{S9}	V_{S10}
1	0	Null									
1	-1	V_{S8}	V_{S9}	V_{S10}	V_{S1}	V_{S2}	V_{S3}	V_{S4}	V_{S5}	V_{S6}	V_{S7}
-1	1	V_{S3}	V_{S4}	V_{S5}	V_{S6}	V_{S7}	V_{S8}	V_{S9}	V_{S10}	V_{S1}	V_{S2}
-1	0	Null									
-1	-1	V_{S6}	V_{S7}	V_{S8}	V_{S9}	V_{S10}	V_{S1}	V_{S2}	V_{S3}	V_{S4}	V_{S5}

The 7-level torque controller's upper band and lower band are divided into three parts according to the vector magnitude ratio below

T_{stat}=+3 for T_{err}> +0.3

T_{stat} =+2 for T_{err}< +0.3 & T_{err}> +0.18

T_{stat} =+1 for T_{err}< +0.18 & T_{err}> +0.11

T_{stat} =0 for T_{err}< +0.11 & T_{err}> -0.11

T_{stat} =-1 for T_{err}< -0.11 & T_{err}> -0.18

T_{stat} =-2 for T_{err}< -0.18 & T_{err}> -0.3

T_{stat} =-3 for T_{err}< -0.3

Where T_{err}= torque error= T_e^*-T_e

T_{stat}=torque controller output status

Upper/lower hysteresis band =0.3 Nm

The 2-level flux controller band is divided into the lower band and the upper band as shown below

Ψ_{stat}=+1 for Ψ_{serr}>0.005

Ψ_{stat}=-1 for Ψ_{serr}<-0.005

Where Ψ_{serr}=flux error= Ψ_s^*- Ψ_{se}

Ψ_{stat}=flux controller output status

Upper/lower hysteresis band=0.005Wb

With the information of torque controller status, flux controller status, and flux vector sector information; the suitable switching vectors are chosen as shown in lookup Table 5.1 and Table 5.2.

5.5 Experimental Result Analysis

The proposed direct torque control (DTC) scheme driving a dual inverter-fed five-phase open-end winding induction motor (DIFPOEWIM) is experimentally tested and compared with the existing DTC schemes [56],[58] on DIFPOEWIM through valid experimental findings. The hardware experimental prototype is shown in Appendix I. In the experimental work, the proposed and existing DTC schemes are implemented with the help of the dSPACE 1202 controller using real-time interfacing with MATLAB/Simulink software. The motor drive being tested comprises a 1HP 5-phase open-end winding induction motor with a coupled 1 HP DC generator. The DC generator is loaded with resistive lamp loads. The test setup includes two 2-level 5-leg IGBT-based inverter modules with an inbuilt gate driver circuit, along with a rectifier unit. These inverter module switches are triggered by gate signals from the dSPACE controller. The 1024 pulses per rotation (PPR) speed encoder is used for accurate speed tracking and this speed information is given to the control circuit with an encoder port on the dSPACE controller. The 5-phase currents and DC link voltages are sensed using LEM make LA-25P current sensors and LV-25P voltage sensors respectively. The sensed signals are converted into to digital manner through onboard ADCs on the dSPACE controller. Both existing DTC control methods [56],[58] and the proposed DTC control method are executed with the same torque hysteresis band (HB_{Te}) of 10% rated torque and flux hysteresis band ($HB_{\Psi e}$) of 4% rated flux with the same sampling time of 100 µsec for fair comparison of experimental findings. The effectiveness of the proposed DTC control scheme over classical DTC schemes [56], [58] is tested for various speeds and loading conditions. The transient behavior of the drive is also tested for different DTC schemes with step load disturbance and step speed disturbances.

5.5.1 Steady-state performance analysis

The steady-state performance evaluation of the FPOEWIM is examined in terms of flux ripple, torque ripple, and current harmonic distortion for both high speeds and low speeds under no load and loading conditions for three control methods: 3-level DTC [56], 5-level DTC [58] and the proposed DTC control methods. This comprehensive analysis aims to assess the superiority of the modified lookup table-based proposed DTC method.

The computation of average torque and flux ripples is done by equation (5.19), utilizing real-time data points of torque pattern and flux pattern from the steady-state hardware results for all three control schemes. The average torque ripple and flux ripple are calculated for 3-level DTC, 5-level DTC, and proposed DTC schemes based on a dataset consisting of 10000 samples per second (*N/sec*).

$$Torque/flux_{ripple} = \sqrt{\frac{1}{N}\sum_{i=1}^{N}\left(X(i) - X_{avg}\right)^2} \tag{5.19}$$

Where $X(i)$ =torque/flux at the i^{th} sample

X_{avg}=average torque/flux over N samples

In Figure 5.7, the torque and flux patterns under no load are illustrated at speeds (I) 1400 rpm and (II) 100 rpm. Notably, I (a) and II (a) for the 3-level DTC exhibit flux ripples of 0.0066 Wb and 0.0047 Wb, along with torque ripples of 0.183 Nm and 0.154 Nm, respectively, at the corresponding speeds. Likewise, I (b) and II (b) for the 5-level DTC showcase flux ripples of 0.005 Wb and 0.00452 Wb, as well as torque ripples of 0.112 Nm and 0.106 Nm, respectively, for speeds of 1400 rpm and 100 rpm.

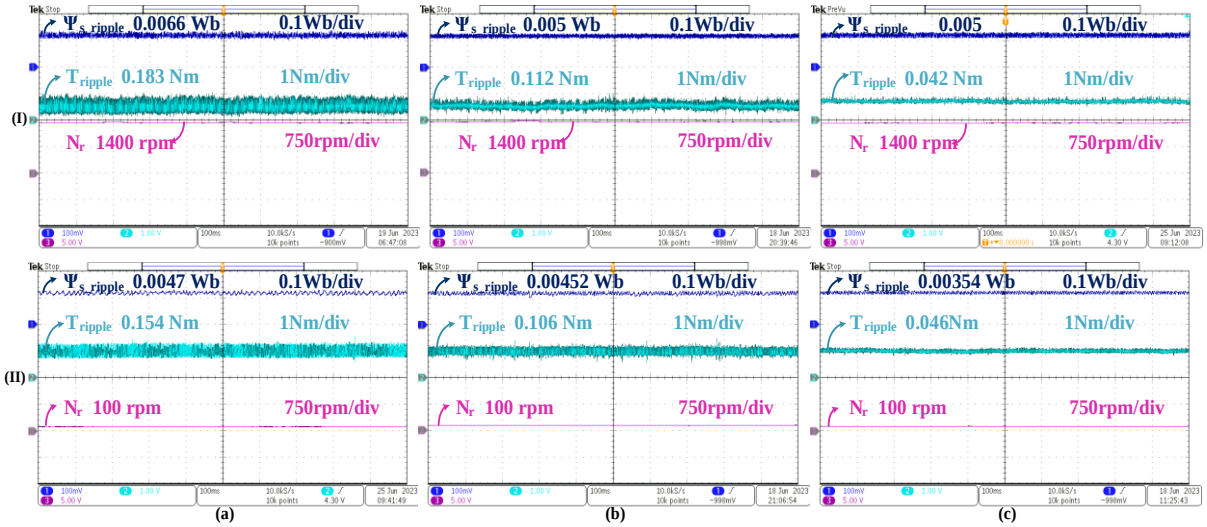

Figure 5.7 Flux, torque pattern at no load for a speed of (I) 1400 rpm, (II) 100 rpm in (a) 3-level DTC, (b) 5-level DTC, (c) proposed DTC methods

In contrast, the proposed DTC control scheme, represented by I (c) and II (c), achieves a notable reduction in flux ripple to 0.005 Wb and 0.00354 Wb, torque ripples of 0.042 Nm and 0.046 Nm, respectively, at the corresponding speeds of 1400 rpm and 100 rpm.

In response to an applied load of 2 Nm, Figure 5.8 depicts the torque and flux patterns at speeds (I) 1400 rpm and (II) 100 rpm for (a) 3-level DTC [56], (b) 5-level DTC [58], and (c) the proposed DTC methods. In I (a) and II (a), the 3-level DTC scheme exhibits flux ripples of 0.0062 Wb and 0.00445 Wb, and torque ripples of 0.161 Nm and 0.159 Nm, respectively, corresponding to speeds of 1400 rpm and 100 rpm. Similarly, I (b) and II (b) for the 5-level DTC scheme show flux ripples of 0.0053 Wb and 0.00443 Wb, with torque ripples of 0.124 Nm and 0.106 Nm, respectively, at speeds of 1400 rpm and 100 rpm. Conversely, the proposed DTC scheme illustrated in I (c) and II (c) produces flux ripples of 0.0053 Wb and 0.0037 Wb, and torque ripples of 0.05 Nm and 0.044 Nm, respectively, at speeds of 1400 rpm and 100 rpm under the applied load of 2 Nm.

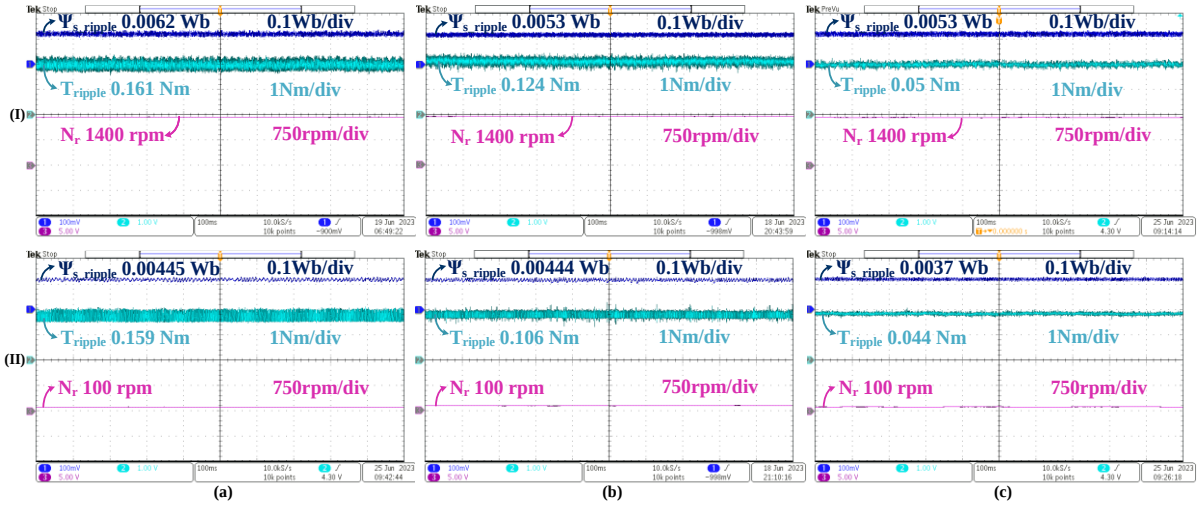

Figure 5.8 Flux, torque pattern under the load of 2 Nm for a speed of (I) 1400 rpm, (II) 100 rpm in (a) 3-level DTC, (b) 5-level DTC, (c) proposed DTC methods

In Figure 5.9, the bar graph illustrates torque ripple at various speeds under a 2 Nm load and no load for 3-level DTC [56] 5-level DTC [58] and the proposed DTC scheme. Notably, the suggested DTC control method markedly reduces torque ripple by employing a 7-level torque hysteresis controller at high speeds and a 3-level torque controller at low speeds with only small vectors. The proposed DTC contributes to the substantial improvement observed in minimizing torque ripple across a range of speeds and loading conditions, as highlighted in the graphical representation.

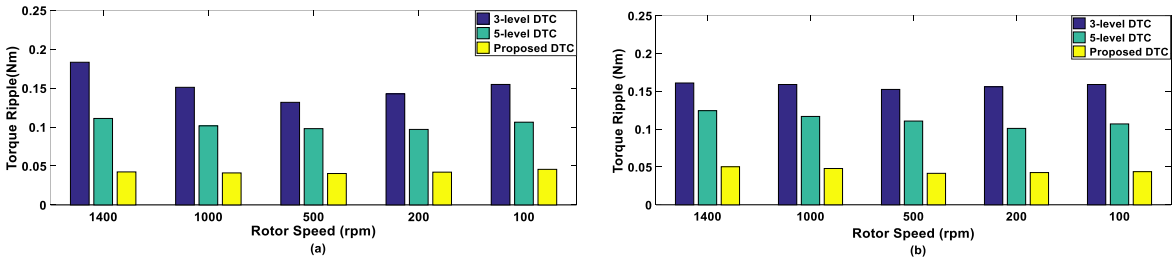

Figure 5.9 Torque ripple analysis for different rotor speeds at (a) no load (b) load of 2 Nm for 3-level DTC, 5-level DTC, and proposed DTC scheme

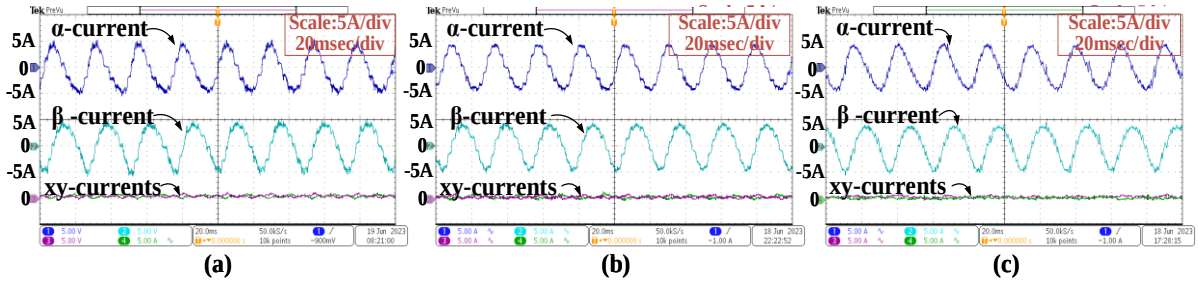

Figure 5.10 Fundamental plane (α,β) currents and harmonic plane (x,y) currents for (a) 3-level DTC, (b) 5-level DTC, (c) proposed DTC scheme

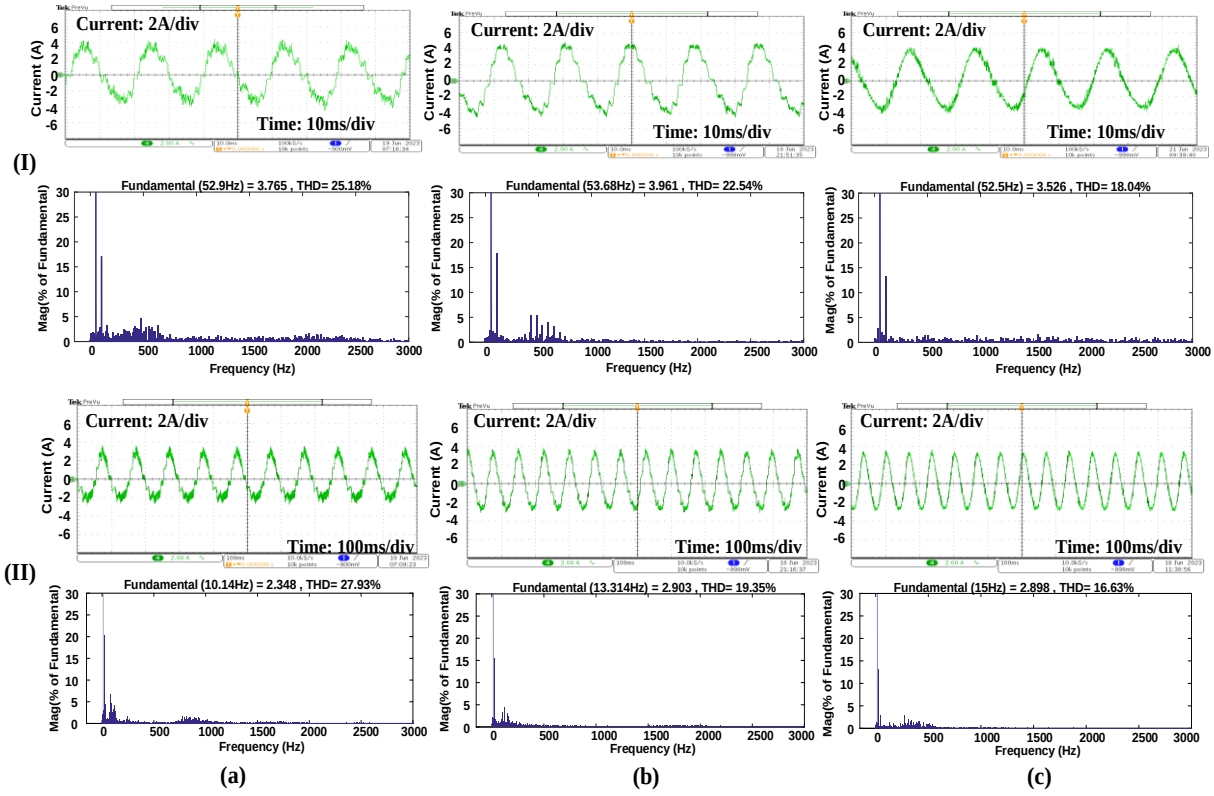

Figure 5.11 Current waveform and %THD for a speed of (I) 1400 rpm, (II) 100 rpm at load 2 Nm for (a) 3-level DTC, (b) 5-level DTC, (c) proposed DTC schemes

Figure 5.10 depicts the fundamental currents (αβ-currents) and xy-plane currents (xy-currents) for the 3-level DTC, 5-level DTC, and the proposed DTC scheme. It is notable that all

DTC schemes effectively reduce the xy currents to zero. Upon closer inspection of Figure 5.10, it is evident that the proposed DTC scheme exhibits a better current profile when compared to existing DTC methods due to an increased number of vectors.

In Figure 5.11, the phase current waveforms and their %total harmonic distortion (%THD) are shown at speeds (I) 1400 rpm, and (II) 100 rpm for (a) 3-level DTC, (b) 5-level DTC and (c) the proposed DTC method under a 2 Nm load. Examining I (a), and II (a), the 3-level DTC exhibits %THD values of 25.18%, and 27.93%, respectively, at speeds of 1400 rpm and 100 rpm. Similarly, in I (b), and II (b), the 5-level DTC produces %THD values of 22.54% and 19.35% for the corresponding speeds. In contrast, the proposed DTC scheme, as shown in I (c), and II (c) demonstrates %THD values of 18.04%, and 16.63%, respectively, for speeds of 1400 rpm, and 100 rpm under the 2 Nm load. Figure. 5.12 further presents a bar graph depicting the phase current harmonic distortion at various rotor speeds under an applied load of 2 Nm. It is evident from the graph that the proposed DTC control method consistently exhibits reduced harmonic current distortion when compared with the 3-level DTC [56] and 5-level DTC [58] methods for various rotor speeds. This signifies a notable improvement in the current quality achieved by the proposed control approach.

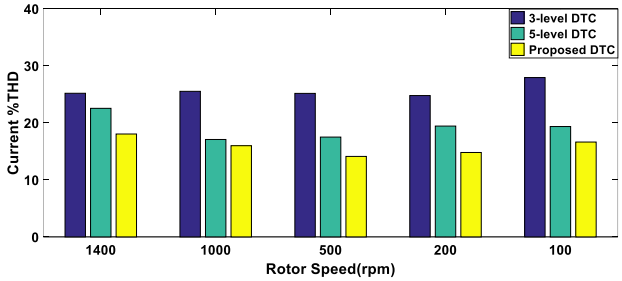

Figure 5.12 Current %THD analysis for various speeds under 2 Nm load for 3-level DTC, 5-level DTC, proposed DTC scheme

Table 5.3 Torque ripple and %THD comparison table for 3-level DTC, 5-level DTC, and proposed a DTC scheme for various speeds

Scheme	1400 rpm		1000 rpm		500 rpm		100 rpm	
	T_{ripple} (Nm)	THD (%)	T_{ripple} (Nm)	THD (%)	T_{ripple} (Nm)	THD (%)	T_{ripple} (Nm)	THD (%)
3-level DTC scheme	0.161	25.18	0.159	25.52	0.1525	25.16	0.159	27.93
5-level DTC scheme	0.1244	22.54	0.1168	19.85	0.1107	17.50	0.1069	19.35
Proposed DTC scheme	0.0503	18.04	0.048	15.99	0.0416	14.11	0.0438	16.63
% ripple, %THD reduction w.r.t 3-level DTC scheme	**68.7%**	**28.3%**	**68.5%**	**37.3%**	**72.7%**	**43.9%**	**72.3%**	**40.4%**
% ripple, %THD reduction w.r.t 5-level DTC scheme	**59.5%**	**19.9%**	**58.9%**	**19.44%**	**62.4%**	**19.3%**	**58.8%**	**14.0%**

From the analysis of Figure 5.7-Figure 5.12, and the results comparison Table 5.3, it is evident that the proposed direct torque control (DTC) scheme for a DIFPOEWIM outperforms the existing DTC techniques [56], [58]. The introduction of a 7-level torque controller in the proposed DTC scheme leads to a significant reduction in the current % total harmonic distortion (%THD) and torque ripple. Furthermore, the utilization of a 3-level torque controller with small vectors and null vectors in the proposed scheme contributes to a simultaneous reduction in both torque and flux ripple, along with a notable decrease in current harmonic distortion compared to existing methods. These findings underscore the superior performance of the proposed DTC approach in optimizing the steady-state operation of the DI-FPOEWIM.

5.5.2 Dynamic Performance Analysis

The dynamic performance of the proposed DTC control scheme is tested and compared with the classical DTC schemes [56], [58] to know the dynamic behavior of the proposed method for speed and load disturbances. The implementation of the DTC control algorithm in the 3-level DTC, 5-level DTC, and proposed DTC scheme implemented by the same hysteresis band, DC voltage source, and sampling time. This uniformity makes, these three methods showcase nearly identical dynamics in the induction motor as discussed below

In Figure 5.13, it displays the speed reversal disturbance from -500 rpm to 500 rpm for three control methods on a DI-FPOEWIM: (a) 3-level DTC, (b) 5-level DTC, and (c) the proposed DTC scheme. It's noticeable that the proposed method exhibits a speed reversal response similar to existing DTC control techniques. Likewise, Figure 5.14 illustrates speed disturbances from 1000 rpm to 1400 rpm for (a) 3-level DTC, (b) 5-level DTC, and (c) the proposed DTC method and it is seen that the proposed DTC scheme shows a response similar to other existing DTC methods [56] and [58].

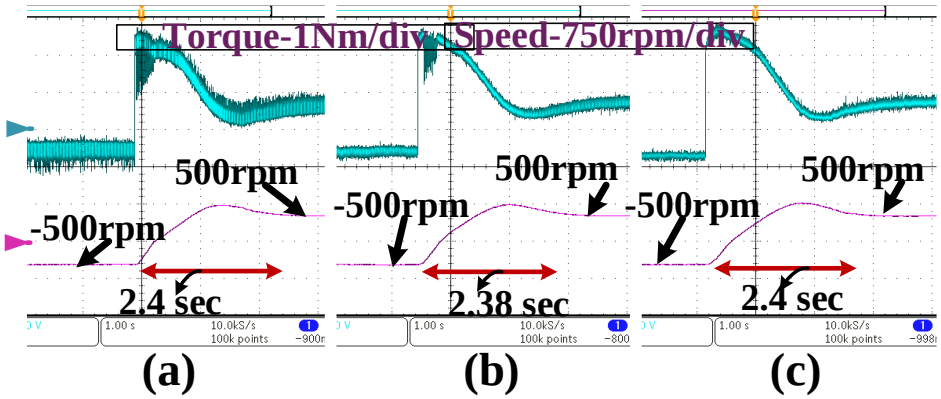

Figure 5.13 Step speed reversal response from -500 rpm to 500 rpm at no load (a)3-level DTC (b) 5-level DTC (c) proposed DTC schemes

Similarly, the inspection of torque dynamics involves introducing load disturbances, from no load to a 2 Nm load, for different control methods of the dual inverter-fed 5-phase induction motor, as depicted in Figure 5.15: (a) 3-level DTC, (b) 5-level DTC, and (c) the proposed DTC scheme. It's evident from Figure 5.13-Figure 5.15, that the proposed DTC scheme exhibits the same response for speed and load disturbances as that of existing DTC schemes mentioned in references [56] and [58]

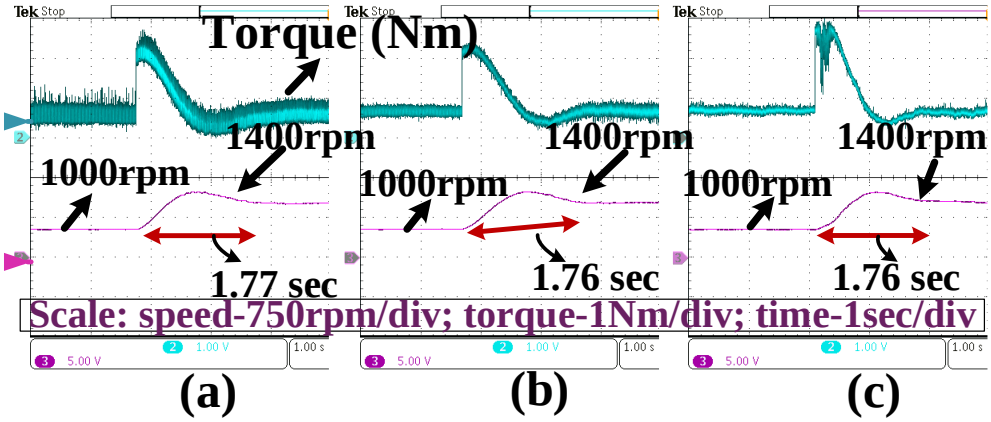

Figure 5.14 Speed response from 1000 rpm to 1400 rpm at no load (a)3-level DTC (b) 5-level DTC (c) proposed DTC schemes

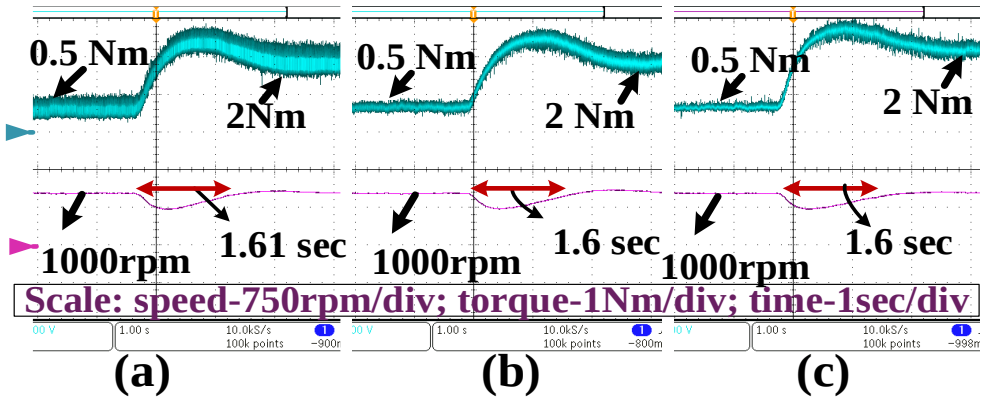

Figure 5.15 Step load disturbance response from no load to 2 Nm at 1000 rpm (a)3-level DTC (b) 5-level DTC (c) proposed DTC schemes

Table 5.4 Five-phase open-end winding induction motor (FPOEWIM) parameters

Parameter	Value	Parameter	Value	Parameter	Value
Power Rating	1 HP	Stator resistance (Rs)	1.05 Ω	Rotor resistance (Rr)	1.42 Ω
Stator inductance (Ls))	90.73mH	Mutual inductance (Lm)	84.73mH	Rotor inductance (Lr)	90.73mH
No. of Poles (P)	4	Inertia constant (J)	0.148Kg-m^2	Rated Speed	1400 rpm
DC voltage (V_{dc})	110V	Sample time (T_S)	100e-6 sec	PI controller K_p, K_i	0.02, 0.005

5.6 Summary and Conclusions

In this chapter, a modified lookup table-based DTC scheme is implemented on DIFPOEWIM for the reduction of torque ripple, flux ripple, and current harmonic distortion without disturbing the dynamic performance of the drive. The proposed direct torque control (DTC) method uses 30 voltage vectors instead of 10 voltage vectors or 20 voltage vectors in existing DTC schemes for DIFPOEWIM. The torque ripple and current distortion are reduced for a DIFPOEWIM by employing the 7-level torque hysteresis controller with all 30 voltage vectors at high speeds. Also, a 3-level torque hysteresis controller is implemented with 10 small voltage vectors at low speeds to further minimize flux ripple, and torque ripple along current distortion. The effectiveness of the proposed DTC scheme is thoroughly tested with experimental validations across various speeds and loads for improved steady-state performance, notably reduced current harmonic distortion and torque ripple. The proposed control scheme produces zero common mode voltage which enables the utilization of a single common DC bus without requiring an isolation transformer, while concurrently eliminating harmonic plane (xy-plane) components through a volt-sec balance scheme. The proposed control method of a 5-phase induction motor is particularly well-suited for applications in high torque density industrial drives, electric aircraft, and electric vehicles, showcasing superior reliability, increased torque density, efficient space utilization, lower voltage rating, and minimized torque and flux ripples.

Chapter 6

Conclusions and Future Scope

Chapter 6

Conclusion and Future Scope

This research explores various modified DTC control strategies applied to a VSI-fed 5-phase induction motor drive, with a primary emphasis on enhancing the drive's steady-state performance. The key objectives involve mitigating torque and flux ripples, reducing current harmonic distortion, optimizing switching frequencies, and addressing common-mode voltage issues. Additionally, the integration of a dual inverter configuration in the OEW-FPIM further contributes to improving the steady-state characteristics of the drive.

7.1 Conclusions

A modified DTC technique is implemented with a constant switching torque controller for improving the steady-state performance of the 5-phase induction motor. The proposed scheme controls the duration of active voltage vectors depending on the motor speed. The precise variation of duty of active vectors will give the reduced torque ripple with lowering speeds. The torque ripples have been reduced by almost 15% under high speed and 40% under low speeds when compared to conventional DTC. The harmonic current %THD is reduced by 10% under high speed and 30% under low speeds compared to conventional DTC. The switching frequency is maintained nearly constant compared to the classical DTC method.

A DTC control method with a proposed constant switching flux controller in place conventional hysteresis flux controller is used to reduce average flux ripple and current harmonic distortion with virtual voltage vectors such that the harmonic plane components will become zero. The proposed CSF controller-based DTC (CSFHTC-DTC) reduces the flux ripple by 30% and 39% under high speed and low speed respectively when compared with the classical DTC method. The current %THD is reduced by 30% w.r.t classical method. The proposed CSFHTC-DTC method won’t disturb the machine dynamics as the same hysteresis torque controller was used.

The modified DTC control with the proposed CST controller and CSF controller is introduced to further improve torque, flux, and current profiles and maintain fast dynamics as that of classical DTC schemes. The virtual voltage vectors introduced in this method make harmonic plane components zero. The torque error and flux error status are forced to follow triangular carrier waves and the duration of active vectors is controlled with CST and CSF

controller duty signals. The proposed CST and CSF-based DTC reduces both torque ripple and flux ripple when compared with the existing classical DTC schemes.

A modified slip speed control based direct flux control (SSC-DFC) is implemented to control the five-phase induction motor to improve the flux profile, torque profile, and current pattern with constant switching frequency. The proposed method uses the voltage error status for every sample and selects a suitable voltage vector to track the reference vector. Due to the precise flux control method, the flux ripple and current %THD are greatly reduced when compared with the existing DTC schemes. The proposed SSC-DFC method reduced the torque ripple by 4.5% and 28% w.r.t C-DTC, 1.4%, 42% w.r.t M-DTC under high speeds and low speeds respectively. The average flux ripple is reduced by 37.5% and 60% w.r.t C-DTC, and 16.65%, 45% w.r.t M-DTC under high speeds and low speeds respectively. The current %THD reduced by 46% and 44% w.r.t C-DTC and 40.9%, 41% w.r.t M-DTC method under high speeds and low speeds respectively. The proposed method also simplifies the lookup table.

A modified lookup table-based DTC of a dual inverter-controlled 5-phase open-end winding induction motor is presented to improve average flux ripple and torque ripple and current %THD without disturbing dynamics. The proposed method uses a 7-level torque controller and a 3-level torque controller under high speeds and low speeds respectively. The proposed method also eliminates the common mode voltage by selecting the $n*2\pi/5$ phase difference between two inverter switching states. The proposed method avoids a bulky isolation transformer and uses a single DC source by proper switching action to make zero common mode voltage. The proposed method uses the virtual voltage vector concept to make harmonic plane components zero. The proposed method reduces the torque ripple by 62.5% and 59.6% respectively under no load and load cases for 1400 rpm when compared with the 5-level DTC of DI-FPOEWIM. The proposed DTC method reduces the current %THD by 20% and 14% under high speeds and low speeds respectively w.r.t 5-level DTC method.

7.2 Future scope

In this work, the modified DTC technique is presented on a VSI-fed 5-phase induction motor. Based on the proposed DTC schemes, the future scope of work can be identified and presented below:

1. The proposed CST-DTC and CSTF-DTC methods can be extended for multi-level torque controller-based DTC techniques with multiple levels of carrier waves

2. The proposed CST-DTC and CSTF-DTC methods can also be extended for multi-level inverter-controlled 5-phase induction motor or multi-phase induction motor
3. The proposed CST-DTC and CSTF-DTC methods can be extended for dual inverter-controlled multi-phase induction motors with multiple carrier signals.
4. The proposed SSC-DFC schemes can be extended to dual inverter-controlled multi-phase induction motors and multi-level inverter-controlled induction motors
5. The proposed DTC technique can be extended for a single DC source fed dual voltage source inverter controlled 5-phase open-end winding induction motor with appropriate switching state selection such that the common mode voltage zero
6. The proposed DTC control schemes in single DC-fed dual inverter controlled 5-phase induction motor can be applied for multi-level dual inverter open-end winding induction motors with different DC bus voltages

Publications

Journals Published

1. V. S. Reddy and S. Devabhaktuni, "Enhanced Low-Speed characteristics with Constant Switching Torque Controller-based DTC Technique of Five-Phase Induction Motor Drive with FOPI Control," in IEEE Transactions on Industrial Electronics, doi: 10.1109/TIE.2022.3227275.
2. V. s. r. Chagam reddy and S. Devabhaktuni, "Reduction of Stator Flux Ripple and Current Harmonic Distortion using Constant Switching Flux Controller-based DTC of Five-Phase Induction Motor," in IEEE Latin America Transactions, vol. 21, no. 8, pp. 915-924, Aug. 2023, doi: 10.1109/TLA.2023.10246341.
3. V. S. Reddy Chagam and S. Devabhaktuni, "An Isolation Transformer-less Single DC Source fed Dual 5-leg Inverter Controlled 5-Phase Induction Motor with Modified Direct Torque Control," in IEEE Latin America Transactions, vol. 22, no. 3, pp. 229-239, March 2024, doi: 10.1109/TLA.2024.10431418.

Conferences

1. V. S. Reddy C and S. Devabhaktuni, "Improved Low-Speed Performance of DTC controller-based Dual Voltage Source Inverter fed Five-Phase OEW Induction Motor," 2022 IEEE International Conference on Power Electronics, Drives and Energy Systems (PEDES), Jaipur, India, 2022, pp. 1-4, doi: 10.1109/PEDES56012.2022.10080521.

Bibliography

[1] Haitham Abu Rub, Atif Iqbal, Jaroslaw Guzinski, “High Performance Control of AC Drives with Matlab/Simulink Models,” Wiley, 2012.

[2] Kim S. H, “Electric Motor Control,” Elsevier.

[3] Al-Bahadly, Ibrahim. (2007). Energy Saving with Variable Speed Drives in Industry Applications.

[4] Hashemnia, Mohammad Naser & Asaei, Behzad. (2008). Comparative study of using different electric motors in the electric vehicles. 1 - 5. 10.1109/ICELMACH.2008.4800157.

[5] K. Matsuse and D. Matsuhashi, "New technical trends on adjustable speed AC motor drives," in Chinese Journal of Electrical Engineering, vol. 3, no. 1, pp. 1-9, 2017, doi: 10.23919/CJEE.2017.7961316.

[6] Wang, Fengxiang & Zhang, Zhenbin & Mei, Xuezhu & Rodriguez, Jose & Kennel, Ralph. (2018). Advanced Control Strategies of Induction Machine: Field Oriented Control, Direct Torque Control, and Model Predictive Control. Energies. 11. 10.3390/en11010120.

[7] M. Mengoni, L. Zarri, A. Tani, L. Parsa, G. Serra, and D. Casadei, "High-Torque-Density Control of Multiphase Induction Motor Drives Operating Over a Wide Speed Range," in IEEE Transactions on Industrial Electronics, vol. 62, no. 2, pp. 814-825, Feb. 2015, doi: 10.1109/TIE.2014.2334662.

[8] A. Tani, M. Mengoni, L. Zarri, G. Serra and D. Casadei, "Control of Multiphase Induction Motors With an Odd Number of Phases Under Open-Circuit Phase Faults," in IEEE Transactions on Power Electronics, vol. 27, no. 2, pp. 565-577, Feb. 2012, doi: 10.1109/TPEL.2011.2140334.

[9] S. Williamson and S. Smith, "Pulsating torque and losses in multiphase induction machines," Conference Record of the 2001 IEEE Industry Applications Conference. 36th IAS Annual Meeting (Cat. No.01CH37248), Chicago, IL, USA, 2001, pp. 1155-1162 vol.2, doi: 10.1109/IAS.2001.955635.

[10] A. Mohammadpour, S. Sadeghi and L. Parsa, "A Generalized Fault-Tolerant Control Strategy for Five-Phase PM Motor Drives Considering Star, Pentagon, and Pentacle Connections of Stator Windings," in IEEE Transactions on Industrial Electronics, vol. 61, no. 1, pp. 63-75, Jan. 2014, doi: 10.1109/TIE.2013.2247011

[11] Frikha, M.A.; Croonen, J.; Deepak, K.; Benômar, Y.; El Baghdadi, M.; Hegazy, O. Multiphase Motors and Drive Systems for Electric Vehicle Powertrains: State of the Art Analysis and Future Trends. Energies 2023, 16, 768. https://doi.org/10.3390/en16020768

[12] N. Bianchi, S. Bolognani and M. Dai Pre, "Strategies for the Fault-Tolerant Current Control of a Five-Phase Permanent-Magnet Motor," in IEEE Transactions on Industry Applications, vol. 43, no. 4, pp. 960-970, July-aug. 2007, doi: 10.1109/TIA.2007.900445.

[13] Luis A. Pereira, Sergio Haffner and Luis F. A. Pereira “Performance comparison of five phase and three phase induction machines under steady state including losses and saturation”, IEEE 39th annual conference of the Industrial Electronics Society, IECON, November 2013, Vienna, Austria.

[14] E. Levi, R. Bojoi, F. Profumo, H. Toliyat, and S. Williamson, “Multiphase induction motor drives - a technology status review,” Electric Power Applications, IET, vol. 1, no. 4, pp. 489–516, July 2007.

[15] A. Baltatanu and M. -L. Florea, "Multiphase machines used in electric vehicles propulsion," Proceedings of the International Conference on ELECTRONICS, COMPUTERS and ARTIFICIAL INTELLIGENCE - ECAI-2013, 2013, pp. 1-6, doi: 10.1109/ECAI.2013.6636204.

[16] P. de Silva, J. Fletcher, and B. Williams, “Design of a five-phase induction motor using flux distribution optimization,” in Power Electronics, Machines and Drives, 2006. PEMD2006

[17] White, D.C. and Woodson, H.H. (1959) Electromechanical Energy Conversion. John Wiley & Sons, New York.

[18] H. Abu-Rub, A. Iqbal and J. Guzinski, High Performance Control of Electric drives with MATLAB/Simulink Models, New Jersey:John Wiley & Sons, Ltd., pp. 293-359, 2012.

[19] R. Bharti, M. Kumar and B. M. Prasad, "V/F Control of Three Phase Induction Motor," 2019 International Conference on Vision Towards Emerging Trends in Communication and Networking (ViTECoN), Vellore, India, 2019, pp. 1-4, doi: 10.1109/ViTECoN.2019.8899420.

[20] E. Levi, "Multiphase Electric Machines for Variable-Speed Applications," in IEEE Transactions on Industrial Electronics, vol. 55, no. 5, pp. 1893-1909, May 2008, doi: 10.1109/TIE.2008.918488.

[21] F. Barrero and M. J. Duran, "Recent Advances in the Design, Modeling, and Control of Multiphase Machines—Part I," in IEEE Transactions on Industrial Electronics, vol. 63, no. 1, pp. 449-458, Jan. 2016, doi: 10.1109/TIE.2015.2447733.

[22] M. J. Duran and F. Barrero, "Recent Advances in the Design, Modeling, and Control of Multiphase Machines—Part II," in IEEE Transactions on Industrial Electronics, vol. 63, no. 1, pp. 459-468, Jan. 2016, doi: 10.1109/TIE.2015.2448211.

[23] S. Devabhaktuni and R. G., "Performance analysis of three-phase and five-phase inverters with different PWM strategies," 2019 Innovations in Power and Advanced Computing Technologies (i-PACT), 2019, pp. 1-5, doi: 10.1109/i-PACT44901.2019.8960210.

[24] A. Iqbal and E. Levi, “Space vector modulation schemes for a five-phase voltage source inverter,” in Power Electronics and Applications, 2005 European Conference on, DOI 10.1109/EPE.2005.219194, pp. 12pp.–P.12, Sep. 2005

[25] Atif Iqbal & Emil Levi (2006) Space Vector PWM Techniques for Sinusoidal Output Voltage Generation with a Five-Phase Voltage Source Inverter, Electric Power Components, and Systems, 34:2, 119-140, DOI: 10.1080/15325000500244427

[26] Karampuri, Ramsha & Prieto Corvalán, Joel & Barrero, Federico & Jain, Sachin. (2014). A comparison between FOC and DTC methods for five-phase induction motor drives.

[27] K. Rahman et al., "Field-Oriented Control of Five-Phase Induction Motor Fed From Space Vector Modulated Matrix Converter," in IEEE Access, vol. 10, pp. 17996-18007, 2022, doi: 10.1109/ACCESS.2022.3142014.

[28] J. A. Riveros, J. Prieto, F. Barrero, S. Toral, M. Jones, and E. Levi, "Predictive Torque Control for five-phase induction motor drives," IECON 2010 - 36th Annual Conference on IEEE Industrial Electronics Society, Glendale, AZ, USA, 2010, pp. 2467-2472, doi: 10.1109/IECON.2010.5675341.

[29] A. Bhowate, M. V. Aware, and S. Sharma, "Predictive Torque Control Algorithm for a Five-Phase Induction Motor Drive for Reduced Torque Ripple With Switching Frequency Control," in IEEE

Transactions on Power Electronics, vol. 35, no. 7, pp. 7282-7294, July 2020, doi: 10.1109/TPEL.2019.2954991.

[30] Zhang, Qingfei, Jinghong Zhao, Sinian Yan, Yiyong Xiong, Yuanzheng Ma, and Hansi Chen. 2022. "Virtual Voltage Vector-Based Model Predictive Current Control for Five-Phase Induction Motor" *Processes* 10, no. 10: 1925. https://doi.org/10.3390/pr10101925

[31] I. Takahashi and T. Noguchi, "A New Quick-Response and High-Efficiency Control Strategy of an Induction Motor," in IEEE Transactions on Industry Applications, vol. IA-22, no. 5, pp. 820-827, Sept. 1986, doi: 10.1109/TIA.1986.4504799.

[32] Noguchi T, Yamamoto M, Kondo S, Takahashi I 1999 Enlarging switching frequency in direct torque controlled inverter by means of dithering. IEEE Trans. Ind. Appl. 35(6): 1358–1366.

[33] B. S. Khaldi, H. Abu-Rub, A. Iqbal, R. Kennel, M. O. Mahmoudi and D. Boukhetala, "Sensor less direct torque control of five-phase induction motor drives," IECON 2011 - 37th Annual Conference of the IEEE Industrial Electronics Society, Melbourne, VIC, 2011, pp. 3501-3506, doi: 10.1109/IECON.2011.6119875.

[34] L. Parsa and H. A. Toliyat, "Sensorless Direct Torque Control of Five-Phase Interior Permanent-Magnet Motor Drives," in IEEE Transactions on Industry Applications, vol. 43, no. 4, pp. 952-959, July-aug. 2007, doi: 10.1109/TIA.2007.900444.

[35] L. Zheng, J. E. Fletcher, B. W. Williams, and X. He, "A Novel Direct Torque Control Scheme for a Sensorless Five-Phase Induction Motor Drive," in IEEE Transactions on Industrial Electronics, vol. 58, no. 2, pp. 503-513, Feb. 2011, doi: 10.1109/TIE.2010.2047830.

[36] L. Gao, J. E. Fletcher, and L. Zheng, "Low-Speed Control Improvements for a Two-Level Five-Phase Inverter-Fed Induction Machine Using Classic Direct Torque Control," in IEEE Transactions on Industrial Electronics, vol. 58, no. 7, pp. 2744-2754, July 2011, doi: 10.1109/TIE.2010.2070775.

[37] J. A. Riveros, M. J. Durán, F. Barrero and S. Toral, "Direct torque control for five-phase induction motor drives with reduced common-mode voltage," IECON 2012 - 38th Annual Conference on IEEE Industrial Electronics Society, Montreal, QC, Canada, 2012, pp. 3616-3621, doi: 10.1109/IECON.2012.6389317.

[38] S. Payami and R. K. Behera, "An Improved DTC Technique for Low-Speed Operation of a Five-Phase Induction Motor," in IEEE Transactions on Industrial Electronics, vol. 64, no. 5, pp. 3513-3523, May 2017, doi: 10.1109/TIE.2017.2652397.

[39] Tatte, Y., Aware, M. Torque ripple reduction in direct torque controlled five-phase induction motor using modified five-level torque comparator. Sādhanā 43, 6 (2018). https://doi.org/10.1007/s12046-017-0767-9

[40] Yen-Shin Lai and Jian-Ho Chen, "A new approach to direct torque control of induction motor drives for constant inverter switching frequency and torque ripple reduction," in IEEE Transactions on Energy Conversion, vol. 16, no. 3, pp. 220-227, Sept. 2001, doi: 10.1109/60.937200.

[41] Shuai Lu and K. Corzine, "Direct torque control of five-phase induction motor using space vector modulation with harmonics elimination and optimal switching sequence," Twenty-First Annual IEEE Applied Power Electronics Conference and Exposition, 2006. APEC '06., Dallas, TX, USA, 2006, pp. 7 pp.-, doi: 10.1109/APEC.2006.1620539.

[42] U. R. Muduli, B. Chikondra and R. K. Behera, "Space Vector PWM Based DTC Scheme With Reduced Common Mode Voltage for Five-Phase Induction Motor Drive," in IEEE Transactions on Power Electronics, vol. 37, no. 1, pp. 114-124, Jan. 2022, doi: 10.1109/TPEL.2021.3092259.

[43] N. R. N. Idris and A. H. M. Yatim, "Direct torque control of induction machines with constant switching frequency and reduced torque ripple," in IEEE Transactions on Industrial Electronics, vol. 51, no. 4, pp. 758-767, Aug. 2004, doi: 10.1109/TIE.2004.831718.

[44] G. H. B. Foo and X. Zhang, "Constant Switching Frequency Based Direct Torque Control of Interior Permanent Magnet Synchronous Motors With Reduced Ripples and Fast Torque Dynamics," in IEEE Transactions on Power Electronics, vol. 31, no. 9, pp. 6485-6493, Sept. 2016, doi: 10.1109/TPEL.2015.2503292.

[45] Venkata Subba Reddy C, Swati Devabhaktuni. "Low-speed Performance improvement of Constant Switching Frequency DTC of Five-Phase Induction Motor", 2021 National Power Electronics Conference (NPEC), 2021

[46] L. M. Tolbert, Fang Zheng Peng, and T. G. Habetler, "Multilevel converters for large electric drives," in IEEE Transactions on Industry Applications, vol. 35, no. 1, pp. 36-44, Jan.-Feb. 1999, doi: 10.1109/28.740843.

[47] H. Ismail et al., "Direct Torque Control of induction machine using 3-level neutral point clamped inverter," 2015 IEEE Student Conference on Research and Development (SCOReD), Kuala Lumpur, Malaysia, 2015, pp. 571-576, doi: 10.1109/SCORED.2015.7449401.

[48] F. Khoucha, S. M. Lagoun, K. Marouani, A. Kheloui and M. E. H. Benbouzid, "Hybrid Cascaded H-Bridge Multilevel-Inverter Induction-Motor-Drive Direct Torque Control for Automotive Applications," in IEEE Transactions on Industrial Electronics, vol. 57, no. 3, pp. 892-899, March 2010, doi: 10.1109/TIE.2009.2037105.

[49] M. F. Escalante, J. . -C. Vannier and A. Arzande, "Flying capacitor multilevel inverters and DTC motor drive applications," in IEEE Transactions on Industrial Electronics, vol. 49, no. 4, pp. 809-815, Aug. 2002, doi: 10.1109/TIE.2002.801231.

[50] Y. N. Tatte and M. V. Aware, "Torque Ripple and Harmonic Current Reduction in a Three-Level Inverter-Fed Direct-Torque-Controlled Five-Phase Induction Motor," in IEEE Transactions on Industrial Electronics, vol. 64, no. 7, pp. 5265-5275, July 2017, doi: 10.1109/TIE.2017.2677346.

[51] S. Payami, R. K. Behera and A. Iqbal, "DTC of Three-Level NPC Inverter Fed Five-Phase Induction Motor Drive With Novel Neutral Point Voltage Balancing Scheme," in IEEE Transactions on Power Electronics, vol. 33, no. 2, pp. 1487-1500, Feb. 2018, doi: 10.1109/TPEL.2017.2675621.

[52] R. E. Kodumur Meesala and V. K. Thippiripati, "An Improved Direct Torque Control of Three-Level Dual Inverter Fed Open-Ended Winding Induction Motor Drive Based on Modified Look-Up Table," in IEEE Transactions on Power Electronics, vol. 35, no. 4, pp. 3906-3917, April 2020, doi: 10.1109/TPEL.2019.2937684.

[53] R. Karampuri, S. Jain and V. T. Somasekhar, "Common-Mode Current Elimination PWM Strategy Along With Current Ripple Reduction for Open-Winding Five-Phase Induction Motor Drive," in

IEEE Transactions on Power Electronics, vol. 34, no. 7, pp. 6659-6668, July 2019, doi: 10.1109/TPEL.2018.2873692.

[54] R. Karampuri, S. Jain and V. T. Somasekhar, "Sample-Averaged Zero-Sequence Current Elimination PWM Technique for Five-Phase Induction Motor With Opened Stator Windings," in IEEE Journal of Emerging and Selected Topics in Power Electronics, vol. 6, no. 2, pp. 864-873, June 2018, doi: 10.1109/JESTPE.2017.2759965.

[55] Reddy, C.V.S., Devabhaktuni, S. (2022). Low-Speed Performance Improvement of Dual VSI Fed Direct Torque Controlled Five Phase Open-End Winding Induction Motor. In: Kumar, S., Singh, B., Singh, A.K. (eds) Recent Advances in Power Electronics and Drives. Lecture Notes in Electrical Engineering, vol 852. Springer, Singapore. https://doi.org/10.1007/978-981-16-9239-0_20.

[56] P. C. Mavila and P. P. Rajeevan, "A New Direct Torque Control Scheme for Five Phase Open-end Winding Induction Motor Drives with Reduced DC Voltage Requirement," 2020 IEEE International Conference on Power Electronics, Smart Grid and Renewable Energy (PESGRE2020), Cochin, India, 2020, pp. 1-6, doi: 10.1109/PESGRE45664.2020.9070665.

[57] P. C. Mavila and P. P. Rajeevan, "A Five Level DTC Scheme for Dual Inverter-Fed Five Phase Open-End Winding Induction Motor Drives with Single DC Source," 2019 IEEE Industry Applications Society Annual Meeting, Baltimore, MD, USA, 2019, pp. 1-6, doi: 10.1109/IAS.2019.8912445

[58] P. C. Mavila and P. P. Rajeevan, "A Five-Level Torque Controller Based DTC Scheme for Open-End Winding Five-Phase IM Drive With Single DC Source and Auxiliary Plane Harmonic Elimination," in IEEE Transactions on Industry Applications, vol. 58, no. 2, pp. 2063-2074, March-April 2022, doi: 10.1109/TIA.2022.3140361.

[59] N. R. N. Idris and A. H. M. Yatim, "Reduced torque ripple and constant torque switching frequency strategy for direct torque control of induction machine," APEC 2000. Fifteenth Annual IEEE Applied Power Electronics Conference and Exposition (Cat. No.00CH37058), New Orleans, LA, USA, 2000, pp. 154-161 vol.1, doi: 10.1109/APEC.2000.826099.

[60] Wardi, M.L., Abdelkrim, R., Abdelkrim, M.N. (2022). Fractional Order CRONE and PID Controllers Design for Nonlinear Systems Based on Multimodel Approach. In: Naifar, O., Ben Makhlouf, A. (eds) Fractional Order Systems—Control Theory and Applications. Studies in Systems, Decision and Control, vol 364. Springer, Cham. https://doi.org/10.1007/978-3-030-71446-8_7

[61] Chandra Sekhar, O., Lakhimsetty, S., & Bhat, A. H. (2020). A comparative experimental analysis of fractional order PI controller based direct torque control scheme for induction motor drive. International Transactions on Electrical Energy Systems. doi:10.1002/2050-7038.12705

[62] Ali, Daniyal & Khurram, Adil & Rehman, Habib-Ur & Mukhopadhyay, Shayok. (2018). Comparative analysis of integer-order and fractional-order proportional integral speed controllers for induction motor drive systems. Journal of Power Electronics. 18. 723-735. 10.6113/JPE.2018.18.3.723.

[63] Jun-Yi Cao, Jin Liang and Bing-Gang Cao, "Optimization of fractional order PID controllers based on genetic algorithms," 2005 International Conference on Machine Learning and Cybernetics, Guangzhou, China, 2005, pp. 5686-5689 Vol. 9, doi: 10.1109/ICMLC.2005.1527950.

[64] Ranjan, Vineeta et al. “Design of Integer and Fractional order PID Controller using Dominant Pole Placement Method.” (2013).

[65] Abdellatif Kasbi, & Abderrafii Rahali. (2019). Design a Fractional Order Controller for Power Control of a Doubly Fed Induction Generator Based Wind Generation System. International Journal of Electrical, Electronic and Communication Sciences, 12.0(8). https://doi.org/10.5281/zenodo.3455647

[66] Chen, H.; Xie, W.; Chen, X.; Han, J.; Aït-Ahmed, N.; Zhou, Z.; Tang, T.; Benbouzid, M. Fractional-Order PI Control of DFIG-Based Tidal Stream Turbine. J. Mar. Sci. Eng. 2020, 8, 309. https://doi.org/10.3390/jmse8050309

[67] Hafezi, H.; Faranda, R. A New Approach for Power Losses Evaluation of IGBT/Diode Module. Electronics 2021, 10, 280. https://doi.org/10.3390/electronics10030280

[68] N. R. N. Idris, A. H. M. Yatim, N. D. Muhamad and T. C. Ling, "Constant frequency torque and flux controllers for direct torque control of induction machines," IEEE 34th Annual Conference on Power Electronics Specialist, 2003. PESC '03., Acapulco, Mexico, 2003, pp. 1095-1100 vol.3, doi: 10.1109/PESC.2003.1216602.

[69] C. L. Toh, N. R. N. Idris and A. H. M. Yatim, "New torque and flux controllers for direct torque control of induction machines," The Fifth International Conference on Power Electronics and Drive Systems, 2003. PEDS 2003., Singapore, 2003, pp. 216-221 Vol.1, doi: 10.1109/PEDS.2003.1282757.

[70] V. S. Reddy and S. Devabhaktuni, "Enhanced Low-Speed characteristics with Constant Switching Torque Controller-based DTC Technique of Five-Phase Induction Motor Drive with FOPI Control," in IEEE Transactions on Industrial Electronics, doi: 10.1109/TIE.2022.3227275.

[71] X. Wu, W. Huang, X. Lin, W. Jiang, Y. Zhao, and S. Zhu, "Direct Torque Control for Induction Motors Based on Minimum Voltage Vector Error," in IEEE Transactions on Industrial Electronics, vol. 68, no. 5, pp. 3794-3804, May 2021, doi: 10.1109/TIE.2020.2987283.

Appendix

Experimental test setup details

The block diagram representation of a 2-level VSI-fed 5-phase induction motor drive is shown in Figure A.1. Similarly, the experimental prototype for a 2-level VSI-fed 5-phase induction motor drive is shown in Figure A.2. The 5-phase induction motor used for this experimentation is a 1 HP, 100V, 3.4A, 5-phase squirrel cage induction motor coupled with 1 HP separately excited DC generator and is loaded resistive lamp loads. The DC supply for the inverter is obtained from the inbuilt rectifier along with DC link capacitors. The experimental block diagram for a dual inverter-fed 5-phase open-end winding induction motor is shown in Figure A.3. and Figure A.4 shows the experimental hardware prototype for a dual inverter-fed 5-phase open-end winding induction motor. The inverter modules have an inbuilt driver circuit to accept the 5V gate pulses to activate switches. The currents in four phases are sensed with Hall Effect current sensors which are manufactured by LEM. Similarly, the DC link voltage is measured using Hall Effect voltage sensors which are manufactured by LEM. The speed of the induction motor is measured by an incremental optical rotary encoder which is mounted on the shaft of the motor. The speed encoder produces 1024 pulses per rotation of the shaft.

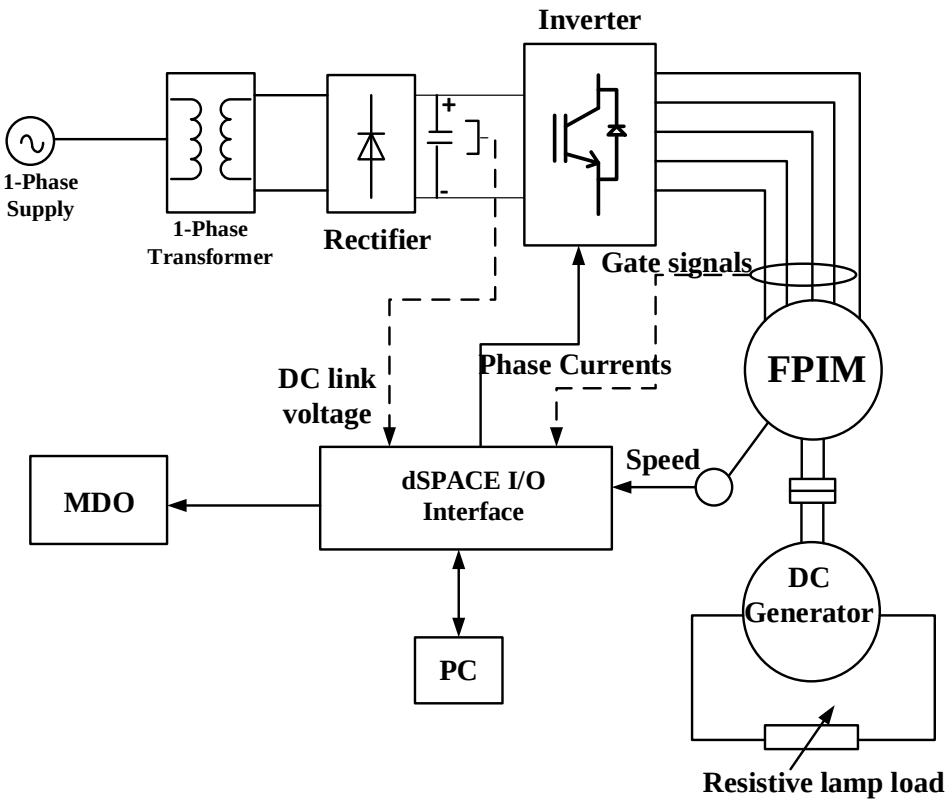

Figure A.1 Block diagram representation of experimental setup of 2-level VSI fed FPIM

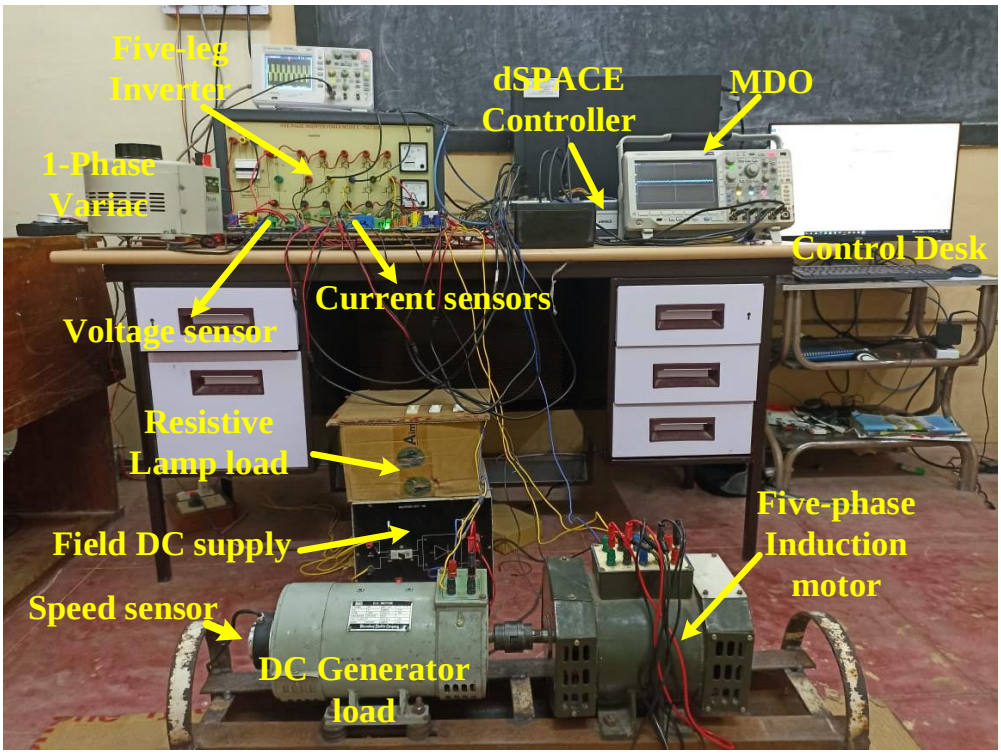

Figure A.2 Experimental setup of VSI-fed FPIM drive to conduct different DTC schemes

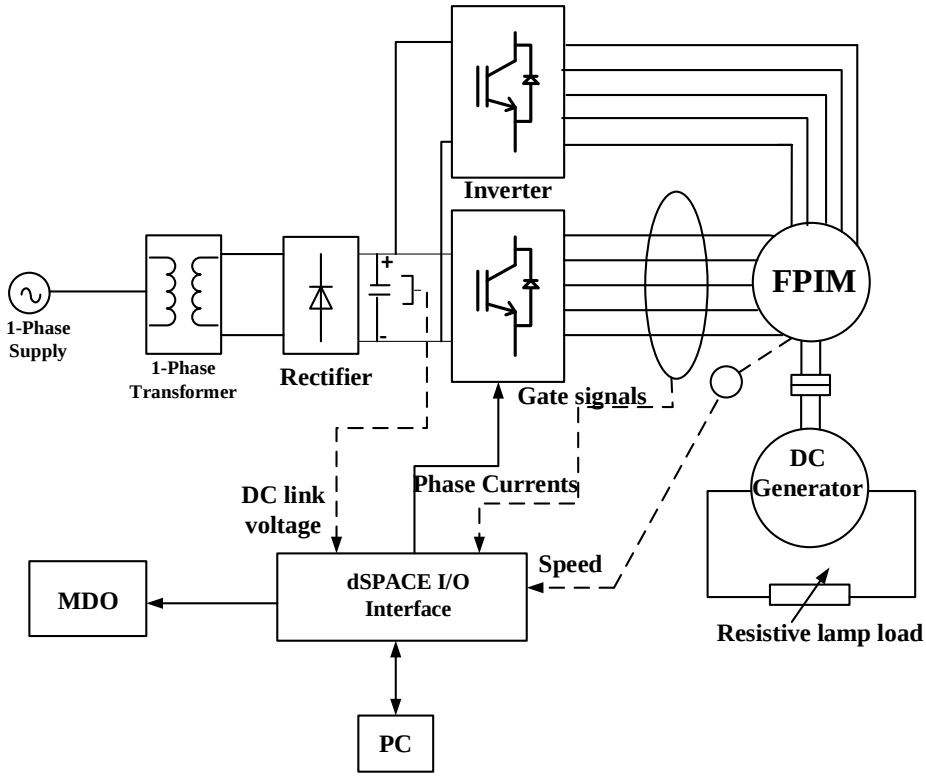

Figure A.3 Block diagram representation of experimental setup of dual inverter fed FPOEWIM

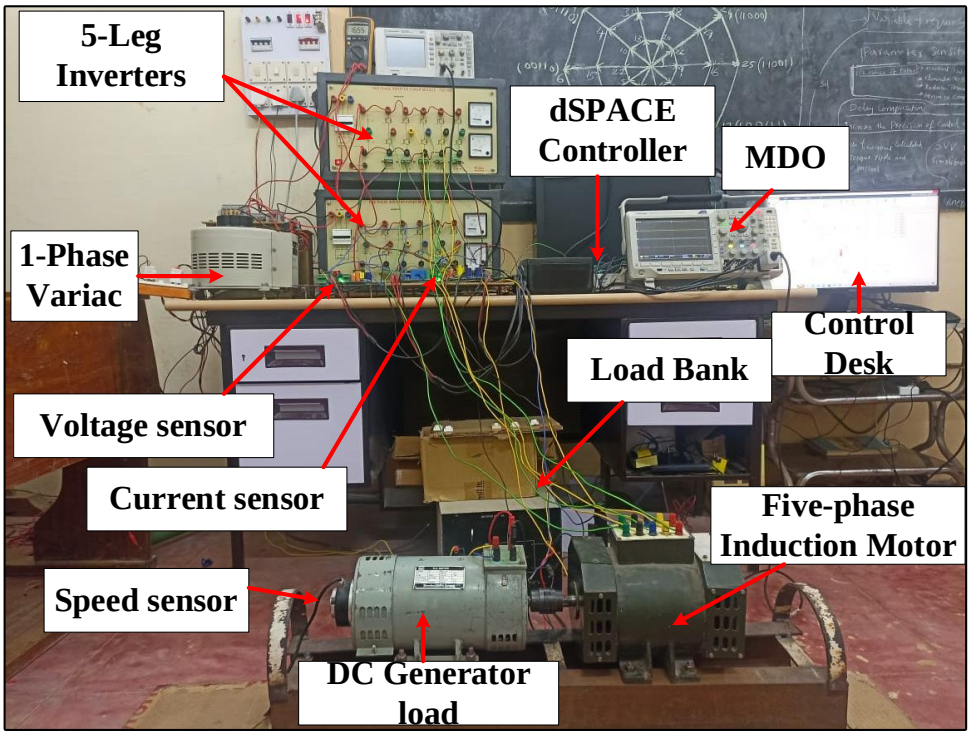

Figure A.4 Experimental setup of dual inverter FPOEWIM drive to conduct different DTC schemes

The dSPACE 1102/1202 controller is used for the implementation of all the DTC schemes on the VSI-fed 5-phase induction motor. The dSPACE controller is equipped with inbuilt ADC ports, and DAC ports which allow a maximum of ±10V signals. The dSPACE contains digital I/O pins which give 5V triggering pulses. The dSPACE controller also contains an incremental encoder port which directly communicates the speed encoder. The dSPACE controller can be interfaced with MATLAB/Simulink software and different control parameters are monitored and controlled online from the dSPACE Control Desk software. The experimental test setup parameters are tabulated in Table A.1, Table A.2, and Table A.3.

Table A.1: 5-phase induction motor parameters

Parameter	value	Parameter	Value	Parameter	Value
Power Rating	1 HP	Stator resistance (Rs)	1.05 Ω	Rotor resistance (Rr)	1.42 Ω
Stator inductance (Ls))	90.73mH	Mutual inductance (Lm)	84.73mH	Rotor inductance (Lr)	90.73mH
No. of Poles (P)	4	Inertia constant (J)	0.148Kg-m^2	Rated Speed	1400 rpm

Table A.2 5-leg voltage source inverter details

Parameter	**value**	**Parameter**	**Value**	**Parameter**	**Value**
Voltage Rating	1200 V	Current rating	75 A	DC link capacitor	4700 µF

Table A.3: Voltage sensor and current sensor details

Parameter	**value**	**Parameter**	**Value**	**Parameter**	**Value**
Supply voltage	±15 V	Maximum sensing voltage	1000 V	Maximum sensing current	25 A